DESIGN AND IMPLEMENTATION OF

ULTRA-HIGH RESOLUTION, LARGE BANDWIDTH, AND

COMPACT DIFFUSE LIGHT SPECTROMETERS

A Thesis
Presented to
The Academic Faculty

by

Majid Badieirostami

In Partial Fulfillment
of the Requirements for the Degree of
Doctor of Philosophy in Electrical and Computer Engineering

Georgia Institute of Technology
December 2008

DESIGN AND IMPLEMENTATION OF

ULTRA-HIGH RESOLUTION, LARGE BANDWIDTH, AND

COMPACT DIFFUSE LIGHT SPECTROMETERS

Approved by:

Prof. Ali Adibi, Advisor
School of Electrical and Computer Engineering
Georgia Institute of Technology

Prof. Thomas K. Gaylord
School of Electrical and Computer Engineering
Georgia Institute of Technology

Prof. W. Russell Callen, Jr.
School of Electrical and Computer Engineering
Georgia Institute of Technology

Prof. Pamela T. Bhatti
School of Electrical and Computer Engineering
Georgia Institute of Technology

Prof. Hao-Min Zhou
School of Mathematics
Georgia Institute of Technology

Date Approved: November 6, 2008

In the name of God, Most Gracious, Most Merciful

To my mother, my wife,

and

in the loving memory of my father

ACKNOWLEDGEMENTS

At the onset, I wish to thank Prof. Ali Adibi not only for being my advisor but also for being my best friend during my Ph.D. He trained me to be an independent researcher and imbibed me with the sense of confidence to search for solutions with hope and patience. I am thankful to him for all of his encouragement, advice, and support. He is a smart researcher, skillful teacher, honest consultant and an overall supportive person. One can rarely satisfy him as he usually expects more and better. I am happy to have known and worked with him; it was one of the golden opportunities of my life. I would like to also sincerely thank his wife, Mrs. Samineh Salimi, for all her hospitality and kindness over the years.

I am also grateful for collaboration with several elite professors during my Ph.D. research. I appreciate helpful discussions I have had with Prof. David J. Brady from Duke University, and Prof. Hao-Min Zhou, Prof. Thomas K. Gaylord, and Prof. Joseph W. Perry all from Georgia Tech. I have also benefited in my research from my colleagues Dr. Omid Momtahan, Dr. Babak Momeni, Mr. Ali Asghar Eftekhar, and Dr. Siva Yegnanarayanan, to all of whom I am thankful.

Moreover, I would like to thank our other group members Charles M. Reinke, Dr. Arash Karbaschi, Dr. Aliakbar Jafarpour, Cheryl M. Reid, Dr. Chaoray Hsieh, Mohammad Soltani, Fengtao Wang, Ehsan Shah Hosseini, Murtaza Askari, Ye Lou, Pouyan Mohajerani, Ali Hashmi, Charles H. Camp, Amir Hossein Atabaki, Qing Li, Maysamreza Chamanzar, Payam Alipour, and Ali Behrooz for their friendship and support. I will never forget the fun times we had together. I am also thankful to my

colleague and roommate Saeed Mohammadi who is a polite, kind, and honest person. In addition, I would like to acknowledge some of my other friends at Georgia Tech with whom I spent valuable time: Dr. Reza Sarvari, Dr. Baabak Ashuri, Hossein Miri, Ehsan Najafabadi, Ali Lari, Pedram Javanmard, Mohsen Sardari, and Alireza Khoshgoftar.

I believe that I have had outstanding teachers who always motivated me to be better. Among them, two have deeply influenced my personality: Mr. Seyyed Jafar Tahavvori, my teacher in middle school, and Mr. Naser Kazemi, my teacher in Alavi High School. I will always be indebted to them. I am also thankful to all of my friends and teachers at Alavi High School with whom I share many good memories. I never been happier than at Alavi in my life, and I am really fond of Alavi's staff and environment.

Moreover, I would like to thank my Quantum Optics teacher, Prof. Brian Kennedy of the School of Physics at Georgia Tech whose teaching style impressed me the most. I have taken more courses with him than with any other professor. I am also thankful to Prof. Monson Hayes and Prof. Andrew Peterson of the School of Electrical and Computer Engineering at Georgia Tech who are both skillful and professional instructors, and my undergraduate teacher Prof. Jawad Salehi of the School of Electrical Engineering at Sharif University of Technology who gave me the vision and inspiration for graduate study.

Last but not least, I am grateful to my family, my parents, my sister, and my brother who always supported me from childhood. I express my ultimate gratitude to my mother for all her love, passion, kindness, sacrifice, encouragement, and support. She is forever my wise friend and trusted advisor. There are no words to express my gratitude for my mother.

Recently, I married my dearest love, Razieh. She is a wise, patient, and passionate wife. She is my kindest friend and beautiful helper. These days, my only grief is the lack of her presence. Yet, talking to her gives me energy and motivation to move forward. I am fortunate for having such a wonderful wife.

Finally, I thank God, the Almighty, who gave me strength, wisdom, and imparted such great friends, family, and teachers to me.

TABLE OF CONTENTS

LIST OF TABLES

LIST OF FIGURES

LIST OF ABBREVIATIONS

1D	One-Dimensional
2D	Two-Dimensional
3D	Three-Dimensional
CBVH	Cylindrical Beam Volume Hologram
CCD	Charge-Coupled Device
ETF	Envelope Transfer Function
FDTD	Finite Difference Time Domain
FPE	Fabry-Perot Etalon
FSR	Free Spectral Range
FWHM	Full Width at Half Maximum
PC	Photonic Crystal
PDE	Partial Differential Equation
SBVH	Spherical Beam Volume Hologram
SEM	Scanning Electron Microscopy
SNR	Signal to Noise Ratio
TE	Transverse Electric
TM	Transverse Magnetic
WCE	Wiener Chaos Expansion

SUMMARY

To realize spectrometers with state-of-the-art performance measures, we need to combine novel synthetic material properties and new device concepts using efficient design and optimization tools. Considering the material engineering, device innovation, and modeling and simulation tool development as the three primary areas of research in the invention of modern spectrometers, I put myself at the intersection of these three areas. My Ph.D. research has been focused on the development of such infrastructures for next generation spectrometers.

My research on the new concepts for spectrometer has been focused on the development of true multi-dimensional spectrometers, which use a multi-dimensional [two-dimensional (2D) or 3D] mapping of the spectral information into space. While the conventional spectrometers use a grating to form a one-dimensional (1D) spatial-spectral mapping, I showed that by combining a simple dispersive element (a volume hologram) formed in very inexpensive polymers with a basic Fabry-Perot interferometer, we can form a spectrometer with ultra-high resolution over a large spectral bandwidth, which surpasses all conventional spectrometers. This unique performance is obtained by the 2D spatial-spectral mapping enabled by combining two simple optical functionalities. I strongly believe that the extension of this mapping into three dimensions by using synthetic nanophotonic structures with engineered dispersion (optimized using the recently demonstrated modeling tool) can further improve the performance and reduce the overall spectrometer size into the micron regime.

The need for efficient modeling and simulation tools comes from the sophisticated nature of the new 3D nanophotonic structures, which makes their simple analysis using well-known simple formulas for the propagation of the electromagnetic fields in bulk materials impossible. On the other hand, direct numerical simulation of these structures using the well-known numerical simulation tools such as finite difference time-domain or the finite element techniques is not possible due to the excessive requirement of memory and simulation time. Added to the complexity of the problem is the diffuse (or spatially incoherent) nature of the optical beams in the state-of-the-art spectroscopy applications. In my Ph.D. research, I developed new approximate modeling tools for both the modeling of incoherent sources in nanophotonics, and for the propagation of such optical beams inside the 3D nanophotonic structures of interest with several orders of magnitude improvement in the simulation speed for practical size devices without sacrificing accuracy. I believe the tools developed in my research enable us to look into new structures and functionalities that we were not able to analyze simply before.

To enable new dispersive properties using a single nanophotonic structure, I have focused in my Ph.D. research into polymer-based 3D photonic crystals, which can be engineered using their geometrical features to demonstrate unique dispersive properties in three dimensions that cannot be matched by any bulk material even with orders of magnitude larger sizes. I have demonstrated the possibilities of using a very compact structure for wavelength demultiplexing and also for spectroscopy without adding any other device. The range of applications that can be enabled by having a material system with a wide range of 3D dispersive properties is very wide covering spectroscopy and

sensing, dispersion management, diffraction compensation, pulse shaping, and many others. I am very interested in using this material platform and extend my current research into 3D heterostructures in which each portion of the structure is engineered to optimize a subset of optical functionalities. The simplest version of such heterostructures is the integration of interferometry and spectroscopy in a single structure. The most general view of such engineered nanostructures is to consider them as a 3D version of the gratings for the spatial-spectral mapping of the information in an optical beam.

CHAPTER 1

INTRODUCTION

Recent increasing demand for high performance handheld sensors for biological and environmental sensing has inspired a lot of research in this area [1-5]. Many optical techniques for such sensing applications rely on the measurement of the spectrum of a light beam after interaction with analyte of interest [6-10]. Thus, the development of compact and low-cost spectrometers with high resolution and large operation bandwidth is highly desired. The use of conventional spectrometers, especially for diffuse source spectroscopy [11-15] (which is the case of interest in many biological and environmental sensing applications) has a few major drawbacks. First, it requires a collimation subsystem (typically a slit and a lens). This adds to the bulkiness and also requires good alignment of different elements in the system [16]. Secondly, to improve the resolution and at the same time to increase the bandwidth of operation, one must enlarge the size of the detector array along the dispersion axis, which makes the overall system larger and more expensive [17]. This is caused by the one-dimensional (1D) nature of the spatial-spectral coding in these spectrometers which are usually based on diffractive gratings as seen in Figure 1.1. This 1D spatial-spectral response is referred to as the trade-off between the resolution and the operation bandwidth throughout this research.

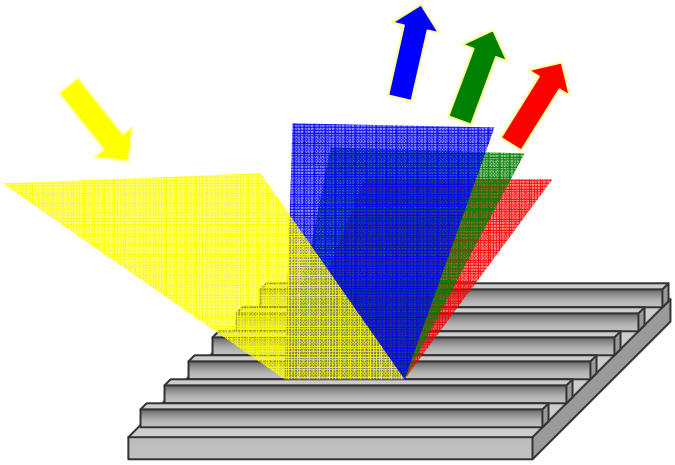

Figure 1.1. Schematic of a spectrometer composed of a diffractive grating which results in a 1D spatial-spectral mapping.

Here our main goal in this thesis is to design and implement a high resolution large bandwidth compact diffuse light spectrometer which is also able to encode the spectral information in a two-dimensional (2D) pattern on a detector array or a charge-coupled device (CCD) chip. To achieve this goal, this thesis is divided into three parts as follows:

1.1. Design and Implementation of a Diffuse Light Spectrometer

There are three major performances that have to be achieved simultaneously to realize such a diffuse spectrometer: 1) ability to disperse a diffuse beam, 2) improvement of the resolution without sacrificing the bandwidth, and 3) ability of 2D spatial-spectral mapping. At first, we study the spectral response of conventional interferometric and diffractive elements to investigate their functionalities under diffuse light illumination. Then, we start from the successful implementation of diffuse light spectrometers based on volume holograms [18, 19] and try to improve their resolutions by incorporating an interferometric device like a Fabry-Perot etalon (FPE) [20, 21]. We show that in order to realize both high resolution and large spectral bandwidth independently, we can make

benefit of a special type of volume holograms known as cylindrical beam volume holograms (CBVHs). We also show that such a tandem spectrometer composed of a FPE and a CBVH collectively results into a 2D spatial-spectral pattern on the CCD.

To further shrink the size of this spectrometer and for more efficient spatial encoding of the spectral channels, we propose to use a new material platform based on three-dimensional (3D) photonic crystal (PC) structures [22-24]. In this new platform, we can merge the functionalities of both interferometric and diffractive elements together and replace the tandem spectrometer with an extremely compact properly designed 3D PC microspectrometer [25].

1.2. Efficient Modeling of a Spatially Incoherent Source

Prior to analysis and design of 3D PC microspectrometers, we have to develop a simulation tool to model a spatially incoherent (i.e., diffuse) source. Initially, we propose a Monte-Carlo model which results in almost one order of magnitude less computation time compared to the conventional brute-force model. However, its simulation results are not as accurate as those of the brute-force model. For a more accurate simulation, we further propose a new analytical model based on the Wiener chaos expansion (WCE) method. We numerically implement this model using the finite difference time domain (FDTD) technique and once again compare it to the brute-force model. It will be shown that by using WCE model, the simulation time is reduced considerably while the results are in excellent agreement with those obtained by the brute-force model.

1.3. Design and Implementation of a 3D PC Microspectrometer

PCs are synthetic periodic dielectric structures [26-30] with controllable dispersion which can be engineered and utilized for numerous dispersive applications [31-35]. Among

these applications, the possibility of wavelength demultiplexing and spectroscopy using the superprism effect is of particular interest [36-45]. Figures 1.2(a) and (b) show a 2D and a 3D PC spectrometer, respectively. Unlike simple diffractive gratings, they can result in multidimensional spatial-spectral mapping. The 2D PC structure is able to separate the wavelength channels in a 2D plane while the 3D PC structure can go further and focus them in different depths of a volume and thus results in 3D spatial encoding of the wavelength channels.

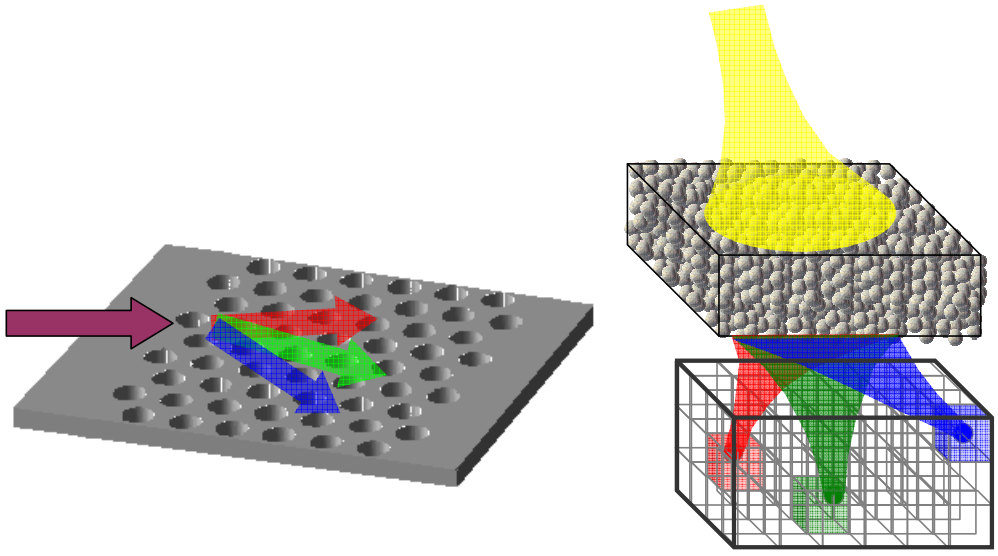

(a) (b)

Figure 1.2. (a) Schematic of a 2D PC spectrometer which is able to map the spectral information into a 2D spatial pattern. (b) Schematic of a 3D PC spectrometer which further enables a 3D spatial-spectral mapping.

2D PC planar structures because of their compatibility with well-developed microelectronic fabrication techniques and possibility of integration in a planar platform have been extensively investigated for many dispersive applications including spectroscopy. However, free-space structures using 3D PCs are highly preferred to avoid the issue of coupling light into and out of a planar platform. In addition, recent advances in the fabrication of 3D PC structures, including self assembly [46], direct laser writing by multi-photon lithography [47-49], and multi-beam interference lithography [50-52]

have made possible the realization of such structures for practical applications. Applications including beam shaping, dispersion control, and spectroscopy are among a variety of possibilities in which unique dispersive properties of 3D PCs can be used [53-60]. Figure 1.3 shows the scanning electron microscope (SEM) image of a tetragonal woodpile 3D PC structure fabricated using a direct laser writing technique which is used in the last part of this research for the implementation of low-cost ultra-compact spectrometers.

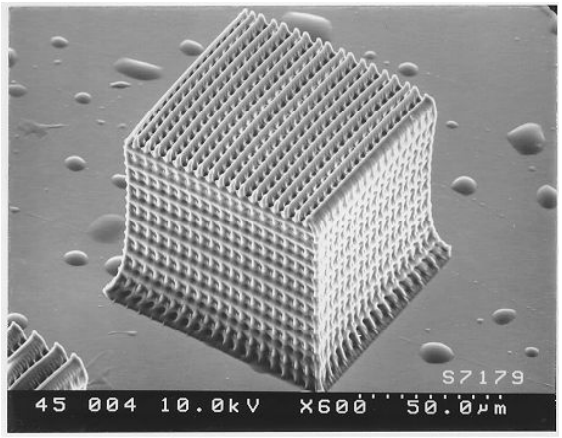

Figure 1.3. SEM image of a tetragonal woodpile 3D PC structure fabricated using a direct laser writing technique.

It has been shown recently that the propagation of optical beams in 2D PCs can be accurately and efficiently analyzed using an effective diffractive index model. Following the same procedure, we develop a diffractive index model for fast and efficient analysis of the beam propagation effects inside 3D PC structures. Having this model developed, we move on to the engineering of functional dispersive devices. We later report on a successful implementation of a 4-chanel and a 6-channel 3D PC demultiplexer which also can be renamed as a proof of principle a microspectrometer. Moreover, we discuss all the design requirements and practical issues which are present in this research.

We believe the low-cost technology and the cheap polymer materials used for the fabrication of this kind of dispersive devices in addition to their design freedoms can revolutionize the spectrometer industry by delivering cheap hand-held high resolution large spectral bandwidth diffuse light spectrometers.

This thesis is organized as following: The first two chapters after introduction deal with the first part of this research regarding the design and implementation of a tandem FPE CBVH spectrometer. In Chapter 2 we investigate the functionality of conventional spectroscopic elements under diffuse light and propose an innovative design to achieve both high resolution and large bandwidth. Chapter 3 reports on the experimental demonstration of a tandem spectrometer. In the next two chapters, we develop a simulation model for a diffuse source. The Monte-Carlo model and the WCE model are described in Chapters 4 and 5, respectively. The subsequent two chapters are focused on the applicability of 3D PCs for functional dispersive devices. The diffractive index model to expedite analysis of beam propagation effects is developed in Chapter 6 and its application for implementation of a wavelength demultiplexer is specified in Chapter 7. Finally, concluding remarks and future directions are given in Chapter 8.

CHAPTER 2

DIFFUSE LIGHT SPECTROMETERS

There are many proposals for the development and improvement of clinical instruments for identification of specific chemicals in human body. Besides, recently, there are huge investments for the development of environmental detection systems for immediate response to hazardous materials for safety and security purposes. Looking into any kind of these instruments, one can certainly verify that its most significant block is a sensor for bulk identification or even an exact percentage measurement of some specific molecules in a target medium.

Among many sensing mechanisms, optical spectroscopy is a powerful diagnostic tool because of its high specificity and potential for in vivo measurements [6-8]. Moreover, its non-invasive nature makes it very suitable for easy and fast medical examinations. On contrary to all these advantages, its very small cross-section and diffuse properties in a highly scattering medium like blood or tissue make the optical signal very weak and challenging to detect. There are numerous reports on the development of coherent light spectrometers which mostly use a spatial filter (i.e., a slit and a collimator) to select only a limited narrow divergence angle of the input beam [61]. However, there are only a few reports on the development of diffuse light spectrometers without any input slit [16].

In this chapter we plan to study the spatial-spectral response of the conventional spectrometers under diffuse light illumination and to show how effectively we can improve their performance by a new design mechanism. Two significant specifications of

a high-quality spectrometer are spectral bandwidth and resolution. Throughout this chapter, our strategy is to come up with a new design to get the best of both, a high resolution and at the same time a large bandwidth.

The conventional spectroscopic devices are categorized in two major types: the interferometers and the diffraction gratings. We first analyze different examples of each category for its spatial-spectral response and investigate its pros and cons regarding bandwidth and resolution. The bandwidth of the spectrum is defined as the maximum range of wavelengths over which the spectrometer can determine the spectrum of the input. The resolution of the spectrometer is usually defined as the smallest difference in the wavelengths of two monochromatic input beams while the corresponding outputs can be resolved on the output detector. The interferometers are well-known of high resolution while the gratings are mostly distinguished for their large bandwidth. In each category we end up with the best candidate capable of diffuse light spectroscopy, the Fabry-Perot etalon (FPE) and the cylindrical beam volume hologram (CBVH), respectively. Later, we combine these two interferometric and diffractive elements and verify its better performance, i.e., the larger bandwidth and the higher resolution, compared to its individual building blocks. We show that in this tandem configuration the collimation subsystem, i.e., the slit and the collimation lens, has been removed to make the final spectrometer very compact and less alignment sensitive than the conventional ones. Furthermore, the less number of elements accordingly reduces the cost too. It will be also shown that the tandem FPE CBVH spectrometer has a two-dimensional (2D) spatial-spectral response rather than the conventional one-dimensional (1D) response and it results in a more efficient and compact coding of spectral information on the CCD.

2.1. Interferometric Spectrometers

Interferometric spectrometers work based on the fact that the interference pattern of any spectral channel as a result of propagation through two or more paths is a function of its wavelength. Therefore, by calibration and analysis of fringe (i.e., interference) patterns we can determine their spectral information [21]. In this section, we look into two major interferometric spectrometers, thin films and FPEs.

2.1.1. Thin Films

The very initial example of an interferometer is a stand alone thin film composed of a dielectric material like silica (SiO_2) or titania (TiO_2). To analyze the operation of a thin film interferometer, we choose a titania film with $n_f = 2.5$ and $d_f = 20$ μm. For the titania film the reflectivity is [62]

$$R = \Gamma^2 = \left(\frac{n_f - 1}{n_f + 1}\right)^2 = \left(\frac{3}{7}\right)^2 \tag{2.1}$$

where for the silica with $n_f = 1.5$, the reflectivity is $R = \left(\frac{1}{5}\right)^2$. Higher reflectivity result in higher extinction ratio,

$$\frac{T_{max}}{T_{min}} = \frac{1}{\left(\frac{1-R}{1+R}\right)^2}\ , \tag{2.2}$$

where T_{max} and T_{min} stand for the maximum and the minimum transmission, respectively. Consequently, higher extinction ratio results in higher signal to noise ratio (SNR) in practical demonstrations. Moreover, if we calculate the full width at half maximum (FWHM) of the resonance peaks (i.e., $\Delta\lambda_{1/2}$) as a measure of resolution for both the titania and the silica films [62],

$$\Delta\lambda_{1/2} = \frac{{\lambda_0}^2}{2n_f d_f}\left(\frac{1-R}{\pi\sqrt{R}}\right) \tag{2.3}$$

we find that the titania film has almost four times better resolution than the silica film. This justifies the better performance of higher refractive index materials for spectroscopic instruments.

Figure 2.1 shows the schematic of a thin film spectrometer in which a CCD is placed at the focal plane of a lens. Hence, the spectral response of the thin film is Fourier transformed to its spatial pattern on the CCD. The input beam is a TE polarized uniform diffuse beam which has all the possible free space wavevectors ($-90° \le \theta \le +90°$). Figures 2.2(a)-(d) show the spatial responses of the titania film on the CCD for four different spectral channels, 550-553 nm, respectively. As seen in these figures, the spectral information of each wavelength is mapped into a circularly symmetric spatial pattern on the CCD. Comparing Figure 2.2(a) with Figures 2.2(b) and 2.2(c) clearly shows that changing the input wavelength results in a small shift of the circular patterns along the radial direction. Therefore, the whole spectral information of the input diffuse beam can be retrieved from the radial dimension of the CCD and its azimuthal dimension carries no more spectral information and it is left useless. In other words, the spectral information recorded along the quarter-circles on the CCD is redundant. This is in fact a 1D spatial-spectral mapping in spite of its 2D appearance and it is not desired because of the wasteful use of the 2D detector array (i.e., CCD).

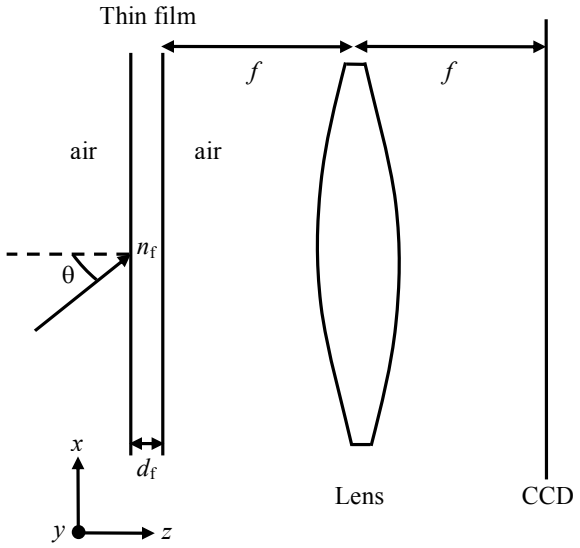

Figure 2.1. Schematic of a thin film spectrometer. The thin film is composed of a titania layer with $n_f = 2.5$ and $d_f = 20$ μm. The spectral information of the input diffuse beam is mapped into its spatial pattern at the Fourier plane of the lens on the CCD.

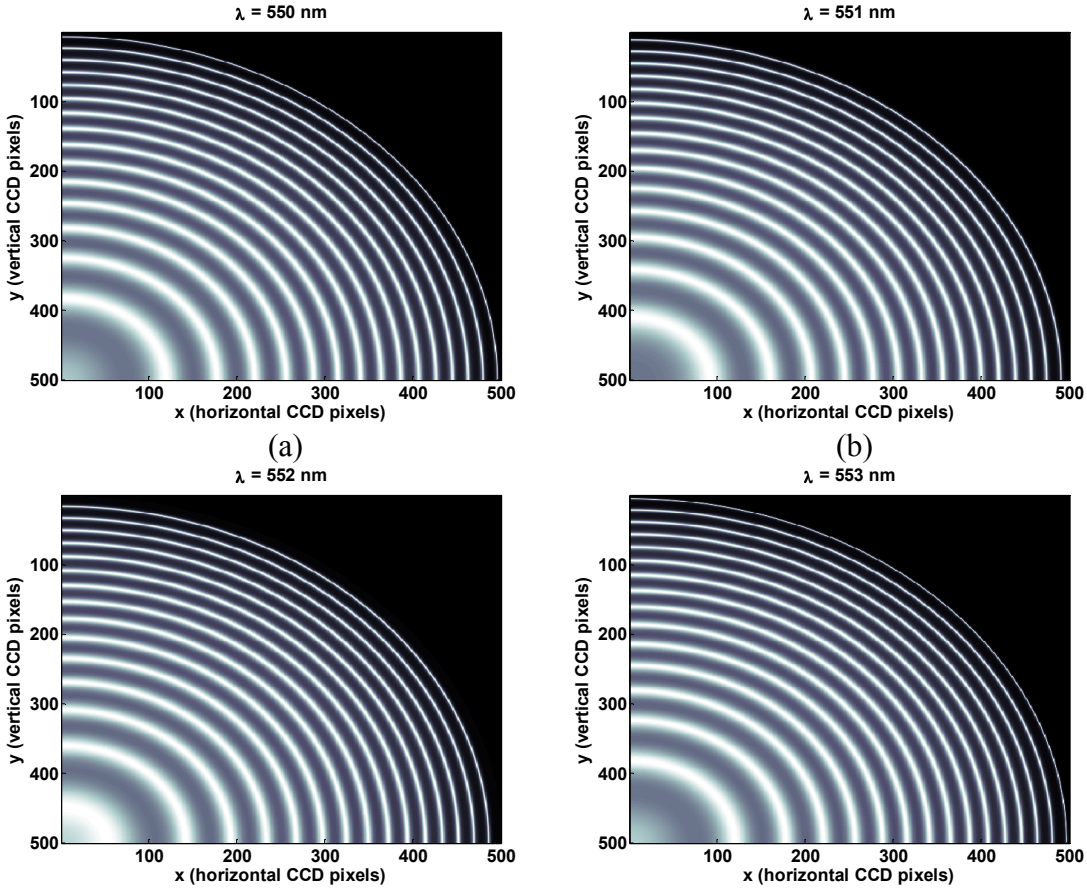

Figure 2.2. Circularly symmetric fringes formed at the Fourier plane of the spherical lens on the CCD as a result of diffuse light illumination of the thin film shown in Figure 2.1.

Figure 2.3 shows altogether the spatial-spectral patterns taken along a radial direction in Figures 2.2(a)-(d) at different wavelengths. The first observation confirms the high resolution of the titania film as the spectral channels with only 1 nm wavelength difference are clearly resolved in this figure. In contrast to its high resolution, the titania film has a very small spectral bandwidth limited by its free spectral range (FSR). This is obviously seen in Figure 2.3 where the spatial response of the λ = 553 nm almost covers that of the λ = 550 nm. Same conclusion can be made in comparing Figures 2.2(a) and (d) where they do look similar. Therefore, the periodicity in the spectral response of interferometers severely restricts the accessible spectral range because the output image on the CCD is degenerate for wavelength spaced by the FSR meaning that the utility of this kind of spectrometer for broad source analysis is constrained.

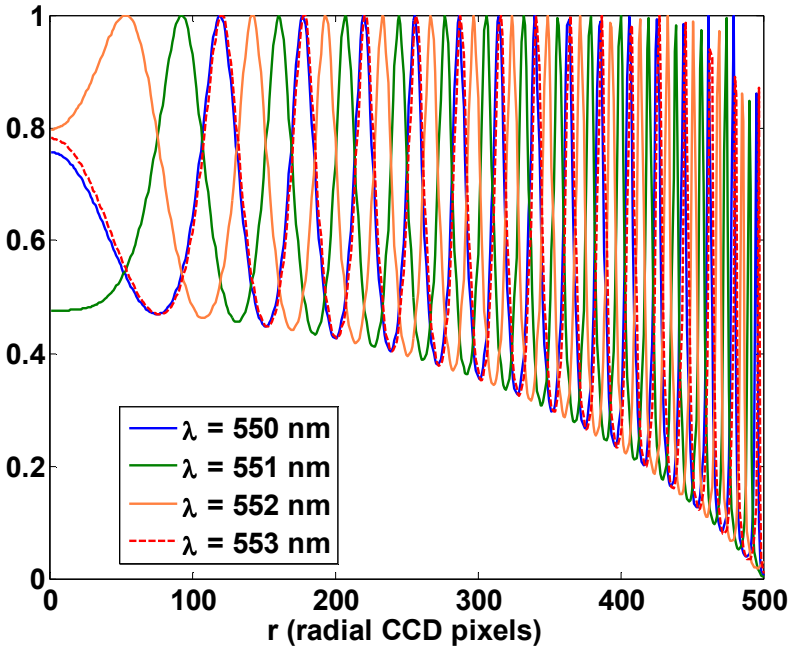

Figure 2.3. Periodic spectral transmission response of the spectrometer shown in Figure 2.1 with FSR = 3 nm. The spectrum of the titania film is degenerate beyond its FSR as evidenced by the overlap of the transmission response at λ = 553 nm and that at λ = 550 nm.

2.1.2. Fabry-Perot Etalons

The second and more remarkable demonstration of the interferometric spectrometers is based on a FPE [20, 21]. FPEs are popular for their extremely high resolutions and they are widely used for the measurement of very sharp atomic spectral lines. To study the operation principle of the Fabry-Perot interferometers under diffuse light illumination we choose a fixed-gap etalon as shown in Figure 2.4. It is composed of two parallel highly reflecting dielectric mirrors with the reflectivity R = 0.9 and the air-gap distance d = 50 μm. The air-gap etalon has a frame or spacers which hold mirrors at a fixed distance. Similar to the previous study for the thin film spectrometer, the input beam is a TE polarized diffuse beam and the CCD is at the focal plane of the lens. Figures 2.5(a)-(d) show the spatial-spectral responses of the FPE spectrometer for four successive spectral channels 550-553 nm, respectively. Once again the spatial pattern along the azimuthal direction on the CCD is redundant and all the spectral information can be extracted from the pattern along the radial direction. Thus, the challenge of achieving a 2D spatial-spectral response is yet remained to be solved.

The FSR of the FPE is calculated using the following formula [62],

$$FSR = \frac{\lambda^2}{2nd} \tag{2.4}$$

and it is almost 3 nm around the λ = 550 nm. Thus, the CCD images in Figure 2.5(a) for λ = 550 nm and Figure 2.5(d) for λ = 553 nm look similar. Figure 2.6(a) shows altogether the CCD outputs along a radial direction in Figures 2.5(a)-(d) for different wavelengths. It is clear that the output pattern at λ = 553 nm almost coincides with that at λ = 550 nm which is consistent with FSR = 3 nm. This observation confirms the degeneracy in the

spectral response of the FPE spectrometer beyond its FSR and limits its applicability to only a 3 nm bandwidth.

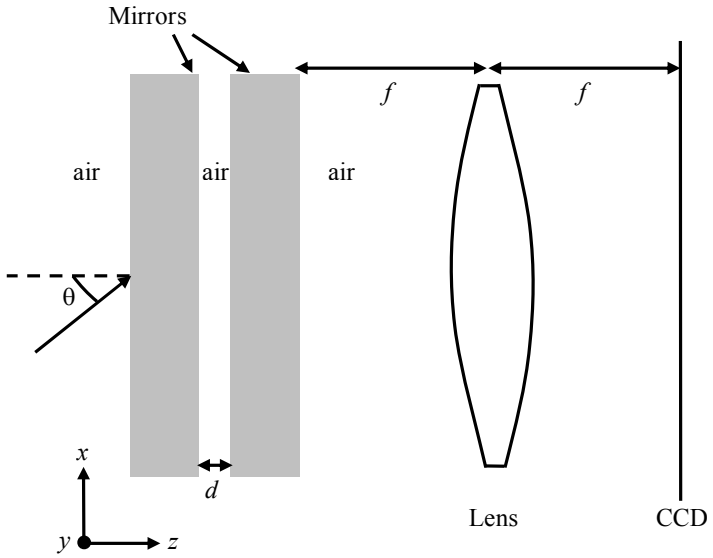

Figure 2.4. Schematic of a FPE spectrometer. The FPE is composed of two parallel highly reflecting dielectric mirrors with the reflectivity $R = 0.9$ and the air-gap distance $d = 50$ μm. The spectral information of the input diffuse beam is mapped into its spatial pattern at the Fourier plane of the lens on the CCD.

Using the estimate given in Equation (2.3), the resolution of the FPE is calculated to be $\Delta\lambda_{1/2} = 0.1$ nm (i.e., 1 Å) while it is $\Delta\lambda_{1/2} = 1.8$ nm for the titania film. Therefore, almost 20 times better resolution than thin film is achieved with FPE. The high resolution of the FPE is also seen from Figure 2.6(b) where the two 1 Å spaced wavelength channels are resolved clearly. Moreover, by comparing the Figures 2.3 and 2.6(a), one can see the extinction ratio of the FPE is very much higher than that of the titania film as a result of its higher reflectivity. Considering all the advantages together, FPEs look more promising interferometric spectrometers than thin films. However, both demonstrations suffer from the very small spectral bandwidth which is equal to their FSR.

To summarize, the interferometric spectrometers have high resolution and small spectral bandwidth. They can work under diffuse light illumination and result in 1D spatial-spectral mapping on the CCD. Nevertheless, to improve their performance, we can integrate them with a diffractive element to not only increase their operation bandwidth but also break their spatial-spectral response symmetry. The collective spectrometer then can result in a 2D invertible mapping between target spectrum and CCD image. Prior to proposing the combined spectrometer, we study diffractive elements as tentative supplements to improve interferometers functionality.

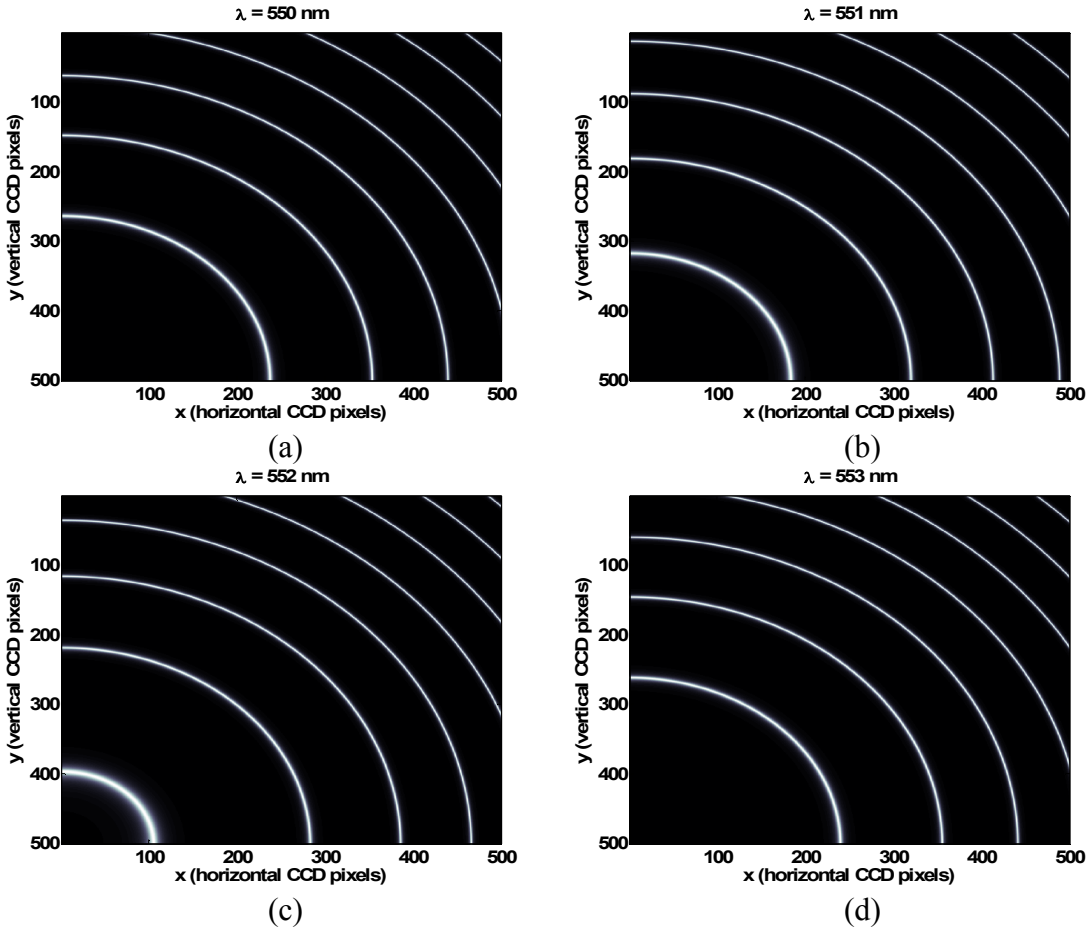

Figure 2.5. Circularly symmetric fringes formed at the Fourier plane of the spherical lens on the CCD as a result of diffuse light illumination of the FPE shown in Figure 2.4. The spatial patterns shown in (a), (b), and (c) are all different from each other along the radial direction. However, the patterns of (a) and (d) look similar which confirms the FSR of 3 nm for the FPE used here.

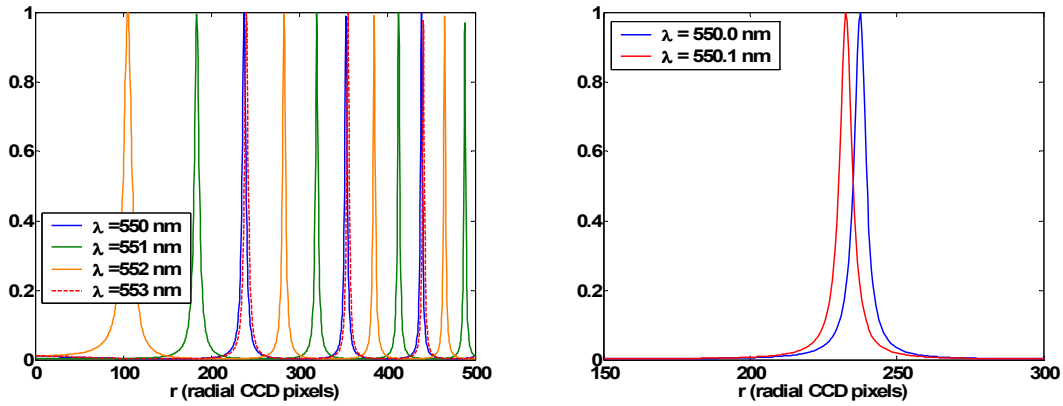

(a) (b)

Figure 2.6. (a) Periodic spectral transmission response of the FPE spectrometer shown in Figure 2.4 with FSR = 3 nm along the radial direction. The spectrum of the FPE is degenerate beyond its FSR as evidenced by the overlap of the transmission response at λ = 553 nm and that at λ = 550 nm. (b) The spatial responses of two channels with only 1 Å wavelength difference are shown for the verification of the ultra-high resolution of the FPEs.

2.2. Diffractive Spectrometers

The second major type of spectrometers is diffractive spectrometers. They work based on the principle that different incident wavelengths are diffracted in different angles. Therefore, they separate an incident polychromatic beam into its constituent wavelength components. Two widely used examples of the diffractive spectrometers are diffraction gratings and volume holograms which are analyzed in this section.

2.2.1. Thin Gratings

The schematic of a spectrometer composed of a thin diffraction grating is shown in Figure 2.7. The grating has a thickness of d_g = 5 μm, a period of Λ = 0.5 μm, and it has been recorded in a photorefractive material with n_g = 1.5. The grating is illuminated by a TE diffuse beam and its diffraction pattern is captured on the CCD at the focal plane of the lens. Figures 2.8(a) and (b) show the diffraction patterns of the thin grating for two different wavelengths λ = 500 nm and λ = 600 nm, respectively. Similar to

interferometric spectrometers discussed in the previous section, grating has also a 1D spatial-spectral pattern. All the spectral information is encoded along the *x* direction and the pattern along the vertical dimension of the CCD has redundant information. To analyze the spectral response of the thin grating we just need to look at a horizontal row of the CCD image. Figure 2.9 shows the spatial patterns along a horizontal row on the CCD images in Figure 2.8 when both normalized to their peak values. As it is observed from this figure the thin grating has a very poor resolution as barely can resolve a 100 nm wavelength difference. Such a low resolution device is not practically valuable and thus, we conclude that the thin diffraction gratings are not useful for the diffuse light spectroscopy.

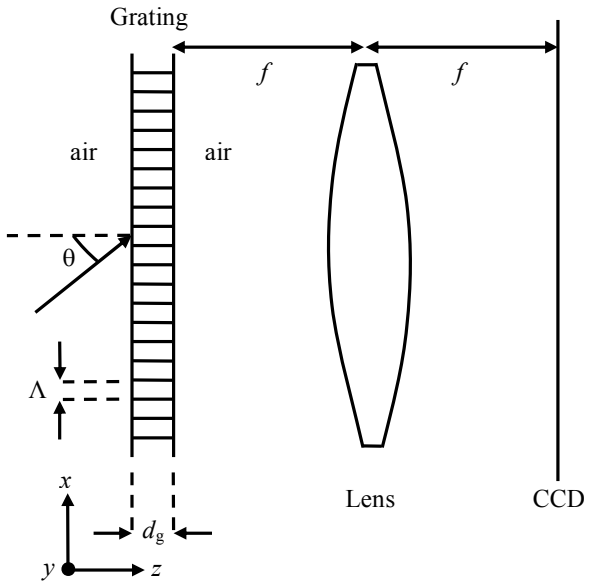

Figure 2.7. Schematic of a grating spectrometer. The grating has a period of Λ = 0.5 μm, and it has been recorded in a photorefractive material with n_g = 1.5. The spectral information of the input diffuse beam is mapped into its spatial pattern at the Fourier plane of the lens on the CCD.

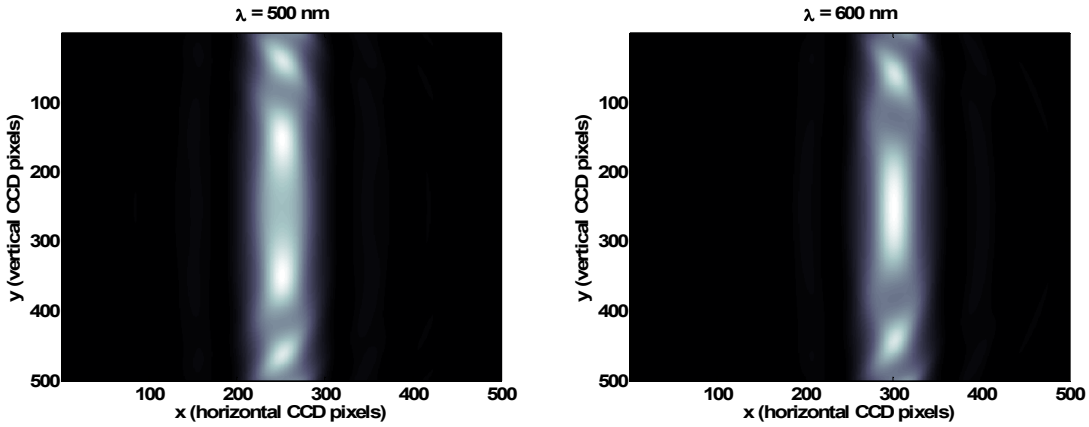

(a) (b)

Figure 2.8. Diffraction patterns formed at the Fourier plane of the spherical lens on the CCD as a result of diffuse light illumination of the grating shown in Figure 2.7. The grating thickness is d_g = 5 μm. The diffraction patterns of the different wavelength channels are only displaced along the *x* direction.

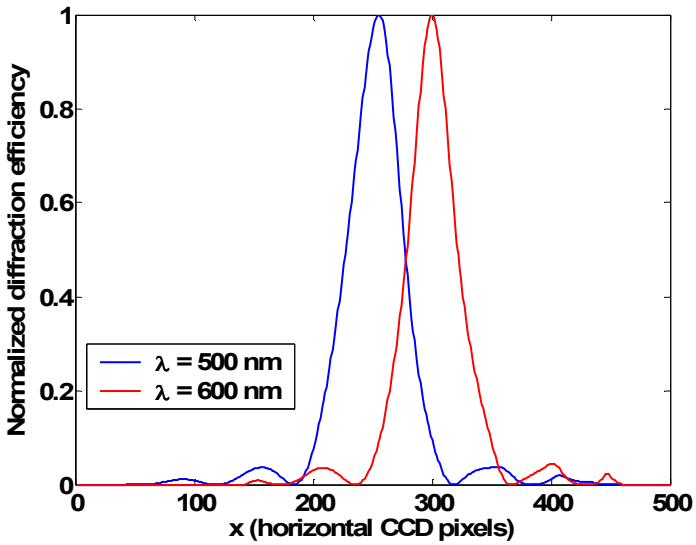

Figure 2.9. The spatial responses of the two channels in Figure 2.8 along a horizontal row on the CCD are shown. Both curves are normalized to their peak values.

2.2.2. Thick Gratings

To make practical spectrometers based on the diffraction gratings, one can thicken the photorefractive material which substantially results in higher resolution. Here we have used a thick grating with the thickness of d_g = 50 μm. All the other parameters are the same as the last simulation. Figures 2.10(a) and (b) show the CCD images for

wavelengths λ = 550 nm and λ = 560 nm, respectively. The output pattern corresponding to each wavelength is a bright stripe along the *y* direction. Once again, by looking into the spatial patterns along a horizontal row on the CCD images, we can confirm its higher resolution which is about 10 nm as shown in Figure 2.11. Despite of diffracting diffuse incident light, the thick gratings are yet low resolution and are not practically useful.

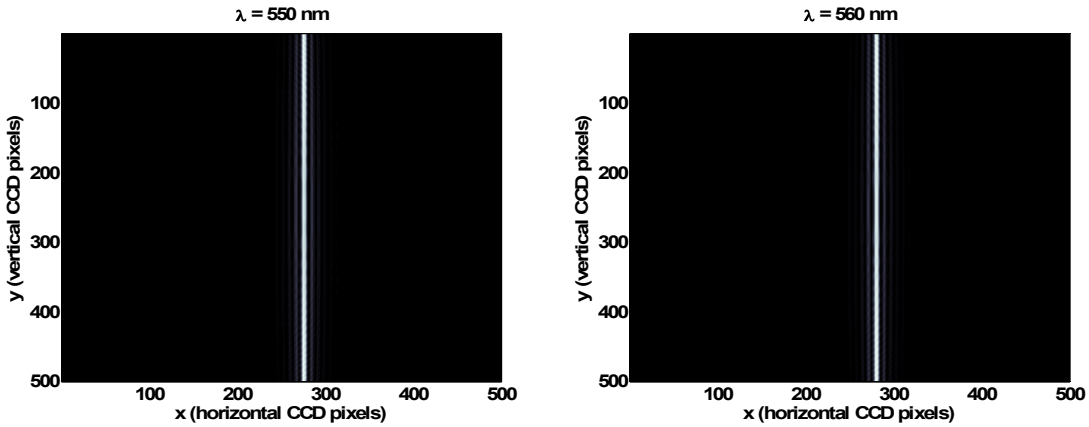

(a) (b)

Figure 2.10. Diffraction patterns formed at the Fourier plane of the spherical lens on the CCD as a result of diffuse light illumination of the grating shown in Figure 2.7. The grating thickness is d_g = 50 μm. The diffraction patterns of the different wavelength channels are only displaced along the *x* direction.

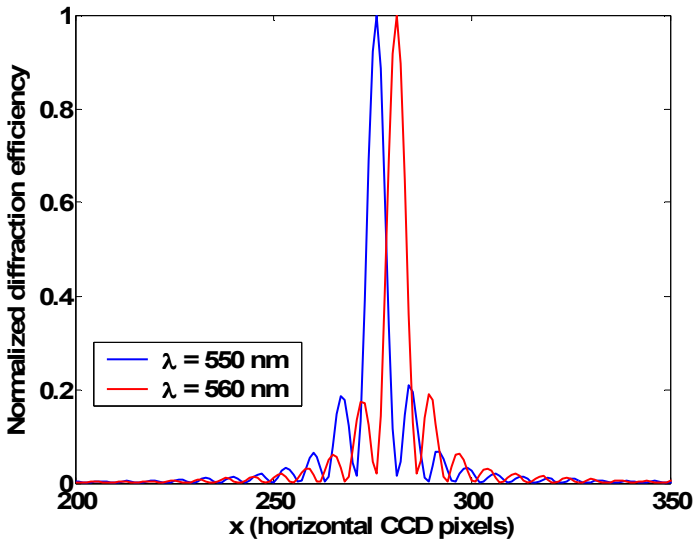

Figure 2.11. The spatial responses of the two channels in Figure 2.10 along a horizontal row on the CCD are shown. The resolution of 10 nm is obviously seen in the figure.

2.2.3 Volume Holograms

For achieving higher resolution while functioning under diffuse incident beam, we propose volume holograms as a new class of diffractive spectrometers. Volume holograms are essentially very thick diffractive gratings where the thickness of the recording material can be up to a few hundred nanometers or even thicker in the order of a few millimeters. In addition to their higher resolution over thick gratings, they can be potentially designed for achieving a desired performance by adjusting their recording geometry. Spherical beam volume holograms (SBVHs) have been already proposed and extensively investigated for diffuse light spectroscopy [16-19]. However, as it will be shown later in this chapter, because of some practical issues they are not of our interest. Here, we explore another type of volume holograms, i.e., cylindrical beam volume holograms (CBVHs), which are capable of performing high resolution diffuse light spectroscopy [63]. We will show later that CBVHs have a great advantage over the SBVHs for making a combined interferometric diffractive spectrometer.

The CBVH is recorded using a plane wave and a cylindrical beam generated by focusing another plane wave using a cylindrical lens in the arrangement shown in Figure 2.12 with d_1 = 2.5 cm and d_2 = 2.7 cm. The angle of incident of the plane wave in the air is 36° and the cylindrical beam propagates normal to the hologram. The recording material is a 2 mm thick $LiNbO_3$:Fe:Mn crystal and the recording wavelength is λ = 532 nm. During the recording the crystal is sensitized using a beam at λ = 404 nm from a diode laser.

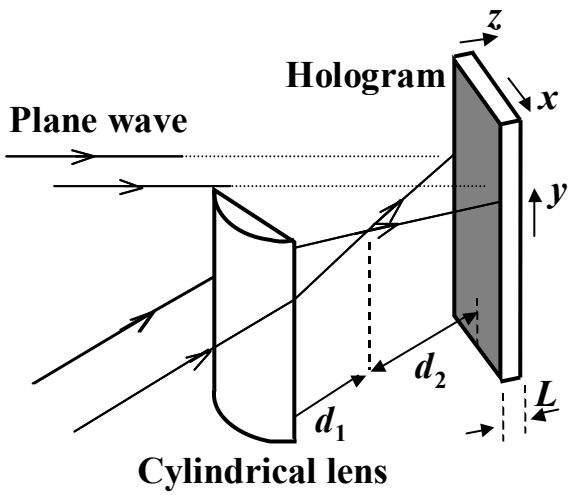

Figure 2.12. Recording geometry for a CBVH. The hologram is recorded using a plane wave and a cylindrical beam formed by passing a plane wave through a cylindrical lens. The focal plane of the cylindrical beam is at distance d_1 = 2.5 cm behind the lens and at distance d_2 = 2.7 cm in front of the hologram. The recording material is a 2 mm thick $LiNbO_3$:Fe:Mn crystal.

The CBVH has almost the same properties as the SBVH in the *x* direction while it does not affect the beam in the *y* direction. This can be realized from the plane wave expansion of both the spherical beam and the cylindrical beam. The expansion of a spherical beam at distance $\mathbf{r} = (x, y, z)$ from a point source at $\mathbf{r_0} = (0, 0, -d)$ as a set of plane waves is [64]

$$\frac{1}{|\mathbf{r}-\mathbf{r}_0|}e^{jk|\mathbf{r}-\mathbf{r}_0|} = \frac{j}{2\pi}\iint\frac{1}{k_z}e^{jk_z(z+d)}\ e^{j(k_x x+k_y y)}dk_x dk_y\ , \tag{2.5}$$

where k_x, k_y, and k_z are the *x*, *y*, and the *z* components of the wave vector **k**. The amplitude of the wave vector **k** is the wave number $k = 2\pi/\lambda$. Similarly, the cylindrical beam, with the axis parallel to *y*-axis, originated from a line source at $\mathbf{r_0} = (0, y, -d)$ and monitored at $\mathbf{r} = (x, y, z)$ can be represented by its Fourier transform as

$$\frac{1}{\sqrt{|\mathbf{r}-\mathbf{r}_0|}}e^{jk|\mathbf{r}-\mathbf{r}_0|} = \frac{1}{4\pi}\int\frac{1}{k_z}e^{jk_z(z+d)}\ e^{jk_x x}dk_x\ . \tag{2.6}$$

Note that in Equation (2.6) $k_y = 0$ and, therefore, $k_x^2 + k_z^2 = k^2$, where k is the wave number. Also, note that the relation in Equation (2.6) is valid for all values of y. If we assume paraxial approximation for the beam propagating primarily in the z direction (*i.e.*, $k_z >> k_x$), the Fourier transform relation in Equation (2.6) can be written as

$$\frac{1}{\sqrt{|\mathbf{r}-\mathbf{r}_0|}} e^{jk|\mathbf{r}-\mathbf{r}_0|} = \frac{e^{jk(z+d)}}{4\pi} \int \frac{1}{k_z} e^{-j\frac{k_x^2}{2k}(z+d)} \; e^{jk_x x} dk_x \; . \tag{2.7}$$

As we know from the analysis of the SBVH [18], the quadratic phase in the x direction that is recorded as a hologram provides the desired dispersion properties. From Equation (2.7) it is clear that the hologram recorded using a plane wave and a cylindrical beam shows the quadratic phase behavior in the x direction (*i.e.*, $\exp[-jk_x^2(z+d)/2k]$ term in the Fourier domain). For the SBVH the quadratic phase is observed in both x and y directions, while in the case of the CBVH, it is only observed in the x direction. In the y direction, however, the signal is not affected by the hologram.

The schematic of the CBVH spectrometer is as Figure 2.7 where a cylindrical lens is used in place of the spherical one. The output pattern on the CCD corresponding to each wavelength is a bright stripe in the y direction as shown in Figure 2.13, where the location of this stripe changes in the x direction as λ changes. Hence, its spatial-spectral mapping is 1D. We can verify its large bandwidth from this figure since it is working from λ = 500 nm all the way to λ = 600 nm. Moreover, in Figure 2.14 we have shown the spatial responses of the two channels, i.e., λ = 550 and λ = 553, along a horizontal row on the CCD. As seen in this figure, the two diffracted stripes are clearly resolved which indicates a resolution better than 3 nm. Therefore, in contrast to typical diffraction gratings, CBVHs demonstrate higher resolution in diffuse light spectroscopy.

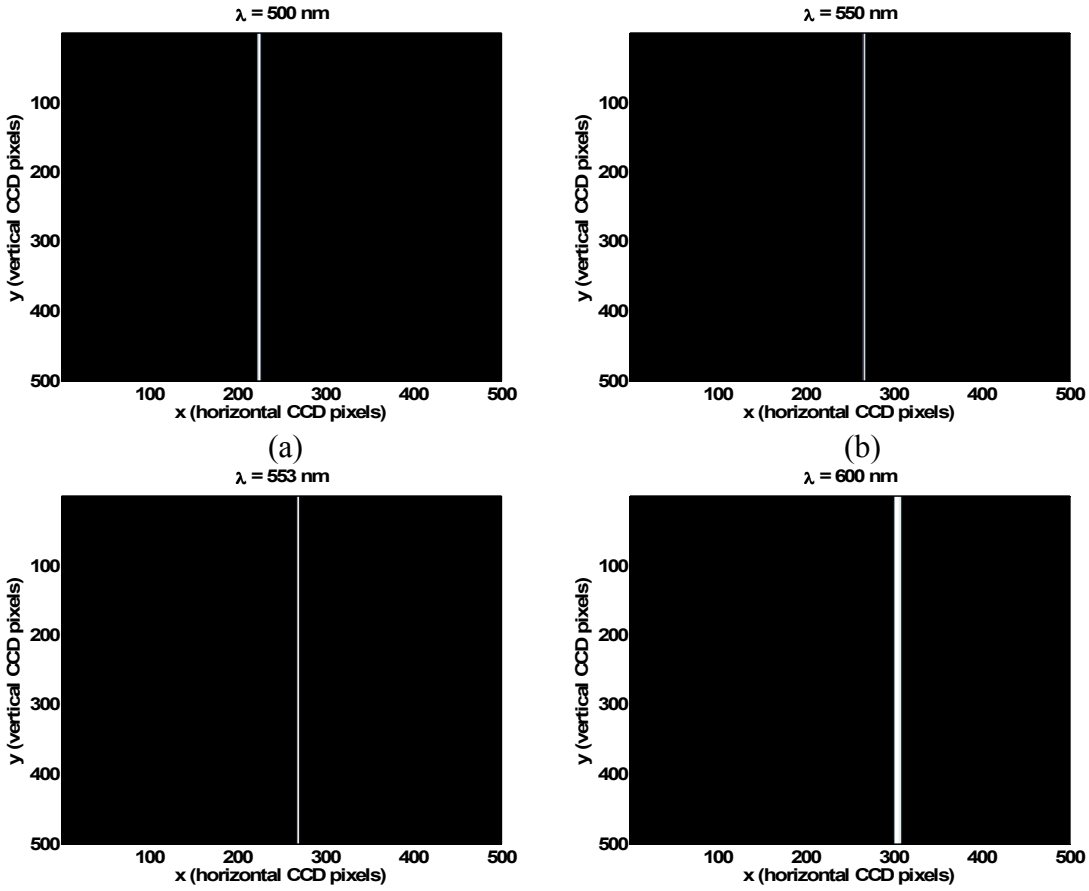

Figure 2.13. Diffraction patterns formed at the Fourier plane of the cylindrical lens on the CCD as a result of diffuse light illumination of the CBVH. The diffraction patterns of the different wavelength channels are only displaced along the *x* direction.

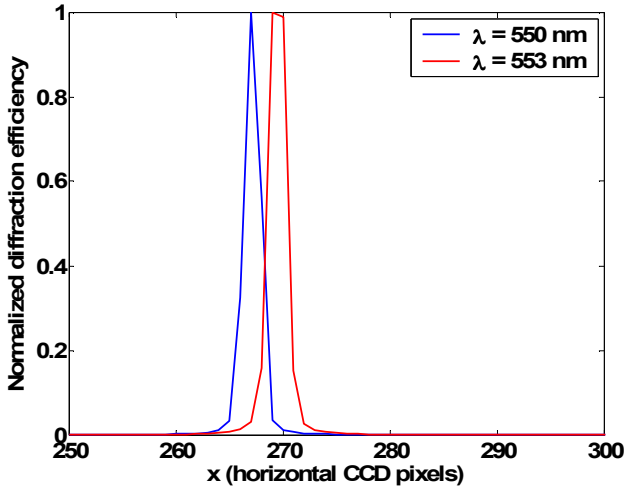

Figure 2.14. The spatial responses of the two channels in Figures 2.10(b) and (c) along a horizontal row on the CCD are shown. The resolution of better than 3 nm is obviously seen in the figure.

To summarize, unlike the interferometric spectrometers, the diffractive spectrometers have low resolution and large spectral bandwidth. They can work under diffuse light illumination and result in 1D spatial-spectral mapping on the CCD.

2.3. Tandem FPE-CBVH Spectrometer

Now we propose an elite spectrometer in a tandem configuration of an interferometer and a diffractive spectrometer to benefit from both the high resolution and the large spectral bandwidth simultaneously. To function under diffuse light illumination and for achieving the highest performance, we choose the best element of each category discussed earlier, the Fabry-Perot etalon as an ultra high resolution interferometer and the CBVH as a very efficient large bandwidth diffuse spectrometer.

The schematic of the tandem FPE-CBVH spectrometer has been shown in Figure 2.15. The CCD is placed in the simultaneous focal planes of the two cylindrical lenses L_1 and L_2. The lenses L_1 and L_2 perform the spatial Fourier transformation on the output beam of the spectrometer in the x and y directions, respectively. Figure 2.16(a) shows the output pattern of the tandem spectrometer on the CCD for $\lambda = 550$ nm. This pattern is formed by intersection of the circular fringes [Figure 2.5(a)] and the vertical stripe [Figure 2.13(b)]. As seen in the figure, the CBVH simply breaks the circular symmetry of the FPE interference fringes and the FPE simply removes the y degeneracy from the CBVH spectrum to from a 2D spatial-spectral pattern in the co-Fourier plane of the two cylindrical lenses. In Figure 2.16(b), we have shown the spatial-spectral response of the tandem spectrometer to a multi-wavelength diffuse input beam composed of $\lambda = 500$ nm, $\lambda = 550$ nm, and $\lambda = 550.1$ nm. As the first observation, the bandwidth of the tandem spectrometer is no longer limited by the FSR of the FPE since the spatial pattern of $\lambda =$

550 nm can be distinguished from that of λ = 500 nm. Second, it can easily resolve between λ = 550 nm and λ = 550.1 nm which indicates a resolution better than 0.1 nm. Therefore, in tandem FPE-CBVH spectrometer, we can indeed achieve the high resolution as well as the large bandwidth. Besides, the tandem spectrometer results in a 2D spatial-spectral pattern on the CCD.

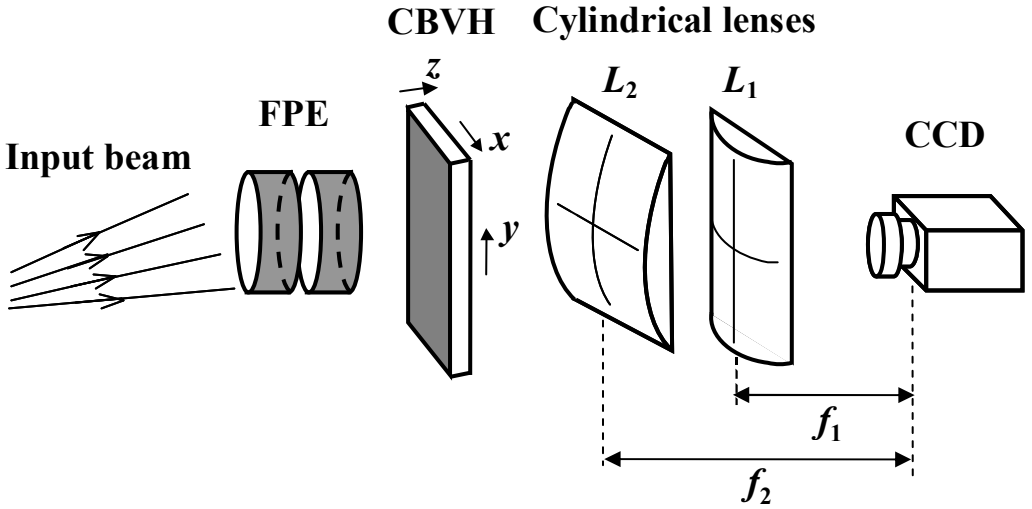

Figure 2.15. Schematic of the tandem FPE-CBVH spectrometer. The spectral information of the input diffuse beam is mapped into a 2D spatial-spectral pattern at the co-Fourier plane of both cylindrical lenses on the CCD. The horizontal cylindrical lens forms the FPE spatial-spectral pattern and the vertical one makes the diffracted orders of the CBVH on the CCD.

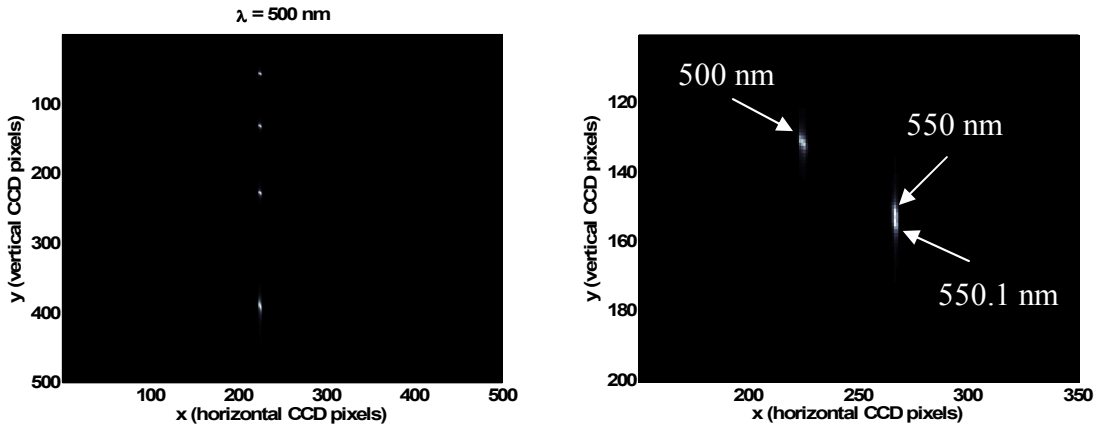

(a) (b)

Figure 2.16. (a) The output pattern of the tandem spectrometer on the CCD for λ = 550 nm is shown. (b) The spatial-spectral response of the tandem spectrometer to a multi-wavelength diffuse input beam composed of λ = 500 nm, λ = 550 nm, and λ = 550.1 nm is shown.

The significant advantage of the CBVH over other types of volume holograms is that it does not alter the beam in the *y* direction which makes the function of tandem spectrometer along *x* and *y* directions independent. Hence, we can design the FPE to encode the high resolution spectral information along the *y* direction and the CBVH to expand the spectral operating range along the *x* direction. In other words, we can think of a two-step mechanism to achieve high resolution and large operation bandwidth in this spectrometer. A coarse resolution in a large spectral range is obtained by the CBVH while a finer resolution is obtained by the FPE inside the coarse resolution of the CBVH. In the optimal spectrometer, the resolution of the CBVH will be equal to the FSR of the FPE so that the fine resolution of the tandem spectrometer is defined by the FPE resolution and its operation bandwidth is defined by the CBVH. In this optimal spectrometer, the best performance is achieved in a very compact structure. Note that for spectrometers in which the FSR of the FPE is smaller than the resolution of the CBVH, spectral ambiguity exists in the *y* direction (the direction of fine-resolution due to the FPE). Thus, to remove the ambiguity in resolving the spectrum of the unknown source we have to strictly enforce a precondition that the CBVH resolution is at best equal to the FSR of the FPE. This guarantees the 2D spatial-spectral mapping is invertible and there is no singularity in the spectrum estimation process. On the other hand, for spectrometers in which FSR of the FPE is larger than the resolution of the CBVH (for spatial coding in the *x* direction), the vertical (i.e., *y*) dimension is not optimally used for coding using the FPE. Only the spatial range or the CCD pixels corresponding to the wavelength range equal to the CBVH resolution are used resulting in reduction in the resolution.

In the following chapter we report on the experimental demonstration of tandem FPE-CBVH spectrometer and we use it to estimate the spectrum of an unknown input diffuse beam with very sharp spectral lines.

CHAPTER 3

EXPERIMENTAL DEMONSTRATION OF ULTRA-HIGH RESOLUTION TANDEM FABRY-PEROT ETALON CYLINDRICAL BEAM VOLUME HOLOGRAM SPECTROMETER

In this chapter we demonstrate a compact and slitless spectrometer with high resolution formed by cascading a Fabry-Perot etalon (FPE) and a cylindrical beam volume hologram (CBVH). The most significant advantage of this combined spectrometer is that we can independently encode spectral information of a diffuse beam in a two-dimensional (2D) plane. Also, we show in this slitless configuration we can simultaneously benefit from the advantages of both elements, the high resolution of the FPE and the large spectral range of the CBVH. Here, we report on the experimental demonstration of a spectrometer with better than 0.2 nm resolution [65].

The basic property of a spectrometer is to map different wavelength channels of the input beam into different spatial patterns in the output plane using an interferometric and/or a dispersive element. The simplest form of this mapping (which is usually done in conventional spectrometers) is to map each wavelength channel to a distinct spatial location (for example, along a line) in the output plane. The intensity distribution of the output is then detected by a detector array or a charged coupled device (CCD). By calibration of the spectrometer and inversion of the detected data, we can estimate the spectrum of an unknown input source [25]. For spectrometers with 1D spatial-spectral mapping, spectral information is encoded in only one spatial dimension and the measurement capabilities of the other dimension are not utilized for improving the

performance of the spectrometer. One major consequence of such 1D mapping is the trade-off among resolution, operation bandwidth, and throughput (or sensitivity), which is a major drawback of conventional spectrometers for sensing applications with weak input signals. There have also been some recent reports using coded aperture spectrometers for 2D spatial-spectral mapping with excellent experimental results [66].

Recently, a new class of volume holographic spectrometers [16] has been reported which do not require any collimation optics. These spectrometers rely on the unique Bragg selectivity and diffractive properties of a spherical beam volume hologram (SBVH) [16, 19] or a CBVH [63] to measure the spectrum of an unknown source. While the resulting spectrometers are very compact, alignment insensitive, inexpensive, and flexible for design, they still work based on the 1D spatial mapping of the spectral information. Among different holographic spectrometers, the ones using CBVH have shown better flexibility for designing new classes of spectrometers as they do not affect the input light in one direction and perform the spatial-spectral mapping in the other direction [63].

3.1. Experimental Results

The schematic of the tandem FPE-CBVH spectrometer that we investigate in this chapter has been shown in Figure 2.15. The FPE is composed of two dielectric mirrors with the fixed air gap (which is 50 μm wide) between them. The reflectivity of each mirror at the wavelength range used here (530 nm < λ < 600 nm) is close to 96%. The CBVH is recorded using a plane wave and a cylindrical beam obtained by focusing a separate plane wave using a cylindrical lens in the arrangement shown in Figure 1(b) with d_1 = 2.5 cm and d_2 = 2.7 cm. The angle of incident of the plane wave in the air is 36° and the

cylindrical beam propagates normal to the hologram. The recording material is a 2 mm thick $LiNbO_3$:Fe:Mn crystal and the recording wavelength is λ = 532 nm. During the recording the crystal is sensitized using a beam at λ = 404 nm from a diode laser. The CCD is placed in the simultaneous focal planes of the two lenses L_1 (with focal length f_1 = 2.5 cm) and L_2 (with focal length f_2 = 5.1 cm) as seen in Figure 2.15. The lenses L_1 and L_2 perform the spatial Fourier transformation on the output beam of the CBVH in the *x*- and *y*-directions, respectively.

The performance of the spectrometer based on only a CBVH can be found similar to what outlined in Reference [63]. The output pattern on the CCD corresponding to each wavelength is a bright stripe in the *y* direction as shown in Figure 3.1(a), where its width depends principally on the thickness of the CBVH. The location of this stripe changes in the *x* direction as λ changes as shown in Figure 3.1(b). It should be noted that the CBVH spectrometer works well for diffuse light [63]. However, in contrast to the FPE spectrometer, the CBVH spectrometer has lower resolution (close to 3 nm for our CBVH) but larger operation bandwidth (more than 100 nm for our CBVH).

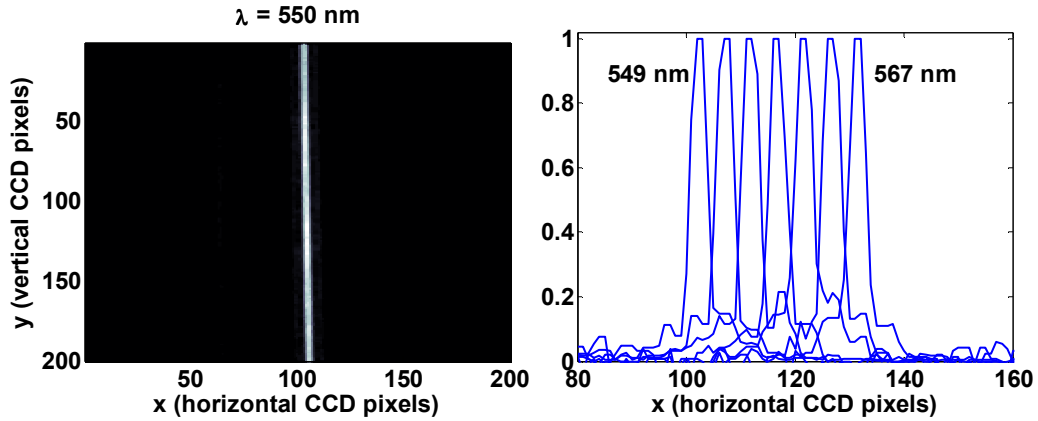

(a) (b)

Figure 3.1. (a) Diffraction pattern of the CBVH formed on the CCD at the Fourier plane of the cylindrical lens with f = 2.5 cm for diffuse light illumination at λ = 550 nm. (b) Spatial-spectral responses of the CBVH along the *x* direction in (a) for different incident wavelengths from λ = 549 nm to λ = 567 nm with 3 nm steps.

The main rationale for forming the tandem spectrometer is to combine the unique features of these two dispersive elements (FPE and CBVH) and at the same time cover each one's deficiency by the other one's capability. Furthermore, since both elements work well under diffuse light illumination, a simple and compact slitless design can be implemented to combine the two elements. In this formation, we use the CBVH to separate the input spectrum into horizontal regions (i.e., stripes) each smaller or equal in bandwidth to the FSR of the FPE. Then, the FPE divides the operation range of each stripe into very small regions with very small wavelength differences (i.e., very high resolution) in the vertical direction. Figure 3.2 shows the spatial-spectral pattern of the tandem spectrometer on the CCD for three different wavelengths: 540.2 nm, 553.2 nm, and 575.4 nm. As clearly seen in this figure, by changing the input wavelength the spatial pattern on the CDD moves in both x and y directions. Thus, the overall spectrometer performs a true 2D spatial-spectral mapping of the input spectrum. The key aspect of this design is to have the right relation between the FSR of the FPE and the resolution of the CBVH. It is noteworthy to mention that combination of interferometric and diffractive elements has been demonstrated previously [67-69], however the tandem spectrometer suitable for diffuse source spectroscopy is presented here for the first time.

Figure 3.3 shows the output pattern of the CCD when the input to the tandem spectrometer is diffuse light from a Hg-Ar lamp with three distinct sharp peaks at 546 nm, 577 nm, and 579 nm. The 2D spatial-spectral mapping is evident from Figure 3.3. It is interesting to note that the 546 nm line is separated horizontally (by the CBVH) from the other two lines as its wavelength difference with those two is larger than the

resolution of the CBVH. However, the two lines at 577 nm and 579 nm are separated vertically (by the FPE) in the output as they fall within the same stripe by the CBVH.

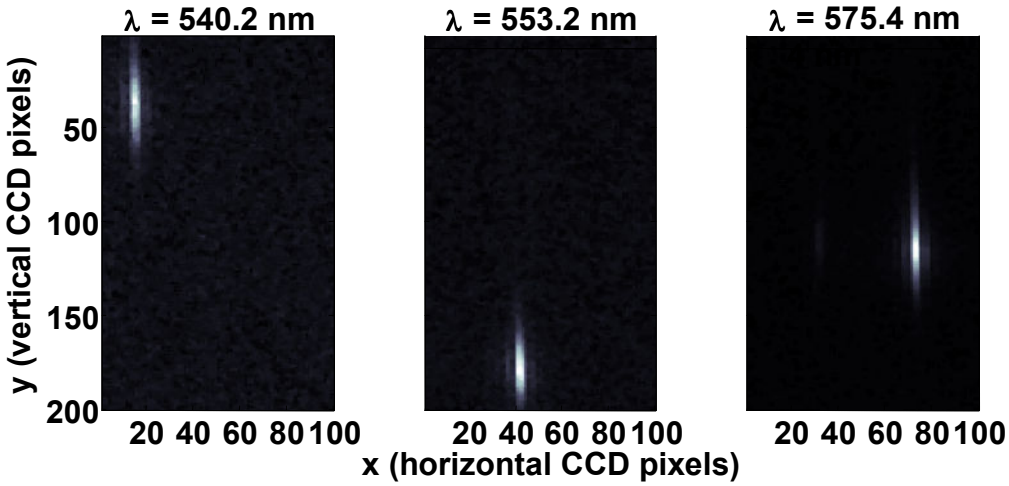

Figure 3.2. Spatial-spectral pattern of the tandem spectrometer on the CCD for three different input wavelengths.

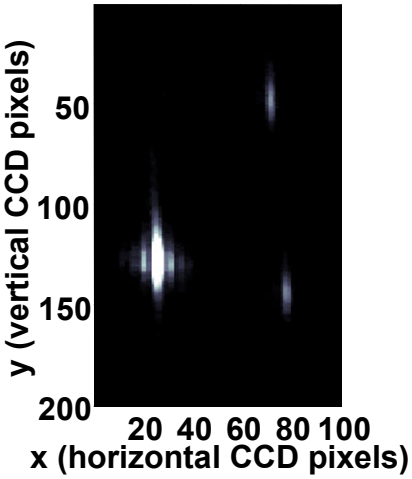

Figure 3.3. The image formed on the CCD corresponding to the diffuse light from an Hg-Ar lamp with three distinct sharp peaks at 546 nm, 577 nm, and 579 nm.

3.2. Spectrum Estimation

As schematically shown in Figure 3.4, the function of any spectrometer is to setup a one to one mapping between the spectrum of the input source, $S(\lambda)$, and the spatial pattern captured on the detector arrays or CCD, $M(\mathbf{r})$, where $\mathbf{r}$ stands for spatial coordinates of

each pixel on the CCD, i.e., (x, y) in Figure 3.3. This invertible mapping between source spectrum and CCD measurements is the spatial-spectral response or transfer function of the spectrometer which is represented by $H(\mathbf{r},\lambda)$ in Figure 3.4. Bandlimited spatial-spectral response of the tandem spectrometer allow source-measurement transformation to be expressed in discrete form as $\mathbf{M} = \mathbf{HS}$, where **M** is an m-tuple measurement vector. **H** is an m-by-n spatial-spectral response matrix of the spectrometer where each row of it represents the spectral response of a specific pixel. Each column of **H** represents the characteristic vector corresponding to a particular spectral channel. **S** is an n-tuple source vector representing the target spectrum.

Now that we have captured the CCD image of the input beam as shown in Figure 3.3, the next step is to invert this image and find the unknown spectrum of the source. To do this inversion process, it is required to have the transfer function **H** of the tandem spectrometer. Because the spatial-spectral response **H** of the tandem spectrometer is not known in advance, a set of calibration sources is used to characterize **H**. To calibrate the tandem spectrometer, we measure the output corresponding to each monochromatic input formed by passing white light through a monochromator with full width at half maximum (FWHM) of 0.2 nm in the entire operation bandwidth. The output beam from the monochromator illuminates a diffuser such that the effective source for the tandem spectrometer is a uniform diffuse beam. This training data defines the system transfer function **H** as shown in Figure 3.5. As seen from this figure the transfer function of the tandem spectrometer looks like a staircase function with perfectly separated spatial-spectral responses in every 3 nm (i.e., bright spots inside the figure). This observation confirms the independent spatial-spectral functionalities of the FPE and CBVH where in

each 3 nm spot the FPE is operating and from one spot to the other the CBVH is operating.

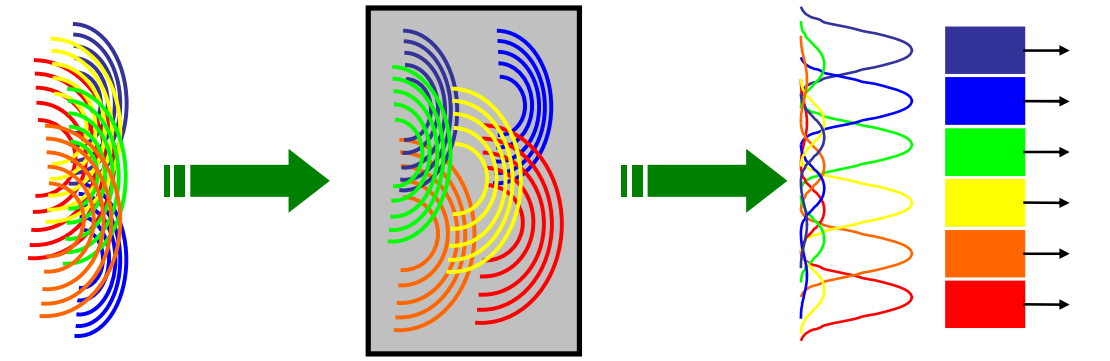

Figure 3.4. The operational principle of any spectrometer is schematically shown. The spectrometer maps the input spectrum $S(\lambda)$ to the detector measurements $M(\mathbf{r})$. This invertible mapping between source spectrum and detector measurements is the spatial-spectral response or transfer function of the spectrometer which is represented by $H(\mathbf{r},\lambda)$ inside the figure.

Now we use the calibrated tandem spectrometer to estimate the spectra of unknown sources over the wavelength range of 540 nm to 585 nm at the resolution of 0.2 nm. Since the number of spectral channels estimated, $(585-540)/0.2=225$, is much less than the number of pixel measurements, $100\times 200=20{,}000$ which is 100 pixels along *x* direction times 200 pixels along *y* direction on the CCD, the measurements over-determine the spectrum. Over-determined problems do not have globally consistent solutions due to the presence of noise, but one can find a solution in the least squares sense. In finding the solution, we have added an additional constraint that the spectral density is non-negative, which makes direct linear least squares inversion impossible. Instead, we have used the Matlab Optimization Toolbox to solve the general nonlinear

optimization problem: $\min_{\mathbf{S}} \|\mathbf{HS}-\mathbf{M}\|_2$ such that $\mathbf{S} \geq 0$, where $\| \ \|_2$ denotes the Euclidean norm [25].

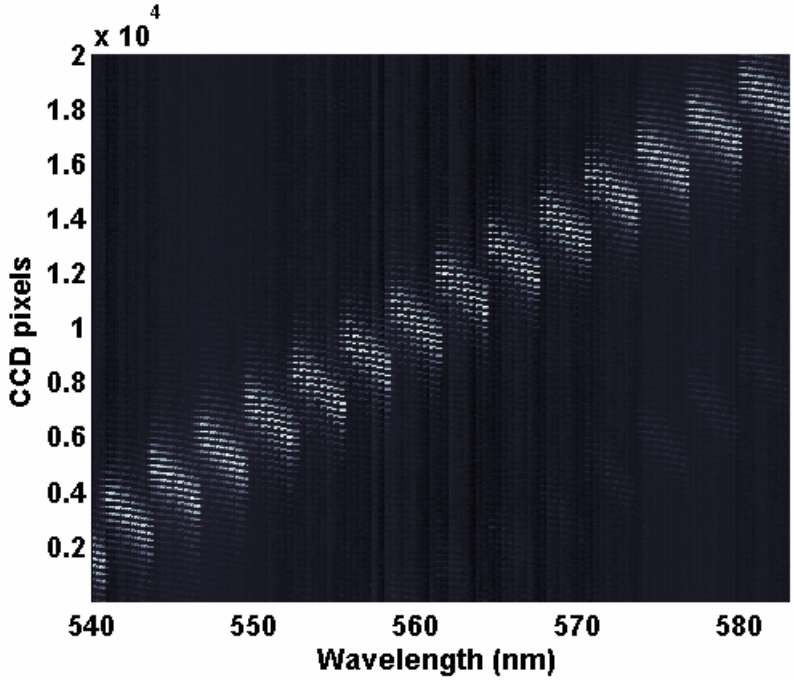

Figure 3.5. The transfer function of the tandem spectrometer in the bandwidth of 540-585 nm is shown. It is composed of separated spots for each 3 nm wavelength range.

Figure 3.6(a) shows the results of the spectrum estimation for the Hg-Ar lamp using our tandem spectrometer. We have also shown the spectrum measured using an Ocean Optics USB2000 spectrometer for comparison. Moreover, to confirm the high resolution capability of our tandem spectrometer and to show its powerful performance, we have compared it with the state of the art and top of the line Oriel InstaSpec ultra-high resolution spectrometer and their excellent agreement is shown in Figure 3.6(b). The results of our estimation agree very well with the lamp data sheet.

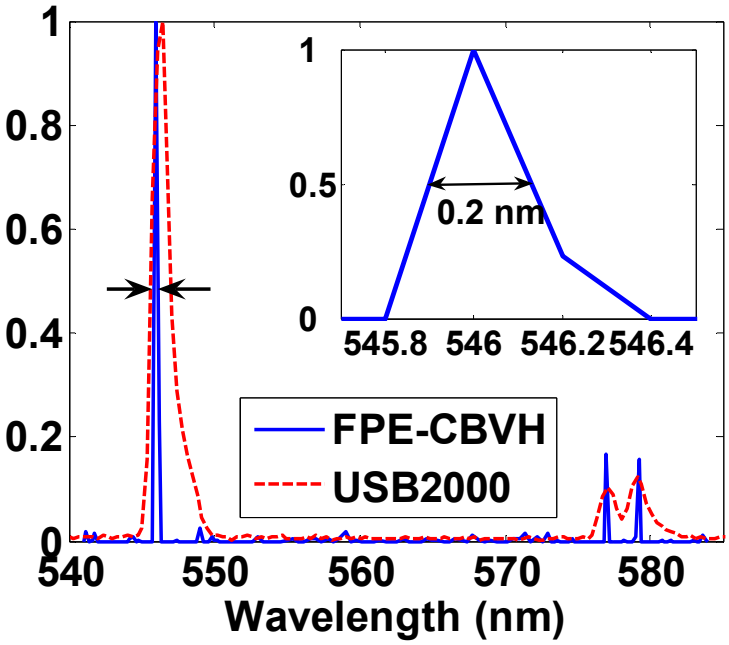

(a)

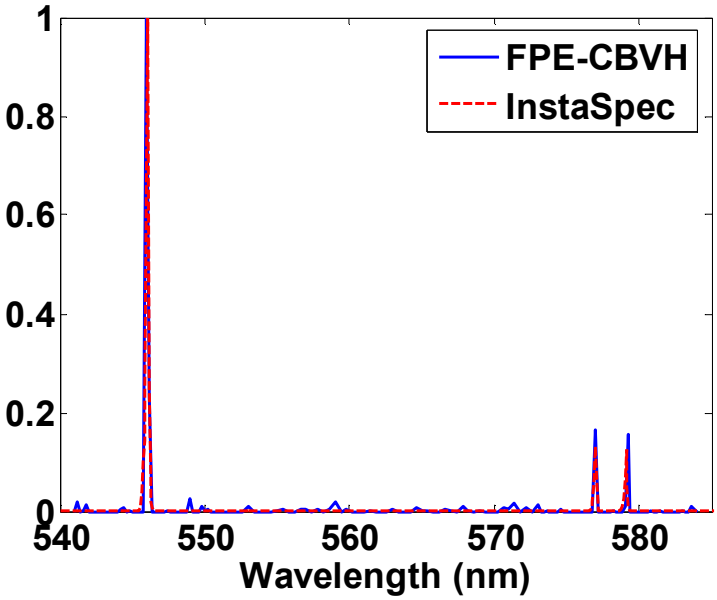

(b)

Figure 3.6. The spectrum of the Hg-Ar lamp measured by the tandem FPE-CBVH spectrometer and (a) an Ocean Optics USB2000 spectrometer and (b) an Oriel InstaSpec spectrometer for comparison.

It is clear from the inset figure that our spectrometer is capable of measuring the fine features of the input light with FWHM of 0.2 nm. Since the resolution of our monochromator is 0.2 nm, we can conclude from this data that the resolution of our

tandem FPE-CBVH spectrometer is better than 0.2 nm. The measurement of the exact resolution requires a more sophisticated monochromator with a resolution much better than 0.2 nm.

A key feature of the proposed spectrometer is its 2D spatial-spectral mapping, which breaks the conventional trade-off between the resolution and the operation bandwidth. Our initial results demonstrate resolution of better than 0.2 nm with operation bandwidth of better than 100 nm using off-the-shelf optics and CCD [65]. Improvement of the operation bandwidth is possible by using the recently proposed spatial multiplexing of a few CBVH along the *y*-direction [63]. It is also worth mentioning that although we obtained high resolution over a considerable bandwidth using the proposed tandem spectrometer, the throughput issue is still present (each wavelength corresponds to a small output region). Nevertheless, it is possible to improve the throughput by using unique properties of volume holograms, especially their multiplexing [70] that allows more sophisticated 2D spatial-spectral mapping to obtain better throughput.

CHAPTER 4

MODELING OF A SPATIALLY INCOHERENT SOURCE USING THE MONTE-CARLO METHOD

The next step in this research is to combine the functionalities of interferometric and diffractive elements together and replace the bulky tandem Fabry-Perot etalon cylindrical beam volume hologram spectrometer with a more compact spectrometer designed based on three-dimensional (3D) photonic crystal (PC) structures as a new class of highly dispersive materials [22-24]. Prior to that, in order to efficiently analyze and optimize PC structures under diffuse light we need to develop a simulation tool to model a spatially incoherent source. Although analytic or semi-analytic techniques exist and work well for simpler structures like volume holograms [18, 19], the analysis of the propagation of diffuse light in more complicated structures like PCs requires detailed numerical simulation as no analytic representation of electromagnetic waves in such structures exists. Several numerical techniques have been widely used for the analysis of spatially coherent electromagnetic waves in PCs, among which the finite difference time-domain (FDTD) technique [71] has got considerably more attention. However, the conventional implementation of these techniques for diffuse sources is not efficient since all these techniques simulate field propagation due to a known (i.e., deterministic) source. Thus, in simulation with extended sources (i.e., sources different from the point source), the relative spatial incoherence of different source points is not conserved in conventional implementation. On the other hand, multiple simulations of large (practical length) structures with only one nonzero point source at a time and incoherent addition of the

results of all such simulations (i.e., brute-force method) is very time consuming despite being accurate. As a result, there is an urgent need for the development of efficient tools for the implementation of the spatially incoherent sources in the existing simulation methods like FDTD.

In this chapter we present a reasonably accurate and efficient technique based on the Monte-Carlo method for the numerical implementation of diffuse sources with at least one order of magnitude (and potentially several orders of magnitude) reduction in the simulation time compared to the brute-force implementation. The model developed in this chapter is quite general and can be implemented by any numerical simulation tool. However, due to extensive use of FDTD for the analysis of novel photonic structures, we use FDTD for its numerical implementation. We also use PC structures for validation of our model. Nevertheless, the model is not limited to PCs and can be applied to any other optical material [72].

In what follows we first summarize some key properties of spatially incoherent sources and then present the underlying principle for our proposed model. The model is then used to analyze PC structures, and the results are compared with those of the brute-force simulations. Finally, advantages and limitations of the proposed model will be discussed.

4.1. Fundamentals of Incoherent Source Modeling

Let $V(\mathbf{r},t)$ denote a field variable at a point represented by a position vector $\mathbf{r}$ at time t. This function may represent, for example, a Cartesian component of the electric field of an electromagnetic wave. We do not specify the nature of V more closely at this stage, since our main analysis is independent of any particular choice of the field polarization.

For any realistic light beam, V will be a fluctuating function of time and space, which may be regarded as a typical member of an ensemble consisting of all possible realization of the field.

As shown in Figure 4.1, assume that the fields at points $P_1(\mathbf{r}_1)$ and $P_2(\mathbf{r}_2)$ in the beam are isolated by placing an opaque screen A across the beam, with pinholes at the two points, and that we observe the intensity distribution resulting from the superposition of the light emerging from the two pinholes, on a screen B at a distance d from A. Assuming d is large compared to the wavelength, the instantaneous field at point P on the screen B is given by

$$V(\mathbf{r},t) = V(\mathbf{r}_1, t - t_1) + V(\mathbf{r}_2, t - t_2), \tag{4.1}$$

where t_1 and t_2 are the time delays from points P_1 and P_2 to point P, respectively.

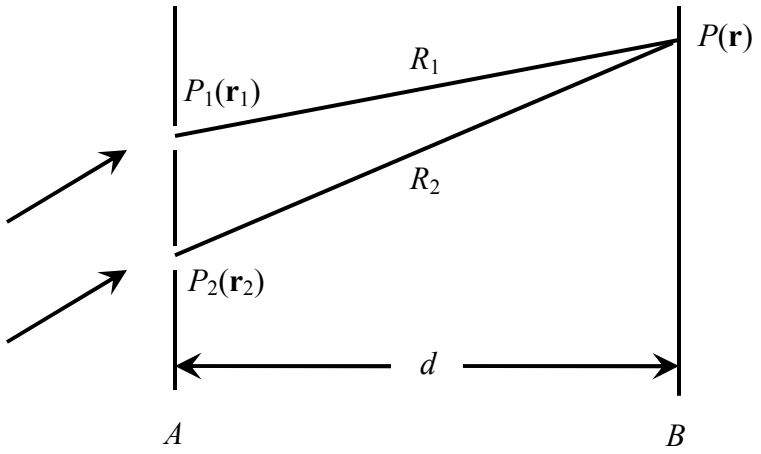

Figure 4.1. Interference experiment from which the mutual coherence function of a light beam is determined.

The ensemble average of intensity $\langle I(\mathbf{r},t)\rangle_e = \langle V^*(\mathbf{r},t)V(\mathbf{r},t)\rangle_e$, at the point P at time t is given by [73]

$$\langle I(\mathbf{r},t)\rangle_e = \langle I_1(\mathbf{r}_1, t - t_1)\rangle_e + \langle I_2(\mathbf{r}_2, t - t_2)\rangle_e + 2\,\mathrm{Re}\{\Gamma(\mathbf{r}_1, \mathbf{r}_2; t - t_1, t - t_2)\}, \tag{4.2}$$

where

$$\Gamma(\mathbf{r}_1,\mathbf{r}_2;t_1,t_2)=\langle V^*(\mathbf{r}_1,t_1)V(\mathbf{r}_2,t_2)\rangle_e, \tag{4.3}$$

$$\langle I(\mathbf{r}_j,t_j)\rangle_e=\langle V^*(\mathbf{r}_j,t_j)V(\mathbf{r}_j,t_j)\rangle_e, \quad (j=1,2). \tag{4.4}$$

The function $\Gamma(\mathbf{r}_1,\mathbf{r}_2;t_1,t_2)$ is recognized as the cross-correlation function of the random processes $V(\mathbf{r}_1,t)$ and $V(\mathbf{r}_2,t)$. It represents the correlation that exists between the field fluctuations at the pinholes P_1 and P_2, at times t_1 and t_2 respectively. It is known as the mutual coherence function in the classical theory of optical coherence [73]. The quantity $\langle I(\mathbf{r}_j,t_j)\rangle_e$ represents the ensemble average intensity of the light at the pinhole P_j at the time t_j $(j=1,2)$. For $\Gamma\neq 0$ in Equation (4.2), the superposition of the two beams will give rise to interference, which is a direct result of spatial coherence. The condition of $\Gamma=0$ is the mathematical definition of spatially incoherent light. We assume that the optical field is stationary, at least in the wide sense, and ergodic [73] so the mutual coherence function only depends on the time difference $\tau=t_1-t_2$ (i.e., $\Gamma(\mathbf{r}_1,\mathbf{r}_2,\tau)$).

As mentioned earlier the concept of coherence is buried in the mutual coherence function. Since the fluctuations in the light beam from any two different points of a spatially incoherent source are mutually incoherent and hence have no fixed phase relationship to each other, the power spectrum distribution at the output plane *B* is obtained by simple addition of beam power spectra due to contribution at each point in the input plane [73]. In a mathematical sense for an input source composed of k mutually incoherent point sources, the power spectrum at an observation point $\mathbf{r}$ in the output plane is given by

$$S(\mathbf{r},\nu)=S_1(\mathbf{r}_1,\nu)+S_2(\mathbf{r}_2,\nu)+\ldots+S_k(\mathbf{r}_k,\nu), \tag{4.5}$$

where ν and $S(\mathbf{r},\nu)$ correspond to temporal frequency and power spectrum (calculated by Fourier transform of $\Gamma(\mathbf{r},\mathbf{r},\tau)$), respectively [73]. Note that in Equation (4.5) no cross-correlation term is considered. Therefore one possible method to model a spatially incoherent source is to turn on one individual source at a time, find the power spectrum on the output plane *B*, and then add them together. Although this approach is accurate, it is not time-efficient since we need to repeat the simulation as many times as the number of sources. We refer to this approach as the brute-force method and the result of this method is taken as the reference for comparison with our approximate method.

To reduce the simulation time in our new approach we develop a statistical model of the spatially incoherent source in such a way that every two point sources in the input plane *A* are mutually independent. In this method, all the sources are on simultaneously during simulation and each source by itself consists of a pulse train. To incorporate the randomness in the source plane, we assume that each point source is composed of a train of identical pulses in time where the interval between the centers of each two pulses is defined by an independent exponential random variable. This source is referred to as a Poisson pulse train source throughout this chapter. The form of a single pulse is defined by

$$g(t) = e^{-(t/T)^2} \sin(\omega t) . \tag{4.6}$$

The reason for this definition is to cover a reasonable frequency bandwidth using one time domain simulation [71] with the FDTD technique. The center frequency ω and the bandwidth $\Delta\omega = 1/T$ are defined based on the desired frequency range for simulation. A typical Poisson pulse train source for an input plane composing of k individual point

sources (usually corresponding to the nodes in the FDTD simulation) is shown in Figure 4.2.

To prove that the proposed source is a reliable model for a spatially incoherent source, we need to calculate the mutual coherence function Γ between two arbitrary Poisson pulse trains shown in Figure 4.2. The pulse train at each point in the source plane can be modeled as

$$V(t) = \sum_{i=1}^{\infty} g(t - t_i) = y(t) * g(t), \tag{4.7}$$

where

$$y(t) = \sum_{i=1}^{\infty} \delta(t - t_i), \tag{4.8}$$

is the derivative of a Poisson process and the interval between t_i and t_{i+1} is an exponential random variable with parameter α [74], $g(t)$ is defined by Equation (4.6), $*$ denotes convolution, and $\delta(t)$ is the Dirac delta function. From Equation (4.7), we can calculate the time-averaged expectation value of $V(t)$ as

$$\begin{aligned} \langle V(t) \rangle_e &= \langle y(t) * g(t) \rangle_e = g(t) * \langle y(t) \rangle_e \\ &= g(t) * \alpha = \alpha \int_{-\infty}^{+\infty} e^{-(t/T)^2} \sin(\omega t) dt = 0, \end{aligned} \tag{4.9}$$

where the properties of the Poisson process are used to obtain the ensemble average of $y(t)$. Now by assuming independent exponential random variables for the intervals between any two pulses for each source point, we can calculate the mutual coherence function corresponding to point sources at $\mathbf{r}_m$ and $\mathbf{r}_n$ as

$$\begin{aligned} \Gamma(\mathbf{r}_m, \mathbf{r}_n; t_1, t_2) &= \langle V^*(\mathbf{r}_m, t_1) V(\mathbf{r}_n, t_2) \rangle_e \\ &= \langle V_m^*(t_1) \rangle_e \langle V_n^*(t_2) \rangle_e = 0, \end{aligned} \tag{4.10}$$

where the fist equality is valid since the random processes are independent and we have used Equation (4.9) to obtain the last result. Equation (4.10) clearly proves that assigning independent Poisson pulse trains to different source points truly models a spatially incoherent source in the input plane.

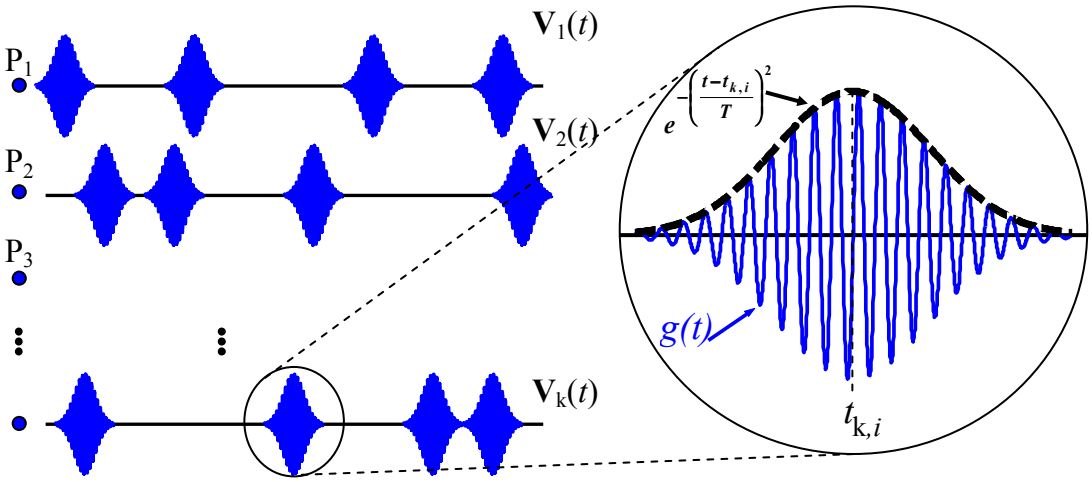

Figure 4.2. Schematic of the spatially incoherent Poisson pulse train source. For every source point the interval between the centers of Gaussian pulses, i.e., between $t_{k,i}$ and $t_{k,i+1}$, is an independent exponential random variable with parameter α.

4.2. Simulations and Results

The structure we consider here is a two-dimensional (2D) PC as shown in Figure 4.3(a). It is composed of square lattice of cylindrical air holes etched in GaAs ($\varepsilon_r = 12.96$). The ratio of holes radius to lattice constant (r/a) is equal to 0.3 that guarantees no bandgap [28] as we desire for diffuse source spectroscopic applications. In order to quantitatively compare the simulation time of the two models (i.e., brute-force and Poisson pulse train) we assume the size of the PC to be a $10a$ by $10a$ square area. We implement both spatially incoherent source models in time domain using standard FDTD method. The light beam is assumed to be TE polarized (where the electric field is parallel to the z-axis). We assume 24 FDTD grid points per lattice constant (a) for both simulations,

which results to 240 mutually incoherent point sources in the input plane *A*. Note that all these parameters for the PC geometry and for the simulation grid are chosen just to set an example and by no means affect the applicability or accuracy of our model.

In the brute-force simulation, one source is excited at a time with a sinusoidal modulated Gaussian pulse [with mathematical representation of Equation (4.6)] and it propagates all the way through the structure to get to the output plane *B*. The normalized center frequency of the pulse (ω) is 0.04 and its width ($\Delta\omega$) is 0.016. The normalized width of the Gaussian pulse (*T*) in the time domain is $1/\Delta\omega = 62.5$ which corresponds to 120 time steps in our FDTD simulation. In order to find the steady state field profile in the output plane we have to run the simulation for about 65000 time steps. This results in a total simulation time of 240×65000 time steps.

In the second simulation we use our new approach and excite all the 240 sources in the input plane *A* with Poisson pulse trains simultaneously. In order to closely simulate the spatially independent point sources, the number of pulses (*NP*) and the average time distance between any two pulses should be large enough. This guarantees no overlap between adjacent pulses in each pulse train. Furthermore, the randomness of the simulation results is averaged out when the number of pulses is large. Here, we choose *NP* = 100 pulses and the average time distance between adjacent pulses (i.e., $1/\alpha$) is 180 time steps. To get to the steady state at the output plane *B*, we run the simulation for $100 \times 180 + 65000 = 83000$ time steps. To further average the results for power spectrum, we repeat this simulation for a few times. The gain of simulation time in our model compared to the brute-force technique depends on the number of simulations needed for

achieving good accuracy. Note that the number of simulations in our model is considerably smaller than that for the brute-force method.

In order to calculate the power spectrum at the output plane, we save all the field values at the output plane at all times during each simulation. The power spectrum is then calculated using the Fourier transformation of the autocorrelation function (or it can be directly calculated using the Fourier transformation of the field values [73]). In the brute-force method, we calculate $S(\mathbf{r},\nu)$ for each input source individually and then add them to enforce spatial incoherence [according to Equation (4.5)]. In the Poisson pulse train method, we calculate $S(\mathbf{r},\nu)$ at all points in the output plane for each simulation as described. We then repeat the simulation and calculate the average value of $S(\mathbf{r},\nu)$ at each point by ensemble averaging the results of all simulations. Figure 4.3(b) shows the power spectrum at a typical point in the output plane *B* for the PC structure described earlier. The results of both the brute-force method and the Poisson pulse train method are shown together in this figure. Obviously there is a very good agreement between the results of the two methods. Here we have simulated the second approach for 10 times to find the ensemble average of the power spectrum. The gain (*G*) in simulation time (by using the Poisson pulse train model) is then equal to $G = \frac{240 \times 65000}{10 \times 83000} \cong 18.8$.

Therefore by using the Poisson pulse train source we can achieve close to 20 times faster simulation while keeping error at a reasonable value (as further discussed in the next section) compared to the brute-force simulation.

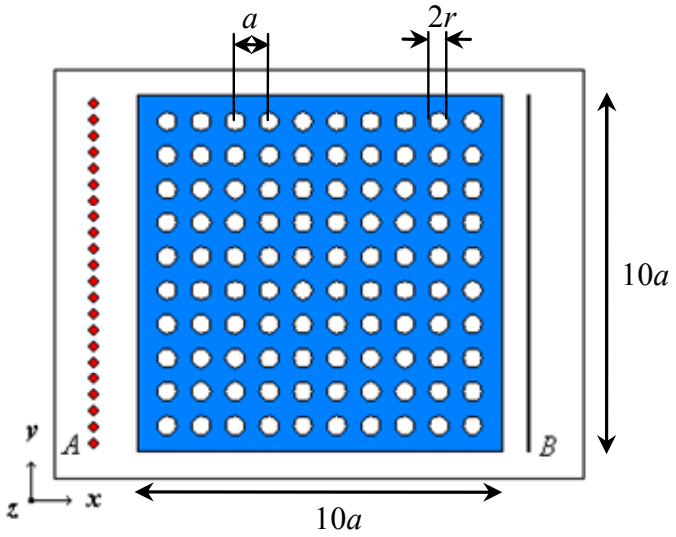

(a)

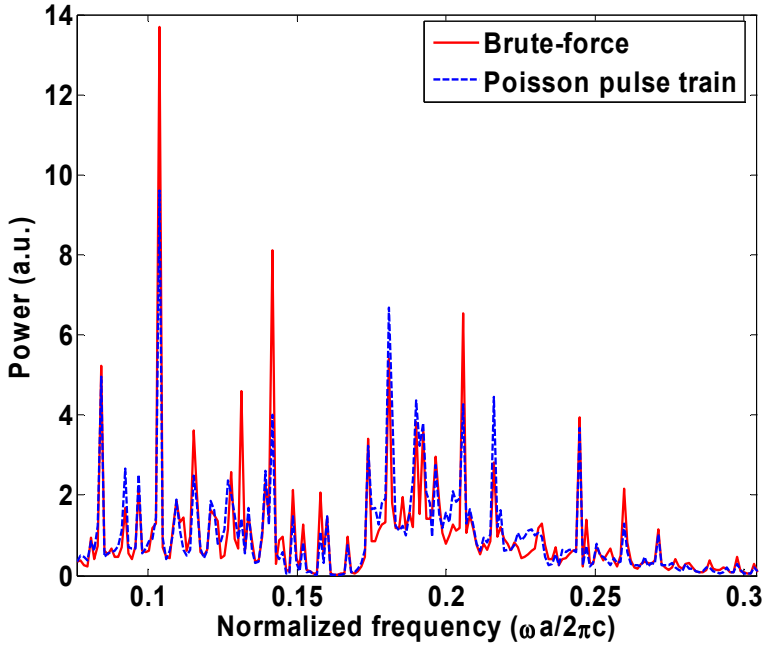

(b)

Figure 4.3. (a) The square lattice PC used for simulations. We have assigned 24 point sources per lattice constant in the input plane *A* to model the spatially incoherent source. Each source is excited with TE polarized light. For the whole time of the simulation all the field values are saved at the output plane *B*. (b) The power spectrum of the brute-force simulation as well as that of the Poisson pulse train simulation with ensemble averaging of 10 different simulations for the PC structure shown in (a) at a typical point in the output plane *B*. Both curves have been normalized to their mean values for comparison.

4.3. Comparison between the Monte-Carlo Model and the Brute-Force Model

The main trade-off for the proposed simulation method is the accuracy versus the gain of simulation time. To measure the error, we first calculate the sum of the square of the differences between the two power spectra (from the two methods) for all frequencies and all points at the output plane *B*. Then we divide this sum by the sum of the square of the power spectrum for all frequencies and all points at the output plane *B* calculated using the brute-force simulation. Note that we use all the frequencies and all the points on the output plane *B* to show the accuracy of our model. Figure 4.4 shows the error and the gain in simulation time verses the number of simulations for the Poisson pulse train method for the PC structure in Figure 4.3(a) using the same simulation parameters used for the calculations in the last section. As seen in Figure 4.4(a) by increasing the number of simulations for the Poisson pulse train method we get smaller error. However, increasing the number of simulations degrades the gain of simulation time as illustrated in Figure 4.4(b). As clearly seen from Figure 4.4 by accepting 10% error which is reasonable for most of practical applications, the simulation of the Poisson pulse train method is performed almost one order of magnitude faster than the brute-force simulation for the small PC structure in Figure 4.3(a).

Figure 4.4(a) implies that the amount of error can not be improved to less than 8% in limited number of simulations. A possible way to solve this issue is to increase the number of pulses at each source point in the proposed method. To do this, we have increased the number of pulses (*NP*) to 350 and accordingly the simulation time to 128000 time steps to get the steady state result. Figure 4.5(a) shows the amount of error can be decreased more than the previous result. The cost of achieving this better accuracy

is the longer simulation time and, therefore, a reduction in the gain of the simulation time as Figure 4.5(b) suggests.

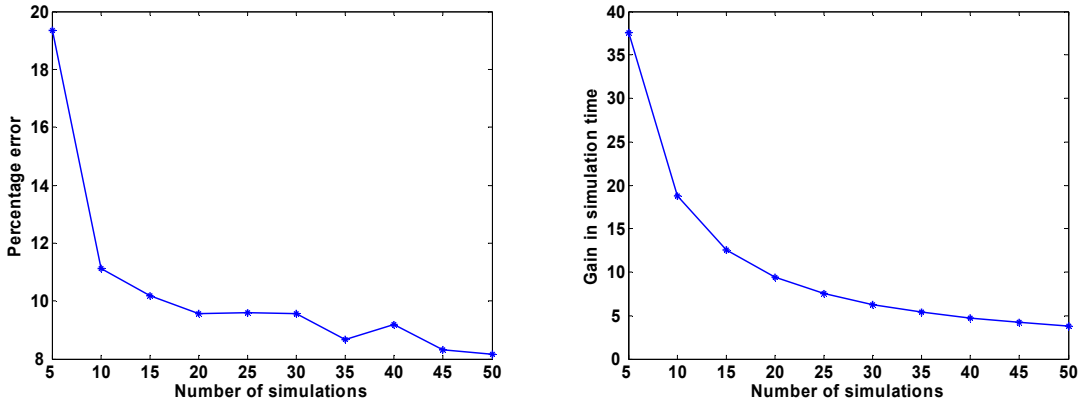

(a) (b)

Figure 4.4. (a) The relative error between the two methods as a function of the number of simulations, and (b) the gain in simulation time of the Poisson pulse train method compared to the brute-force simulation for $NP = 100$.

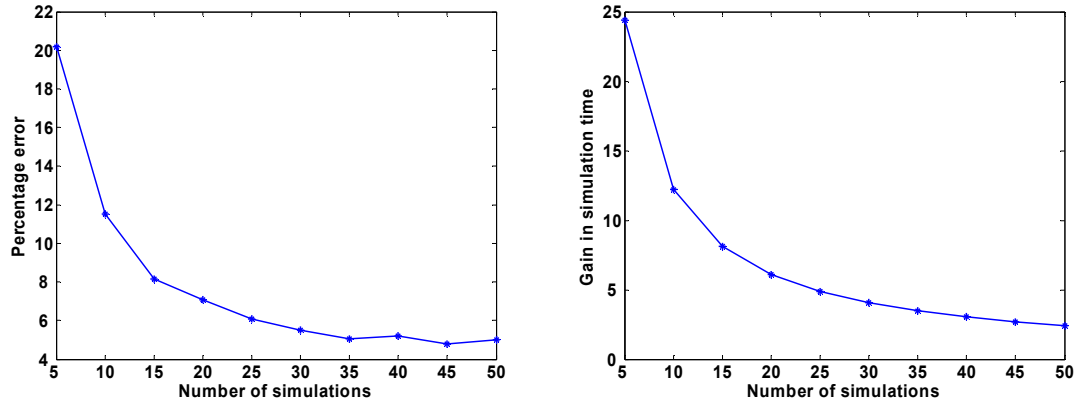

(a) (b)

Figure 4.5. (a) The relative error between the two methods as a function of the number of simulations, and (b) the gain in simulation time of the Poisson pulse train method compared to the brute-force simulation for $NP = 350$.

An important point is that we have used a very small PC structure for our simulation. In general, a PC device designed to operate as dispersive element has dimensions larger than $100a$ by $100a$ [43, 44]. The advantage of the Poisson pulse train method over the brute-force method becomes more evident for larger structures since the number of simulations needed in the brute-force method increases proportional to the size

of the structure and its growth rate is faster than that of the Poisson pulse train method. As a result, extensive gain in the simulation time of practical-size structures is expected for the proposed Poisson pulse train technique. It should be noted that the simulation of such large structures might not be practical using the brute-force method.

Figure 4.6 shows the error and gain in the simulation time for the same PC as that in Figure 4.3(a) when the size of the structure is increased to $20a$ by $10a$. All other parameters are the same as those used to obtain the results of Figure 4.4. Comparing Figures 4.6 and 4.4 clearly shows higher gain in the simulation time can be achieved for larger structures. For example, for obtaining a result with an error close to 8% the gain in the simulation time for the larger structure is more than twice of that for the smaller structure. Thus, for practical-size structures, we expect to have multiple orders of magnitude improvement in the simulation time (while keeping error small) by using the Poisson pulse train model for spatially incoherent sources.

It is noteworthy to mention while we have compared the Poisson pulse train method with the brute-force method to show its accuracy and efficiency, this method by itself can be used to choose the number of simulations needed to obtain accurate results in a typical simulation. For this purpose, we can increase the number of simulations one by one and calculate the relative error between the new power spectrum at the output plane and the previous one. Again, we calculated this error for all the points and all the frequencies as explained before. Based on this relative error, we can decide on the number of simulations needed for the desired accuracy and stop simulating the structure after certain number of times. Figure 4.7 shows the relative error between consecutive results versus the number of simulations for the structure shown in Figure 4.3(a) using

the Poisson pulse train method with NP = 100. All the other parameters are similar to those used to obtain the results shown in Figure 4.4 for the Poisson pulse train method. To obtain the results, we increased the number of simulations by five in each step and calculated the relative error. It is clear from the Figure 4.7 that by increasing the number of simulations the relative error decreases and, therefore, the results converge. This is expected since the increase in the number of simulations provides more accurate estimation of the ensemble average of the results. Using the relative error we can choose the number of simulations for achieving desired accuracy.

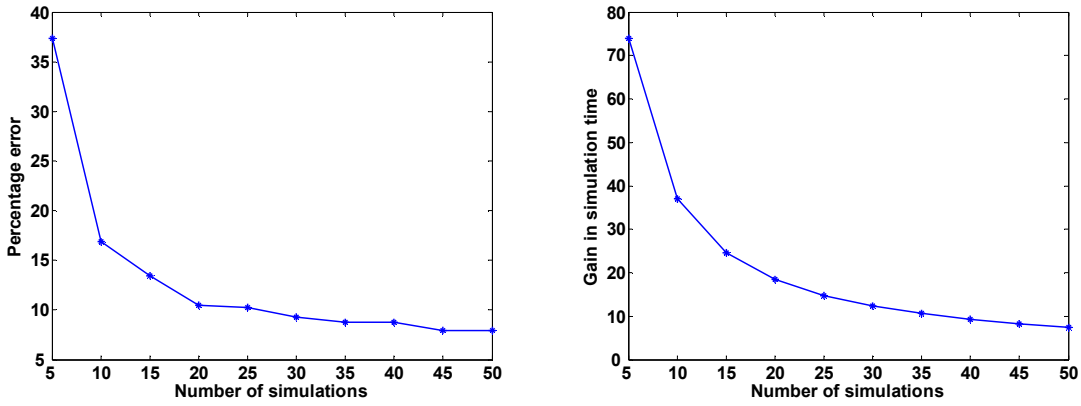

(a) (b)

Figure 4.6. (a) The relative error between the two methods as a function of the number of simulations, and (b) the gain in simulation time of the Poisson pulse train method compared to the brute-force simulation for NP = 100. The size of the PC used for simulations is 20a by 10a with the same parameters as in Figure 4.3(a).

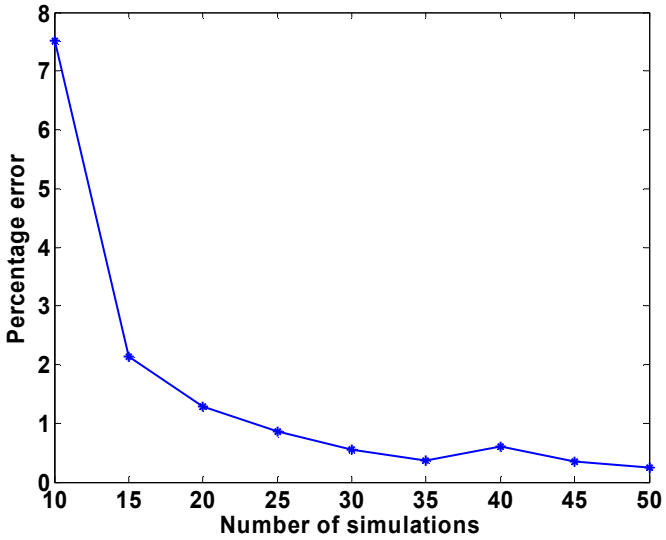

Figure 4.7. The relative error between consecutive results of the Poisson pulse train method with NP = 100 versus the number of simulations for the structure shown in Figure 4.3(a). We have increased the number of simulations by five in each step.

Finally, it is useful to note the spatial-spectral diversity in the output power spectrum for the PC structure under a uniform diffuse light input. While the focus of this chapter is only the development of an accurate and efficient incoherent source, it is worth mentioning that the results [Figure 4.3(b)] clearly show the potential of PC structures for spectroscopy.

.

CHAPTER 5

MODELING OF A SPATIALLY INCOHERENT SOURCE USING THE WIENER CHAOS EXPANSION METHOD

Although the Monte-Carlo method explained in the previous chapter reduces the simulation time of the spatially incoherent source with respect to the brute-force method, its accuracy is not very promising. In this chapter we report on a new model which almost matches the results of the brute-force model while considerably reduces the simulation time. To explain our new model, let's revisit the propagation of the spatially incoherent source from the beginning.

We know that the light beam originated from a spatially incoherent source is inherently an electromagnetic wave which can not be modeled by a deterministic field. To physically model such a spatially incoherent source, we normally use stochastic processes [73-75]. Therefore, the resultant deriving equation will be a stochastic partial differential equation (PDE) in the form of the well-known electromagnetic wave equation. Unlike deterministic PDEs, solutions of stochastic PDEs are random fields. However, in most cases the physical evaluation is based on the statistical moments (e.g., mean, variance) of the solutions rather than the solutions themselves. Therefore, it is highly desired to be able to calculate these statistical moments independent of finding the random solutions.

The governing stochastic electromagnetic wave equation is usually too complex to be solved analytically; therefore numerical simulations play a significant role in solving this useful class of PDEs. So far, the most commonly used method in simulation

of random effects modeled by a stochastic PDE is the Monte-Carlo method. As explained in the previous chapter, it solves the stochastic PDE realization by realization and then takes statistical moments from all the realizations [72]. However, it has some major limitations. For instance, in order to correctly simulate a random effect, many realizations have to be computed to obtain a reliable estimate of various statistical properties. Moreover, in the Monte-Carlo method we need a random number generator that naturally increases the numerical error and consequently degrades the accuracy of the solution. Hence, the Monte-Carlo simulations are generally lengthy and inaccurate.

In this chapter we propose to use a more efficient and accurate approach based on the Wiener chaos expansion (WCE) method which has been widely used for many different problems for both analytical and numerical purposes [76-85]. In this method, both the spatially incoherent source and the random solutions of the wave equation are expanded on independent standard Gaussian random variables [86, 87]. The WCE separates the deterministic effects from the randomness in the stochastic PDE. Consequently, it results into a system of deterministic PDEs for the expansion coefficients, which is referred to as its propagator. The propagator is the mechanism responsible for the evolution of randomness inherent to the original stochastic PDE. Remarkably, the propagator has the same form as the original equation. The main statistics (such as mean, covariance, and higher-order statistical moments) can be calculated by simple formulas involving only the coefficients of the propagator [85]. In the WCE approach, there is no randomness directly involved in the computations. One does not have to rely upon random number generators, and there is no need to solve the

stochastic PDEs repeatedly over many realizations. Instead, the propagator system is solved only once.

Since the propagator is a set of deterministic PDEs for the WCE coefficients, standard deterministic numerical methods can be applied to solve it. Here, once again we have used the finite-difference time domain (FDTD) technique to numerically simulate the electromagnetic wave equation [71]. Further we have compared the results obtained using the WCE method to the results of the brute-force method which is a direct simulation method based on the exact definition of a spatially incoherent source [73]. It will be shown that the WCE method very accurately resembles the results of the brute-force method in a much faster pace. We have also used a photonic crystal (PC) structure which is a typical inhomogeneous optical material for validation of our numerical simulation. Nevertheless, the model is not limited to PCs and can be applied to any other optical material [86, 87].

In what follows we first briefly introduce the WCE method and some of its significant properties. Then we apply the WCE method to the electromagnetic wave equation (i.e., Helmholtz wave equation) driven by a spatially incoherent source and we form out its associated propagator. The propagator is then numerically solved by a standard FDTD technique for a typical PC structure as a propagation environment, and the results are compared to those of the brute-force simulations. Finally, advantages and limitations of the proposed method will be discussed.

5.1. Wiener Chaos Expansion

As mentioned earlier, WCE has been extensively used for solving stochastic PDEs in many different fields. Here we briefly introduce the expansion and emphasize some of its useful properties for linear equations. Let *u* be a solution of a linear stochastic PDE

$$L(u) = \sigma \dot{W}(x,t), \tag{5.1}$$

where L is a linear differential operator and $W(x,t)$ is a spatial-temporal Brownian motion. u is a function of x, t, and the Brownian motion. It would be beneficial if one could solve this equation by separating the deterministic spatial-temporal variables x and t from the random variable $W(x,t)$. At the beginning, this idea might appear to be improbable or at least impractical due to the infinite dimensional nature of the Brownian motion $W(x,t)$. Nevertheless, the information contained in the path of a Brownian motion can be efficiently quantized.

To be more specific, let's take a temporal Brownian motion $W(t)$ as an example. For any orthonormal basis $\{m_i(s), i = 1,2,...\}$ in $L^2([0,t])$, define

$$\xi_i = \int_0^t m_i(s)dW(s), \quad i = 1,2,.... \tag{5.2}$$

It is easy to show that ξ_i are independent standard Gaussian [$N(0,1)$] random variables. Then we have the following expansion

$$W(s) = \int_0^t \chi_{[0,s]}(\tau)dW(\tau) = \sum_{i=1}^{\infty} \xi_i \int_0^s m_i(\tau)d\tau \tag{5.3}$$

for all $s \le t$, where $\chi_{[0,s]}(\tau)$ is the characteristic function of interval $[0,s]$. The expansion in Equation (5.3) converges in the mean square sense

$$E\left[W(s)-\sum_{i=1}^{N}\xi_i\int_0^s m_i(\tau)d\tau\right]^2\to 0 \quad \text{as} \quad N\to\infty .$$

For many choices of basis functions (e.g., Haar wavelets or trigonometric functions) the convergence in Equation (5.3) holds with probability 1 and uniformly for $s\le t$. For the choice of sinusoidal basis functions that later will be used in this chapter,

$$\begin{cases} m_1(s)=\dfrac{1}{\sqrt{t}}, \\ m_i(s)=\sqrt{\dfrac{2}{t}}\cos\left((i-1)\pi\dfrac{s}{t}\right), \quad i=2,3,..., \end{cases} \tag{5.4}$$

one can easily show that

$$\begin{aligned} E\left[W(s)-\sum_{i=1}^{N}\xi_i\int_0^s m_i(\tau)d\tau\right]^2 &= E\left[\sum_{i=N+1}^{\infty}\xi_i\int_0^s m_i(\tau)d\tau\right]^2 \\ &= \sum_{i=N+1}^{\infty}\left(\int_0^s m_i(\tau)d\tau\right)^2 \\ &\le C\frac{1}{N}, \end{aligned} \tag{5.5}$$

where C is a constant independent of N.

In the same way, one can derive a similar expression for $W(x)$ if a spatial Brownian motion is considered and a simple tensor product can lead to the expression for a spatial-temporal Brownian motion,

$$W(x,t)=\sum_i \xi_i\int_0^x\int_0^t m_i(l,s)dlds , \tag{5.6}$$

where $\{m_i(l,s), i=1,2,...\}$ form an orthonormal basis of $L^2([0,x]\times[0,t])$. Replacing $W(x,t)$ in Equation (5.1) by Equation (5.6), we have

$$L(u)=\sigma\sum_i \xi_i m_i(x,t) . \tag{5.7}$$

This indicates that the solution u is a function of x and t as well as random variables ξ_i.

Using the fact that ξ_i are independent and L is a linear operator, we multiply Equation (5.7) by ξ_i and take the expectation, we obtain

$$L(u_i) = \sigma m_i(x,t) \tag{5.8}$$

where $u_i = E(u, \xi_i)$, and

$$u = \sum_i u_i \xi_i \,. \tag{5.9}$$

The Equation (5.8) is the associated propagator of the primary stochastic PDE given in Equation (5.1). Clearly, it has the same form as of the stochastic PDE while it is absolutely deterministic. This is the most significant observation which tells us that we can successfully factor out the random effects from the stochastic PDE. The expansion in Equation (5.9) is the Wiener chaos expansion (WCE) of *u* for linear equations.

In the following section we will apply the WCE method to the Helmholtz wave equation excited by a spatially incoherent source.

5.2. The WCE Method and the Stochastic Helmholtz Wave Equation

Although there are numerous reports on the physical properties of an incoherent beam in the context of optical coherence theory [73], to the best of our knowledge there is no explicit report on the direct simulation of its propagation in a typical environment. In this section, we first propose a new stochastic model for spatially incoherent light sources which drives the electromagnetic wave equation and then apply the WCE method to solve it rigorously.

Figure 5.1 shows our simulation platform, which is composed of an inhomogeneous dielectric material as the propagation environment. The source line is placed in front of the propagation medium along line *A* and the electric field values are

monitored along the output line *B*. All the input sources are excited with a TE polarization (where the electric field is parallel to the *z*-axis). Due to the *z*-invariant setup, the electromagnetic wave propagation throughout the medium can be reduced to a two-dimensional (2D) Helmholtz wave equation

$$\nabla^2 E_z(x,y,t) - \mu\varepsilon(x,y)\frac{\partial^2 E_z(x,y,t)}{\partial t^2} = \mu\frac{\partial J_z(x,y,t)}{\partial t}, \tag{5.10}$$

where the current density (J_z) is the source of excitation, and μ and $\varepsilon(x, y)$ are permeability and permittivity of the propagation environment, respectively. Here our source is represented by a one-dimensional (1D) array of point sources along line *A*. For modeling of a spatially incoherent source, any two point sources on line *A* should radiate independently of each other. More specifically, a spatially incoherent source is defined as $\left\langle J_z^*(y_i,t)J_z(y_j,t)\right\rangle = \delta(y_i - y_j,t)$. This definition by itself can be used as the brute-force method for numerical modeling of the spatially incoherent source. In the brute-force modeling, we enforce zero correlation between the contributions from every two input point sources by separately analyzing the structure with each point source and adding the individual contributions at the output line *B* incoherently (i.e., in power) [72].

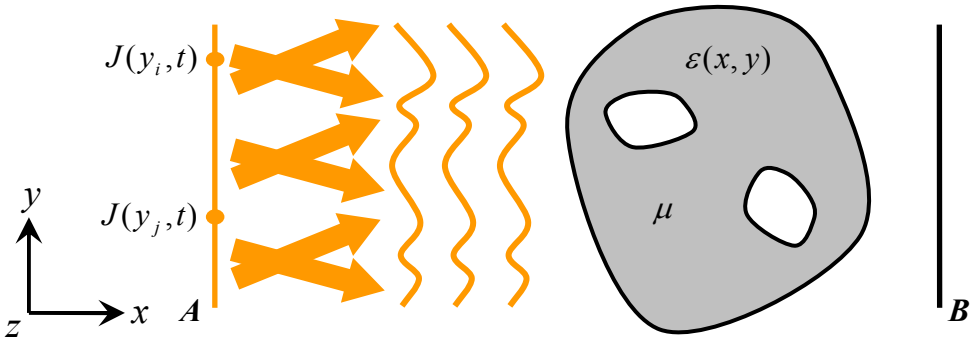

Figure 5.1. Propagation of a spatially incoherent source from the input source line *A* to the output line *B* in a typical environment is schematically shown.

Note that the input source along line A in Figure 5.1 is a deterministic function of time and its stochastic nature is only in the spatial dimension (i.e., y in Figure 5.1). To model the spatially incoherent source, we use the white noise, i.e., the derivative of the Brownian motion, to model the spatial part of the current density (J_z). More precisely, we represent the spatially incoherent source along line A (i.e., $x = x_A$) as

$$J_z(y,t) = dW(y)V(t), \tag{5.11}$$

where $V(t)$ is a deterministic function representing the time variation of the source and $dW(y)$ is the derivative of the Brownian motion representing the independent spatial randomness along y. Note that assuming J_z to be a separable function of space (y) and time (t) is consistent with all practical applications in which the time-variation of the source is assigned by the frequency range of operation and is usually the same at all points along the source line.

Following the formulation developed in the previous section, by choosing any orthonormal basis functions [$m_i(s)$] in $L^2([0,y])$, we can expand $dW(y)$ as

$$dW(y) = \sum_i \xi_i m_i(y), \tag{5.12}$$

where $\xi_i = \int_0^y m_i(s)dW(s) \quad i = 1,2,....$ Now both the input source (J_z) and the electric field (E_z) are expanded using the WCE method similar to Equation (5.9) as

$$J_z(y,t) = \sum_i \xi_i m_i(y)V(t), \tag{5.13}$$

$$E_z(x,y,t) = \sum_i \xi_i E_{zi}(x,y,t). \tag{5.14}$$

The expansion in Equation (5.14) separates the deterministic effects [$E_{zi}(x,y,t)$] from the randomness (covered by ξ_i). By placing Equations (5.13) and (5.14) into Equation

(5.10), the original stochastic Helmholtz wave equation is reduced to its propagator which is an associated set of decoupled deterministic equations for the expansion coefficients [$E_{zi}(x,y,t)$] as following,

$$\nabla^2 E_{zi}(x,y,t) - \mu\varepsilon(x,y)\frac{\partial^2 E_{zi}(x,y,t)}{\partial t^2} = \mu m_i(y)\frac{dV(t)}{dt} \qquad i = 1,2,.... \tag{5.15}$$

We summarize this observation into the following theorem:

Theorem 5.1. *The solutions of the Helmholtz wave equation (5.10) excited by a spatially incoherent source must be Gaussian distributed and have the following expression,*

$$u\big(x,y,t,W(y)\big) = \sum_i u_i^m(x,y,t)\xi_i \,, \tag{5.16}$$

where $u_i^m(x,y,t)$ *are deterministic coefficients and* ξ_i *are independent standard Gaussian random variables constructed as* $\xi_i = \int_0^y m_i(s)dW(s) \quad i = 1,2,....$

It is worth-mentioning that the linearity of the primary PDE in Equation (5.10) makes the application of the WCE method much easier than its application for nonlinear PDEs. It can be shown that all the statistical moments of the random solution of the original stochastic PDE at the output line *B* in Figure 5.1 can be directly calculated using these expansion coefficients [85]. Obviously, by choosing the number of expansion coefficients considered in Equation (5.12), the accuracy and the length of the simulation time can be varied. Fortunately, it is known that WCE is a very fast converging expansion technique, and usually does not require many expansion coefficients [76, 77, 79, 81, 82, 84]. Thus by using only a few terms in Equation (5.12), we can achieve enough accuracy in a very fast simulation for almost all practical optical structures.

5.3. Numerical Simulation of Spatially Incoherent Sources

The structure we consider here is a 2D PC as shown in Figure 5.2. It is composed of square lattice of cylindrical air holes etched in silicon. The radius of the air holes is 0.3a, where a is the lattice constant (i.e., period). We fix the size of the PC structure with dimensions $x_f = 10a$ and $y_f = 20a$. For the wave propagation simulation, we use the standard FDTD method. The x-y plane is discretized so we get 24 grid cells per lattice constant (a) along both x and y axes. The source line A is placed in the air one lattice constant (i.e., 24 grid cells) before the interface of the PC structure, and the output line B is fixed 3 grid cells after the interface of the PC structure in the air. To minimize the non-physical reflections from the computation boundary, a 12 grid-cell wide perfectly matched layer (PML) [71] is set up around the structure. Note that all these parameters for the PC geometry and for the simulation grid are chosen just to set an example and by no means affect the applicability or accuracy of our model.

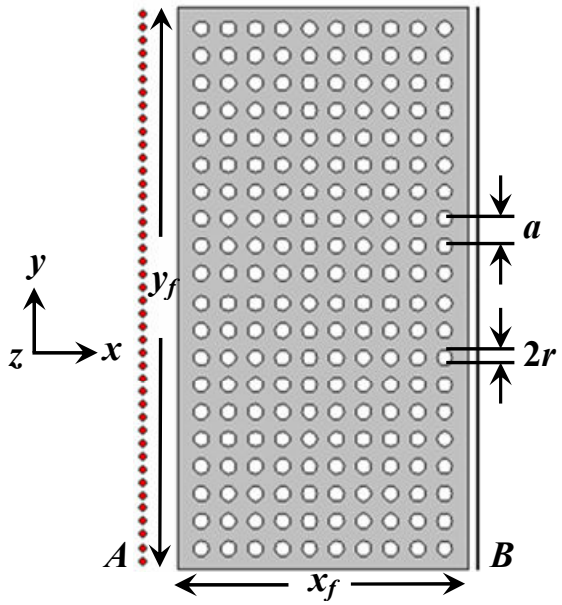

Figure 5.2. The schematic of a 2D square lattice PC structure of air holes in silicon with hole radius r and lattice constant a. The input (or source) and output lines are shown by A and B, respectively.

5.3.1. The Brute-Force Model

As we have already mentioned, one possible method to model a spatially incoherent source is to turn on one individual source on the input line *A* at a time, find the power spectrum on the output line *B*, and then add them together. While this technique models the incoherent source perfectly, it is very time-consuming since it requires one simulation of the entire structure for each input point source along line *A* in Figure 5.2. Knowing that even a single numerical simulation of a PC structure with dimension suitable for practical applications is very time-consuming, the use of the brute-force method is not a reasonable option. We use this method only as a reference to assess the accuracy of our more efficient WCE method.

In the brute-force simulation, one source is excited at a time with a commonly-used sinusoidal modulated Gaussian pulse for the time function $V(t)$ [71],

$$V(t) = \sin\left(\omega(t - t_0)\right)\exp\left(-\left(\frac{t - t_0}{T}\right)^2\right), \tag{5.17}$$

to cover a reasonable range of frequencies. This pulse propagates all the way through the structure to get to the output line *B*. The normalized center frequency of the pulse (ω) is 0.04 and its width ($\Delta\omega$) is 0.016. The normalized width of the Gaussian pulse (*T*) in the time domain is $1/\Delta\omega = 62.5$ which corresponds to 120 time steps in our FDTD simulation. In order to find the steady state field profile at the output line *B*, we have to run the simulation for about 65000 time steps. Since we have assigned one point source to each grid cell along input line *A*, it adds up to 20 × 24 = 480 point sources (corresponding to $y_f = 20a$ and 24 grid cells per lattice constant, *a*) and this results to the total simulation time of 480 × 65000 time steps.

5.3.2. The WCE Model

Using the formulation described in the last section, we need to solve the set of deterministic PDEs given in Equation (5.15) for the expansion coefficients [$E_{zi}(x,y,t)$]. In this section, we numerically solve these deterministic PDEs using the FDTD technique. Since the deterministic time function [i.e., $V(t)$] and the stochastic spatial function [i.e., $dW(y)$] of the source are separated as shown in Equation (5.11), for the numerical simulation of the WCE method once again we can use the sinusoidal modulated Gaussian pulse given in Equation (5.17) for the time function. However, for the spatial part we choose a set of sinusoidal basis functions for $m_i(y)$ as given in Equation (5.4). It is worth mentioning that in general we can choose any orthonormal basis for the spatial function [$dW(y)$ in Equation (5.12)]. The functions used here are primarily selected for their simplicity.

In the numerical simulation, we need to simulate the structure for each basis function $m_i(y)$ (i = 1, 2, ..., M) to find the corresponding $E_{zi}(x,y,t)$ defined in Equation (5.15) at the output line B (i.e., $x = x_B$). In each simulation all the point sources along line A are excited simultaneously, however the amplitude of the time function at each point source is modulated with the value of $m_i(y)$ at its corresponding vertical position. We can then calculate all statistical properties of the output field using its corresponding expansion coefficients. For example, prior to calculate the power spectrum of light at the output line B, we need to find the second moment [73] of the random field values in the frequency domain [i.e., $\langle E_z{}^2(x,y,\omega)\rangle_e$] from Equation (5.10) which can be simply

calculated using the Fourier transform of its corresponding expansion coefficients [$E_{zi}(x, y, \omega)$] as

$$\langle E_z{}^2(x, y, \omega)\rangle_e = \sum_i \left|E_{zi}(x, y, \omega)\right|^2 . \tag{5.18}$$

It should be noted that the Fourier transform is a linear transformation and thus, all the formulation for the statistical moments in the time domain is kept unchanged in the frequency domain. The key advantage of the WCE method is its fast convergence. With M expansion coefficients selected in Equation (5.15), the total simulation time is M times the simulation time of the original structure with a deterministic input (i.e., $M \times 65000$ time steps).

5.4. Simulation Results and Discussion

The simulation result of the electric field power spectrum versus the normalized frequency at a typical point on the output line B is shown in Figure 5.3. For this simulation, we have only used $M = 15$ expansion coefficients. The same data calculated using the brute-force technique is also shown in Figure 5.3 for comparison. The excellent agreement between the fast simulation using the WCE model and the long simulation using the brute-force model is clear from Figure 5.3. To calculate the gain in the simulation time using the WCE model, we have just to compare the total number of simulations of the entire structure needed in the two models. This number is equal to $M = 15$ (i.e., the number of the expansion coefficients) for the WCE model while it is equal to the number of FDTD grid cells along the source line A, which is 480 for the brute-force model. Thus, the simulation based on the WCE model is 32 times faster than that using the brute-force model.

Figure 5.4(a) shows the relative error of the WCE model with respect to the brute-force model as a function of the number of expansion coefficients, *M*. To calculate the relative error, we first calculate the sum of the square of the differences between the two power spectra (from the two models) for all frequencies and all points at the output line *B*. Then, we divide this sum by the sum of the square of the power spectrum for all frequencies and all points at the output line *B* calculated using the brute-force model. The exact mathematical formulation for the relative error is as following:

$$Error = \frac{\sum_{i}^{N_p}\sum_{j}^{N_f}\left(\left\langle E_{zBF}^2(x_B, y_i, \omega_j)\right\rangle_e - \left\langle E_{zWCE}^2(x_B, y_i, \omega_j)\right\rangle_e\right)}{\sum_{i}^{N_p}\sum_{j}^{N_f}\left\langle E_{zBF}^2(x_B, y_i, \omega_j)\right\rangle_e}$$

where N_p and N_f are the number of grid cells on the output line *B* and the number of discrete frequencies in our numerical simulation, respectively. Note that we use all the frequencies and all the points at the output line *B* to show the accuracy of our model. Figure 5.4(a) clearly shows that the results of the WCE model very quickly become close to those of the brute-force model with negligible error (the error is 0.08% for $M = 15$), which is a direct observation of its fast convergence.

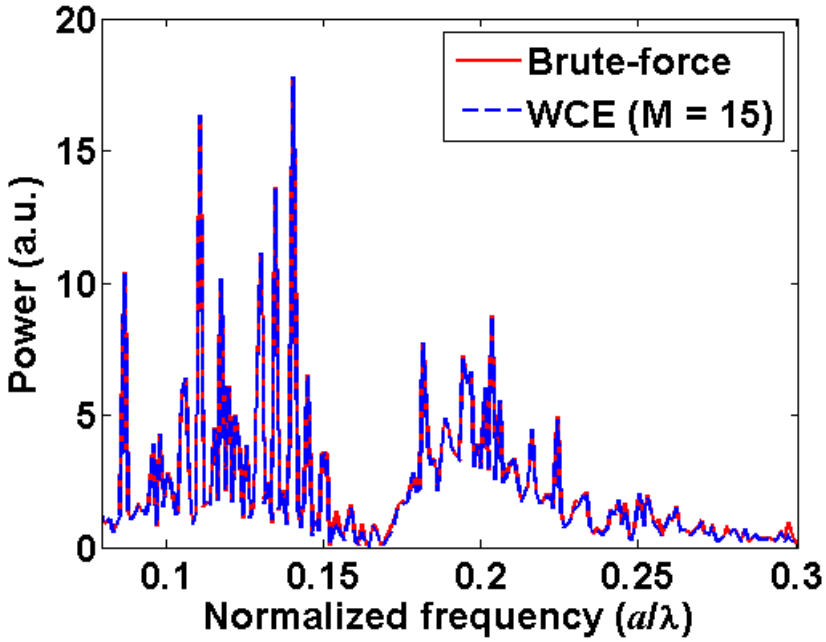

Figure 5.3. The electric field power spectrum as a function of normalized frequency at a typical point on the output line *B* in Figure 5.2 is shown. The simulation result of WCE model was obtained with only $M = 15$ expansion coefficients.

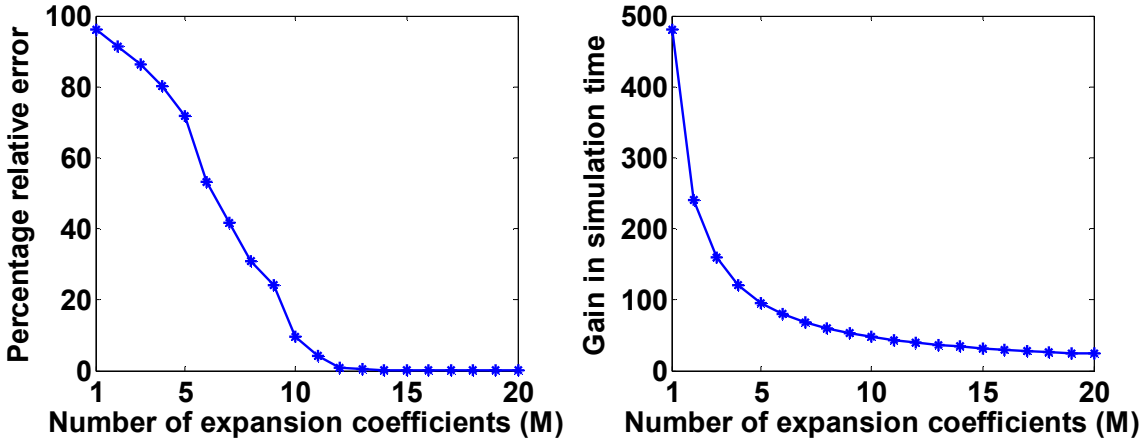

(a) (b)

Figure 5.4. (a) The relative error and (b) the gain in the simulation time of the WCE model with respect to the brute-force model as a function of the number of expansion coefficients (*M*).

Figure 5.4(b) shows the simulation time advantage of the WCE model with respect to the brute-force model. As seen in this figure, for larger *M* values the gain in the simulation time of the WCE model over the brute force model is decreased. This is because by increasing *M*, the number of distinct PDEs in Equation (5.15) and equally the

number of FDTD simulations for WCE model is increased. Therefore, the overall WCE simulation takes longer. Table 5.1 shows the number of expansion coefficients M required in WCE model for assuring certain upper-bounds of the relative error. Correspondingly, the gain in simulation time has been calculated and given inside the table. As implied by the table, for an accuracy better than 99%, we have to truncate the WCE series in Equation (5.12) at M = 12 and hence the numerical simulation is performed almost 40 time faster than the brute-force model. Moreover, the data in Table 5.1 clearly verifies the fast convergence behavior of the WCE model. Comparing the first and the third columns tells us by inclusion of only five more expansion coefficients in the WCE model, the error is 100 times reduced.

Table 5.1. Number of expansion coefficients (M) versus gain for a specific amount of relative error

Error	$<10\%$	$<1\%$	$<0.1\%$
M	10	12	15
Gain	48	40	32

5.5. Relation between the Brute-Force Model and the WCE Model

As the last comment in this section, we will show that there is a mathematical relation between the brute-force model and the WCE model.

Let $n_j(s)$ be another orthonormal basis for $L^2([0,y])$ too, similar to the discussion given at the beginning, we can construct $\eta_j = \int_0^y n_j(s)dW(s)$, and then the solutions $u(x,y,t,W(y))$ have a different expression

$$u(x,y,t,W(y)) = \sum_j u_j^n(x,y,t)\eta_j \,, \tag{5.19}$$

where $u_j^n(x,y,t)$ satisfies Equation (5.15) with $m_i(y)$ being replaced by $n_j(y)$.

Theorem 5.2. *The coefficients u_i^m and u_j^n satisfy the following equation*

$$u_j^n = \sum_i < m_i, n_j > u_i^m , \tag{5.20}$$

where $< m_i, n_j >= \int_0^y m_i(s) n_j(s) ds$.

Proof: Since both $m_i(s)$ and $n_j(s)$ are orthonormal bases of $L^2([0,y])$, we must have

$$m_i(s) = \sum_j < m_i, n_j > n_j(s).$$

Therefore, if we integrate both sides against $dW(s)$ over $[0,y]$, we have

$$\begin{aligned} \xi_i = \int_0^y m_i(s) dW(s) &= \int_0^y \sum_j < m_i, n_j > n_j(s) dW(s) \\ &= \sum_j < m_i, n_j > \int_0^y n_j(s) dW(s) = \sum_j < m_i, n_j > \eta_j . \end{aligned}$$

Then by using Equation (5.19) to expand the solution *u* on these two bases, we have

$$\sum_j u_j^n \eta_j = \sum_i u_i^m \xi_i = \sum_i u_i^m \sum_j < m_i, n_j > \eta_j = \sum_j \left(\sum_i < m_i, n_j > u_i^m \right) \eta_j ,$$

which implies Equation (5.20).

Theorem 5.3. *The brute-force solutions u_j^p and the WCE solutions u_i^m are related by the following formulas,*

$$u_j^p = \sum_i m_i(y_j) u_i^m , \tag{5.21}$$

and conversely

$$u_i^m = \sum_j m_i(y_j) u_j^p . \tag{5.22}$$

Proof: First of all, we note that in the brute-force method if the point source at y_j is excited then $J_z(x_A, y, t) = \delta_j(y)V(t)$ is the input source for Equation (5.10) where

$$\delta_j(y) = \begin{cases} 1 & \text{if } y = y_j \\ 0 & \text{otherwise} \end{cases}.$$

We define

$$n_j^h(y) = \begin{cases} \dfrac{1}{\sqrt{h}} & y \in \left[y_j - \dfrac{h}{2}, y_j + \dfrac{h}{2} \right], \quad j = 1, ..., N, \\ 0 & \text{elsewhere} \end{cases}$$

where $h = y_f / N$. Denote u_j^h as the solutions of Equation (5.15) with $n_j^h(y)\sqrt{h}V(t)$ as the input which satisfies $\lim_{h\to 0} n_j^h(y)\sqrt{h}V(t) = \delta(y_j)V(t)$. We have

$$\lim_{h\to 0} u_j^h = u_j^p.$$

Follow the linearity of Equation (3.6), it is easy to check u_j^h can be expressed as

$$u_j^h = \sum_i < n_j^h, m_i > u_i^m .$$

Taking *h* to 0, we obtain Equation (5.21).

On the other hand, the piecewise constant functions u_j^h span a subspace of $L^2([0, y])$ as

$$R_h = span\left\{ n_j^h(y), j = 1, ..., N \right\}.$$

It is obvious that

$$\lim_{h\to 0} R_h = L^2([0, y]),$$

which implies,

$$m_i(y) = \lim_{h\to 0}\sum_j < m_i, n_j^h > n_j^h(y)$$
$$= \lim_{h\to 0}\sum_j \frac{1}{\sqrt{h}} m_i(y_j) h n_j^h(y).$$

Follow the linearity of Equation (5.15) again, we have

$$u_i^m = \lim_{h\to 0}\sum_j < m_i, n_j^h > u_j^h$$
$$= \lim_{h\to 0}\sum_j \sqrt{h} n_j^h(y) m_i(y_j) u_j^h$$
$$= \sum_j m_i(y_j) u_j^p,$$

which is Equation (5.22).

As mentioned earlier in particular we are interested in the second moment of the solutions in many applications and it can be computed by the WCE coefficients as following:

Corollary: *Let u_j^p be the brute-force solutions with a point source at y_j. Let u_i^m be the solutions of Equation (5.15) with $J_z(x_A, y, t) = m_i(y)V(t)$ as the input source. Then the second moment of the solutions is preserved,*

$$\sum_j \left|u_j^p\right|^2 = \sum_i \left|u_i^m\right|^2. \tag{5.23}$$

Proof: From Equation (5.21) and the orthonormal property of $m_i(y)$, one has

$$\sum_j \left|u_j^p\right|^2 = \sum_j \left(\sum_{i,k} m_i(y_j) m_k(y_j) u_i^m u_k^m \right)$$
$$= \sum_{i,k} \left(\sum_j m_i(y_j) m_k(y_j) \right) u_i^m u_k^m$$
$$= \sum_i \left|u_i^m\right|^2.$$

This result confirms the equivalence of the second moments of the brute-force model and the WCE model as shown in Figure 5.3. Note that in general this is not true for other statistical moments. Thus, for correct comparison between their other moments, one has to use the linear transformations given in Theorem 5.3 to find the corresponding relation.

CHAPTER 6

MODELING THE PROPAGATION OF OPTICAL BEAMS IN THREE-DIMENSIONAL PHOTONIC CRYSTALS

Now that we have developed an efficient simulation model for a spatially incoherent source, we move forward and propose to use three-dimensional (3D) photonic crystal (PC) structures [22-24] to merge the functionalities of both interferometric and diffractive elements together and replace the tandem spectrometer with an extremely compact properly designed 3D PC microspectrometer [25]. However, to design and implement these structures efficiently and systematically, it is essential to have a basic understanding of the propagation effects in 3D PCs.

In this chapter we show that the propagation effects of optical beams in 3D PC structures can be modeled using a direction-dependent effective diffractive index model. The parameters of the model (i.e., the effective diffractive indices) can be calculated using the curvatures of the band structure of the PC at the operation point. After finding these indices, the wave propagation inside the PC can be analyzed using simple geometrical optics formulas. As an example, the application of the model for diffraction compensation in a tetragonal woodpile PC is demonstrated.

6.1. Diffractive Index Model for 3D PCs

The problem of interest in most dispersive applications of PCs is the modeling of evolution of optical beams propagating through the periodic structure. Recently, some models have been suggested to describe these effects for special cases [88, 89], but a general model for 3D PCs is still missing. To analyze these structures, modal approaches

can be directly used by expanding the beam over the modes of the PC structure. This, however, requires a detailed mode matching process, which is a tedious task. At the same time, in most dispersion-based applications of PCs we are not interested in the details of the beam profile inside the periodic structure. In most practical cases, accurate description of the behavior of the envelope of the optical beam is of main interest. In this section, we develop an easy to use model for the analysis of the envelope of an optical beam as it propagates through a 3D PC structure. This model can also provide useful insight into the process of beam propagation through 3D PC structures. It has been shown that in 2D PCs an envelope transfer function (ETF) (using the band structure) can be defined to model the evolution of the special envelope of the beam inside the PC structure [90]. Here, we extend this idea to define the amplitude transfer function for 3D PCs [91]. Local quadratic approximation of the band structure at the operation point is then used to define diffractive indices that describe the diffraction of optical beams inside the PC structure at different wavelengths.

One main concept that differentiates between the 3D and the 2D PCs is the vectorial nature of the electromagnetic fields in the 3D case, which cannot be modeled using scalar quantities as in the 2D case. Nevertheless, it can be shown that the polarization of the modes of 3D PC structures in most practical cases have Bloch components with well-defined transverse eigenstates [92]. In addition, these polarization states have smooth variations over the band structure. As a result, an optical beam with limited spatial-spectral content in a 3D PC can be locally modeled using a scalar field by projecting its actual vector field over the dominant polarization state. In what follows, such a scalar model is used to develop approximate solutions.

For simplicity, we consider a tetragonal woodpile 3D PC in our derivations. The formulation can be extended readily to other lattices, and the results are not limited to the choice of lattice. Assume we have an optical beam with an initial scalar (electric or magnetic) field distribution $p_1(x,y)$ along $z = z_1$ (i.e., a plane normal to the z-axis) inside the PC. We can expand this distribution over the PC modes as

$$p_1(x,y) = \frac{1}{4\pi^2}\iint A(k_x,k_y)U_{\bar{k}}(x,y,z_1)\exp(-jk_x x - jk_y y)\exp(-jk_z z_1)dk_x dk_y , \tag{6.1}$$

where each PC mode is represented by an excitation amplitude [i.e., $A(k_x,k_y)$], a periodic Bloch function [i.e., $U_{\bar{k}}(x,y,z)$], and a propagation term [i.e., $\exp(-jk_x x - jk_y y - jk_z z)$], and the integration is performed over the entire 2D k_x-k_y plane. The periodic Bloch function can be expanded as a Fourier series

$$U_{\bar{k}}(x,y,z) = \sum_m\sum_n\sum_l \widetilde{U}_{mnl}(k_x,k_y,k_z)\exp[-j(mK_x x + nK_y y + lK_z z)]. \tag{6.2}$$

in which, $K_x = 2\pi/a_x$, $K_y = 2\pi/a_y$, and $K_z = 2\pi/a_z$ are the reciprocal lattice vectors of the PC in the k-domain (a_x, a_y, and a_z are the corresponding lattice constants in the x, y, and z directions, respectively). The initial scalar field expansion, thus, can be written as

$$\begin{aligned} p_1(x,y) = \frac{1}{4\pi^2}\iint A(k_x,k_y)\Big(\sum_m\sum_n\sum_l \widetilde{U}_{mnl}(k_x,k_y) \\ \times\exp[-j(k_x + mK_x)x]\exp[-j(k_y + nK_y)y]\exp[-j(k_z + lK_z)z_1]\Big)dk_x dk_y \end{aligned} \tag{6.3}$$

where $\widetilde{U}_{mnl}(k_x,k_y)$ represents the Fourier expansion coefficient of the periodic Bloch function. Note that since this expansion corresponds to a specific operation frequency, by fixing k_x and k_y, the third component of the wavevector of the PC mode, k_z, will be known [i.e., k_z is a function of k_x and k_y, or $k_z = k_z(k_x,k_y)$], and this fact has been used in Equation (6.3).

The 2D spatial Fourier transform of the field distribution, $p_1(x,y)$ can be calculated as

$$\begin{aligned} P_1(k_x,k_y) &= \iint p_1(x,y)\exp(jk_x x)\exp(jk_y y)dxdy \\ &= \sum_m\sum_n\sum_l A(k_x',k_y')\widetilde{E}_{mnl}(k_x',k_y')\exp\{j[k_z(k_x',k_y')+lK_z]z_1\}\Big|_{\substack{k_x'=k_x-mK_x \\ k_y'=k_y-nK_y}} \end{aligned}, \tag{6.4}$$

or

$$\begin{aligned} P_1(k_x,k_y) = \sum_m\sum_n\sum_l & A(k_x-mK_x,k_y-nK_y)\widetilde{E}_{mnl}(k_x-mK_x,k_y-nK_y) \\ & \times\exp\{j[k_z(k_x-mK_x,k_y-nK_y)+lK_z]z_1\} \end{aligned}. \tag{6.5}$$

Assuming that the beam profile covers a limited spectrum around $(k_x,k_y)= (k_{x0},k_{y0})$, we can extract the envelope of the beam by filtering out the high-frequency portion of the spectrum around (k_{x0},k_{y0}) and moving it to the baseband by shifting the spectrum by $-k_{x0}$ and $-k_{y0}$ in the k_x and k_y directions, respectively [90]. The resulting spectrum of the envelope, represented by $\overline{P}_1(k_x,k_y)$, is

$$\begin{aligned} \overline{P}_1(k_x,k_y) = & A(k_x+k_{x0},k_y+k_{y0})\exp[jk_z(k_x+k_{x0},k_y+k_{y0})z_1] \\ & \times\left(\sum_l \widetilde{E}_{00l}(k_x+k_{x0},k_y+k_{y0})\exp(jlK_z z_1)\right) \end{aligned}. \tag{6.6}$$

Note that all $m\neq 0$ and $n\neq 0$ in Equation (6.5) correspond to the higher spatial frequency terms corresponding to rapid spatial variations in the length scales smaller than a PC unit cell. For the analysis of propagation of optical beams in a dispersive PC structure, the optical beam usually covers multiple unit cells, and such rapid variations will not be of interest in designing PC structures for practical applications.

At the monitoring output plane, $z = z_2$, the spectrum of the envelope of the beam can be calculated as

$$\overline{P}_2(k_x,k_y) = A(k_x+k_{x0},k_y+k_{y0})\exp[jk_z(k_x+k_{x0},k_y+k_{y0})z_2] \times\left(\sum_l \widetilde{E}_{00l}(k_x+k_{x0},k_y+k_{y0})\exp(jlK_z z_2)\right) \quad . \tag{6.7}$$

If $z_2 - z_1 = 2\pi q/K_z$ (with q being an integer), the summation term in Equations (6.6) and (6.7) will be exactly the same, resulting in

$$\overline{P}_2(k_x,k_y) = \overline{P}_1(k_x,k_y)\exp[jk_z(k_x+k_{x0},k_y+k_{y0})(z_2-z_1)], \tag{6.8}$$

which means that the effect of propagation from $z = z_1$ to $z = z_2$ on the envelope of the beam is only a phase change in the spectral domain similar to a plane-wave-type propagation with propagation constant k_z. Thus, the main effect of propagation in 3D PCs on the beam envelope is the phase variations of the modes from the initial plane to the observation plane.

Based on Equation (6.8), we can define an ETF for the structure to describe the propagation from the $z = z_1$ plane to the $z = z_2$ plane as

$$H(k_x,k_y) = \frac{\overline{P}_2(k_x,k_y)}{\overline{P}_1(k_x,k_y)} = \exp[j(z_2-z_1)k_z], \tag{6.9}$$

where $k_z = k_z(k_x+k_{x0},k_y+k_{y0})$ is related to k_x and k_y through the dispersion relation of the structure at the constant temporal frequency (ω) of the beam. The ETF for 3D PCs [given by Equation (6.9)] is similar to what was obtained for 2D PC structures [90], with the main difference being the extension of the ETF from a single variable function to a two-variable one. Using the analogy with propagation in bulk media, we can extend Equation (6.9) to the case of beam propagation along the ζ direction (normal to the constant frequency surface at the point of operation, i.e., parallel to $\mathbf{v}_g = \nabla_{\mathbf{k}}\omega$) as

$$H(k_\xi, k_\eta) = \frac{\overline{P}_2(k_\xi, k_\eta)}{\overline{P}_1(k_\xi, k_\eta)} = \exp[-j(\zeta_2 - \zeta_1)k_\zeta(k_\xi, k_\eta)], \tag{6.10}$$

where the coordinates ξ, η, and ζ are defined in Figure 6.1.

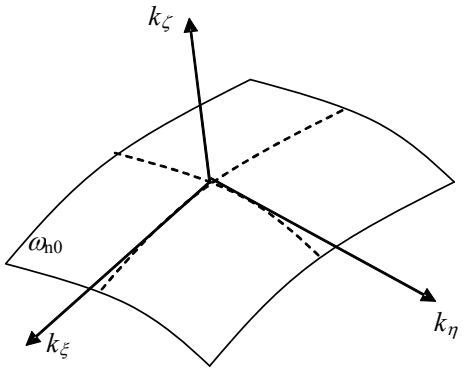

Figure 6.1. A portion of an iso-frequency surface (at normalized frequency ω_{n0}) of a general 3D PC in the *k*-space is shown. The directions tangent to the surface (i.e., ξ and η) and the direction normal to the surface (ζ) are defined in the figure.

Equation (6.10) can be used readily to investigate beam propagation effects for the most general case inside a 3D PC. The analogy with propagation in normal bulk media can be further utilized, if we express the exponential term of the spectral response in Equation (6.9) in terms of its Taylor expansion. Knowing that the diffraction of an optical beam (defined by ω and $\mathbf{k}$) inside a PC is governed by the curvatures of the constant frequency surface at the operation point, we need to first calculate the PC band curvatures at the operation point. Using the second order approximation,

$$\begin{aligned} k_z = k_{z0} + a_2(k_x - k_{x0}) + a_3(k_y - k_{y0}) + a_4(k_x - k_{x0})^2 \\ + a_5(k_x - k_{x0})(k_y - k_{y0}) + a_6(k_y - k_{y0})^2 \end{aligned}, \tag{6.11}$$

a standard method can be adopted to find these curvatures [93]. First, we define *W* as the magnitude of the gradient at the operation point, given by

$$W = \sqrt{1 + a_2^2 + a_3^2}\ . \tag{6.12}$$

Then, the parameters for the first fundamental form of the surface (associated with the tangent plane) can be found as [93]

$$\begin{cases} E = (1 + a_2^2)W \\ F = a_2 a_3 W \\ G = (1 + a_3^2)W \end{cases}, \tag{6.13}$$

and those of the second fundamental form (associated with the second-order curvatures) can be calculated as

$$\begin{cases} L = 2a_4 \\ M = a_5 \\ N = 2a_6 \end{cases}. \tag{6.14}$$

Using these relations, which are coefficients of the fundamental forms of a quadratic surface, we can calculate the Gaussian curvature as

$$K = \frac{LN - M^2}{EG - F^2}, \tag{6.15}$$

and the mean curvature as

$$H = \frac{1}{2}\frac{EN - 2FM + GL}{EG - F^2}. \tag{6.16}$$

Finally, the two principal curvatures can be calculated as

$$\kappa_1 = H + \sqrt{H^2 - K}, \tag{6.17}$$

$$\kappa_2 = H - \sqrt{H^2 - K}. \tag{6.18}$$

The principal directions, $\mathbf{v}_i$, can be calculated by inserting these principal curvatures in the characteristic equation,

$$\begin{pmatrix} L - \kappa_i E & M - \kappa_i F \\ M - \kappa_i F & N - \kappa_i G \end{pmatrix} \mathbf{v}_i = 0 \qquad i = 1,2, \tag{6.19}$$

which determines the principal directions projected on the *xy*-plane. From these directions, we can find the two directions at the operation point on the band structure, which are normal to the gradient direction,

$$\mathbf{n} = (-a_2, -a_3, 1). \tag{6.20}$$

The two directions obtained from this process determine the principal directions corresponding to the principal curvatures at the operation point on the band structure. Since these curvatures describe the diffraction of the optical beam inside the structure, we will refer to these two principal directions as the principal diffraction directions. Without loss of generality we assume the directions of ξ and η in Figure 6.1 to be along the principal diffraction directions at the operation point. Note that in the special case that the two curvatures are equal (i.e., the degenerate case), the choice of the principal diffraction directions is arbitrary.

To summarize, for each mode of the 3D PC structure (at a given ω and **k**), there are two principal diffraction directions in the plane perpendicular to the direction of group velocity for that mode. A principal diffractive index can be defined for each of these directions to describe the diffraction of an optical beam along that specific direction. Based on the analogy with bulk media, we can find the principal diffractive indices ($n_{d\xi}, n_{d\eta}$) at the operation point as

$$\begin{cases} n_{d\xi} = \dfrac{1}{k_0 \kappa_1} \\ n_{d\eta} = \dfrac{1}{k_0 \kappa_2} \end{cases}. \tag{6.21}$$

The same phenomenon of anisotropic diffraction, in principle, occurs in ordinary anisotropic media as well, but the extent of the contrast between the two principal

diffractive indices can be much larger in 3D PCs (for instance they can have opposite signs), and the beam propagation in 3D PCs can show practically significant effects from a device point of view. Equation (6.21) is the final result of our model. To implement this model for an arbitrary 3D PC, we need to first calculate the 3D band structure, which can be efficiently done by analyzing one unit cell of the PC structure using a standard technique such as plane wave expansion or FDTD. Then, we can calculate the curvatures of the iso-frequency surface of the band structure at the operation point of interest. The advantage of this model is that the calculation of curvatures is fast (much faster than the analysis of wave propagation in even a small 3D PC). Furthermore, once the diffractive indices are calculated, they can be readily used to study propagation effects of optical beams for different propagation lengths and in a variety of applications of that PC structure.

6.2. Simulation Results

To verify the applicability of our approximate diffractive index model, we investigate the propagation of a Gaussian beam inside a woodpile PC structure with a tetragonal unit cell [as shown in Figure 6.2(a)] with $f_x = f_y = 0.3$, $f_z = 0.5$, and $a_z = 2.4a_x = 2.4a_y = 2.4a$. The relative permittivity of the material used for fabricating the 3D PC is assumed to be ε_r = 2.5 throughout this chapter, which is the typical value in structures realized in polymer-based PCs. We assume the incident wave to be a Gaussian beam coming from a homogeneous bulk material (with $\varepsilon_r = 2.5$) at $\alpha = 38°$ and $\phi = 0°$ [i.e., propagation in the *xz*-plane in Figure 6.2(b)], where α is the angle between the incident wavevector and the *z*-axis, and ϕ is the angle between the plane of incidence and the *x*-axis as shown in Figure 6.2(b). For this lattice, the dominant polarizations of the PC modes are very close

to the conventional transverse electric (TE) and transverse magnetic (TM) polarizations [92]. By direct calculation, we can also verify that the principal diffraction directions in this case are parallel and normal to the *xz*-plane. Figure 6.3 shows the cross-section of a Gaussian beam inside this PC structure at different propagation lengths. The beam is assumed to be at normalized frequency of $a/\lambda = 0.45$ with TE polarization (electric field normal to the plane of incidence) and a symmetric shape with a beam waist of 41.2λ upon entrance to the PC structure. Results in Figure 6.3(a) are calculated using a direct modal approach based on the plane wave expansion technique as a point of reference, and those in Figure 6.3(b) are calculated using our ETF discussed in this chapter. The fluctuations on the profile of the beam for the exact method (i.e., the direct modal approach) are caused by the nonuniformity of the refractive index inside the photonic crystal structure. It can be observed that the approximate profile calculated by the ETF is an accurate estimate for the envelope of the beam for most practical purposes.

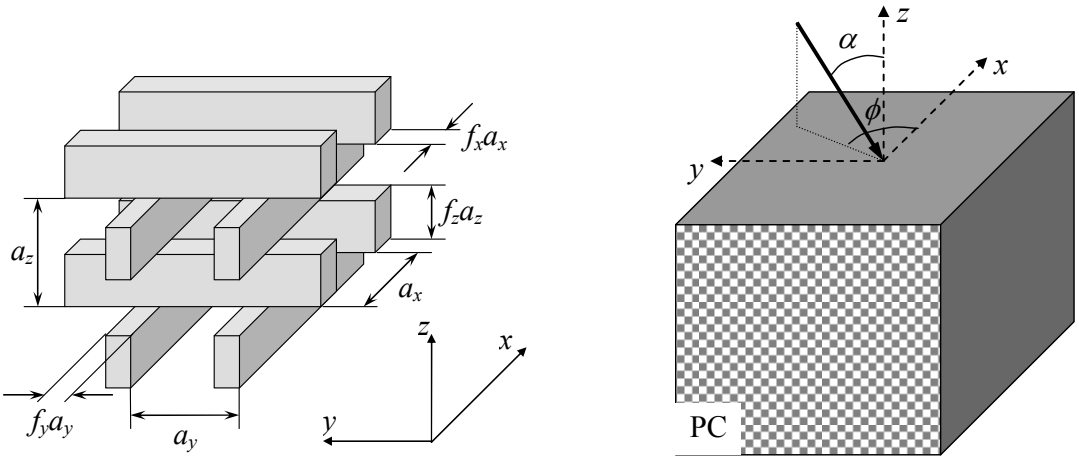

Figure 6.2. (a) The schematic demonstration of the 3D tetragonal woodpile PC considered throughout this chapter is shown. Lattice constants and filling factors in different directions of this lattice are marked on this figure. (b) The general direction of the incident beam is shown, with α being the angle between the incident wavevector and the normal to the interface (z), and ϕ being the angle between the plane of incidence and the *xz*-plane.

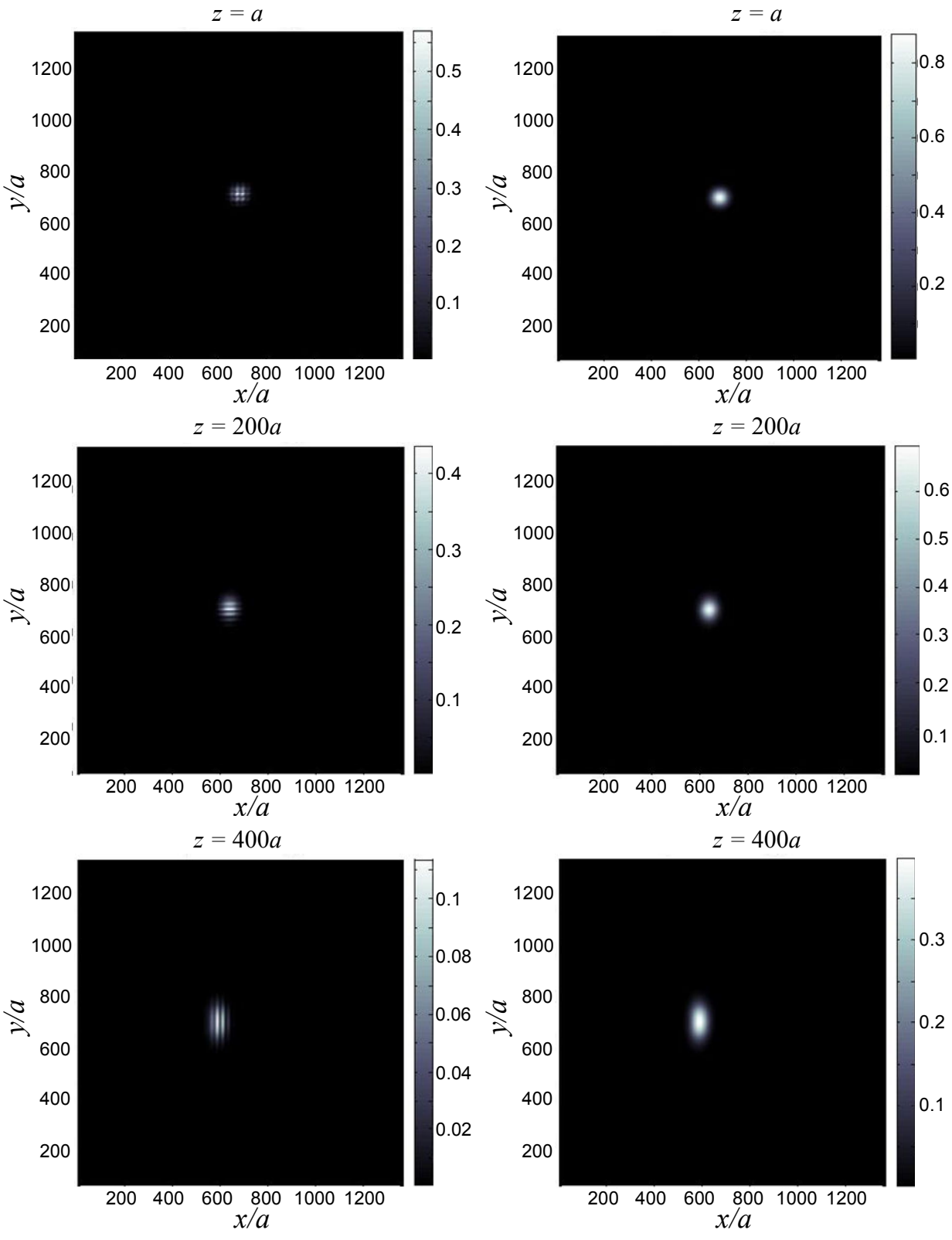
z = a
z = 200a
z = 400a
y/a
x/a
200 400 600 800 1000 1200
0.5 0.4 0.3 0.2 0.1
0.8 0.6 0.4 0.2
0.4 0.3 0.2 0.1
0.6 0.5 0.4 0.3 0.2 0.1
0.1 0.08 0.06 0.04 0.02
0.3 0.2 0.1

(a) (b)

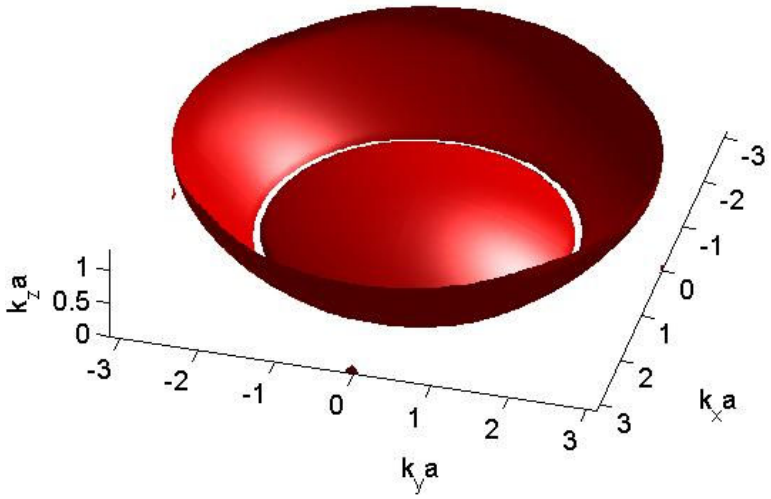

Figure 6.3. Calculated cross-sections of an optical beam propagating through a tetragonal woodpile PC structure (with $f_x = f_y = 0.3$, $f_z = 0.5$, and $a = a_x = a_y = a_z/2.4$) are shown at different propagation lengths using (a) the direct mode-matching (brute-force approach) and (b) the envelope transfer function approximation. The three snap-shots show the calculated E_y field at $z = a$, $200a$, and $400a$, respectively. The beam has a normalized frequency of $a/\lambda = 0.45$ and a symmetric beam waist of 41.2λ, and it is incident upon the PC from a homogeneous material with relative permittivity 2.5 at $\alpha = 38°$ and $\phi = 0°$ as shown in Figure 2. (c) Iso-frequency surface of the tetragonal woodpile PC used here at the normalized frequency of $a/\lambda = 0.45$.

Different broadenings in the two principal directions are also evident from the beam shapes in Figure 6.3. Figure 6.3(c) shows the iso-frequency surface of the 3D PC used in Figures 6.3(a) and (b) at the normalized frequency of $a/\lambda = 0.45$. The deformation of the bands in the vicinity of the edges of the Brillouin zone is responsible for the anisotropic curvature resulting in the different diffraction of the beam in the *x* and *y* directions, as shown in Figures 6.3(a) and (b). To get a more quantitative result, we have calculated the beamwidths in the two principal diffraction directions [i.e., *x* and *y* in Figure 6.2(b)] at different propagation lengths and the results are shown in Figure 6.4. Agreement between the beamwidths obtained by the diffractive index model and the ETF technique is clear from Figure 6.4. The results in Figure 6.4 confirm that the beamwidth

of the propagating beam in the photonic crystal structure follows the same simple geometrical optics relation predicted by the diffractive index model.

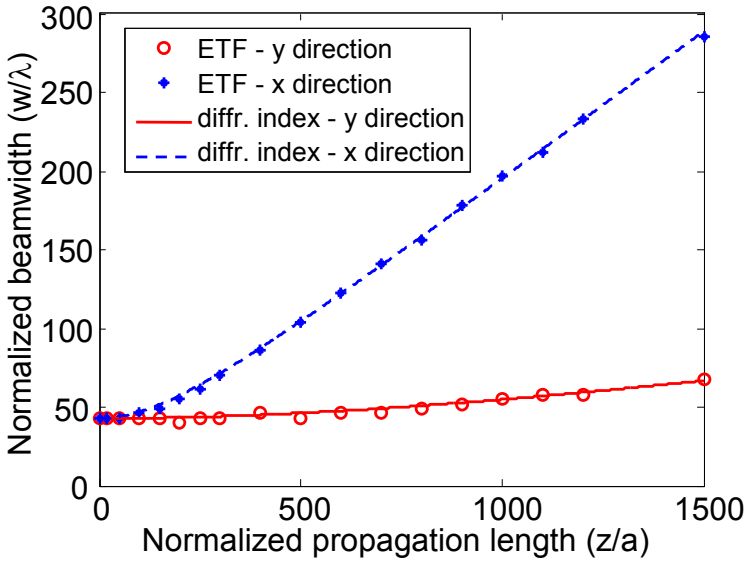

Figure 6.4. Comparison of the beamwidths along the *x* and *y* directions for an optical beam propagating inside a 3D PC (same parameters as defined in Figure 6.3). The results obtained using the ETF (shown by markers) are in good agreement with the expected beamwidths from a diffractive index model (shown by solid curves).

6.3. Negative Diffraction

The possibility of negative diffraction in PC structures is another important property that can affect an optical beam propagating inside these structures. The immediate applications of this property are diffraction compensation [94] and beam shaping. To obtain an appropriate 3D PC structure with negative diffraction, we can use our diffractive index model and design the PC structure for the desired diffractive indices along the two principal diffraction directions. More importantly, we can use these indices along with the well-known analytical formulas of geometrical optics to analyze the propagation of the optical beam in such a negative diffraction structure at any arbitrary propagation length [94].

For this analysis, we consider an incident Gaussian beam at the normalized frequency of $a/\lambda = 0.57$ with the symmetric beam waist of 20.6λ incident at an angle $\alpha = 21.75°$ and $\phi = 0°$ from the substrate region on the 3D PC structure in the geometry shown in Figure 6.2(b). We choose a woodpile PC structure with $a_x = a_y = a$, $a_z = 2.4a$, $f_x = f_y = 0.3$, $f_z = 0.5$, and $\varepsilon_r = 2.5$, similar to the one in Figure 6.2. The 3D iso-frequency surface for this PC at the operation normalized frequency is shown in Figure 6.5(a). The excitation point on the band structure is marked by an arrow in Figure 6.5(a), showing that the iso-frequency surface at this operation point has different curvatures in the x and y directions. We assume that the beam initially propagates a distance of $L_{pre} = 1960a$ in the substrate with $\varepsilon_r = 2.5$ (and thus, broadens to a beam spot of $2w = 77\lambda$ in each lateral direction) before entering the PC. The two diffractive indices for this structure at the operation frequency of $a/\lambda = 0.57$ are $n_{dx} = -0.16$ and $n_{dy} = 0.90$ [calculated from the band structure using Equation (6.21)]. The beam profiles normal to the direction of propagation (the z direction) at two different propagation lengths inside the PC structure are shown in Figures 6.5(b) and (c). Perfect diffraction compensation in the x direction at $L = 500a$ is observed from Figure 6.5(c), and the transfer-limited spot size is retrieved. Further propagation inside the PC region beyond this point results in the broadening of the beam. It is interesting to note the difference between the diffraction effects in the x and y directions. The beam undergoes normal diffraction in the y direction and continues to broaden upon propagation (since $n_{dy}>0$), while the diffraction effect in the x direction is opposite to that of ordinary bulk materials (since $n_{dx}<0$), and results in focusing of the beam. Figure 6.6 compares the widths of the beam in the x and y directions obtained from direct ETF simulations with those obtained by fitting Gaussian

beam propagation into the calculated data based on a modal analysis. The estimated diffractive indices in the x and y directions from this fitting process are n_{dx} = -0.14 and n_{dy} = 0.87, respectively, which are in good agreement with direct calculations of diffractive indices from the band structure.

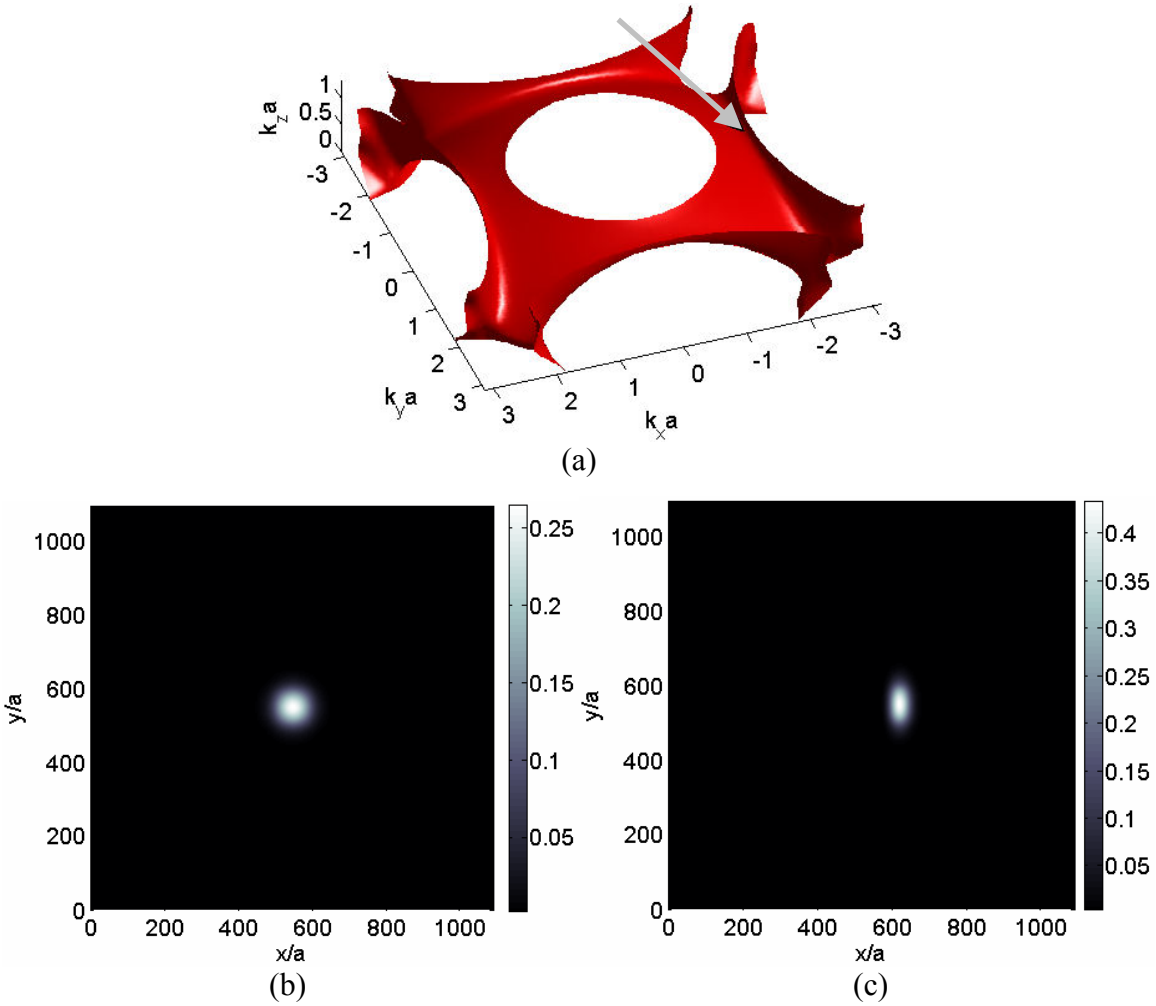

Figure 6.5. (a) Iso-frequency surface of a tetragonal woodpile PC structure (with $f_x = f_y = 0.3$, $f_z = 0.5$, $\varepsilon_r = 2.5$, and $a = a_x = a_y = a_z/2.4$) in the 3D k-space at the normalized frequency of a/λ = 0.57 is shown. Only the surface corresponding to the excitation polarization (i.e., E_y) is retained. The excitation is a Gaussian beam incident from the substrate region ($\varepsilon_r = 2.5$) at an angle of $\alpha = 21.75°$ and $\phi = 0°$, with a symmetric beam waist of $2w_0 = 41.2\lambda$, and is originally broadened to a beamwidth of 77λ. Cross-sections of the beam inside the PC structure is shown at (b) $z = a$ (i.e., upon entrance to the PC region) and (c) $z = 500a$.

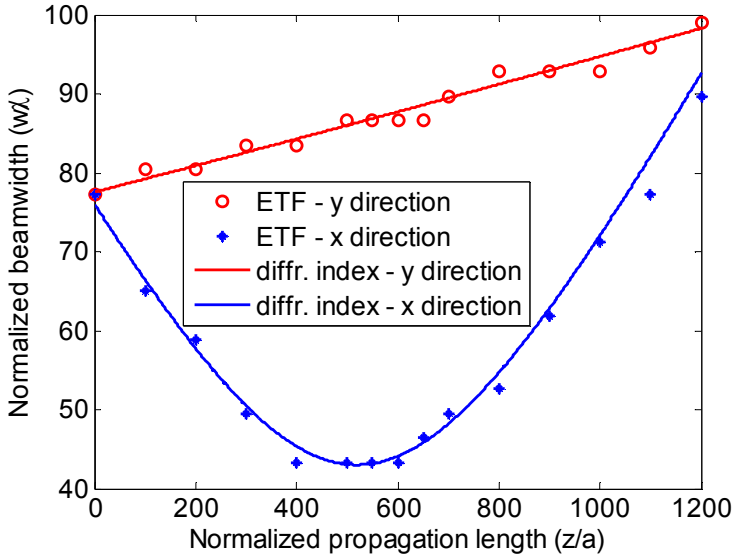

Figure 6.6. The evolution of the width of the beam during propagation through the PC structure is calculated using the ETF method and our simple diffractive index model, showing good agreement. Using Gaussian beam propagation formulas and by fitting the parameters into the calculated ETF beamwidths, the diffractive indices are estimated to be n_{dx} = -0.14 and n_{dy} = 0.87, which are in good agreement with those calculated in our simple model.

It is clear that choosing an appropriate 3D PC structure for diffraction compensation and confirming its effect on the incident beam with direct simulation of propagation (using methods such as FDTD) is very time-consuming. This clearly shows the importance of our diffractive index model in the analysis, design, and optimization of 3D PC structures for practical applications.

CHAPTER 7

ANALYSIS AND DESIGN OF THREE-DIMENSIONAL PHOTONIC CRYSTAL DEMULTIPLEXERS

Photonic crystals (PCs) are periodically patterned synthetic optical materials that have shown a very strong capability to control the propagation of optical beams [26-30]. Because of their anomalous dispersion diagram, they can manipulate different wavelengths differently and hence they are very suitable materials for dispersive applications. There are many dispersive devices have been proposed so far to exploit different dispersion properties of PCs like superprism effect, negative diffraction, and super collimation [31-35]. Most of these proposals are in view of two-dimensional (2D) PCs as a design template and three-dimensional (3D) PCs did not get much attention because of the difficulties present in their fabrication process to make a uniform sample with desired lattice geometry. However, recent advances in the fabrication of 3D PC structures have resulted in the development of these structures for practical applications. Among a variety of dispersive applications of 3D PCs, here in this chapter we look into superprism-based 3D PC demultiplexers.

In conventional PC demultiplexers where optical beam diverges as propagates through the PC structure, for larger separation between different spectral channels we have to enlarge the PC region along the propagation direction. Knowing that 3D PC structures are fabrication limited to pretty small thicknesses, it is not practically possible to enlarge the propagation length inside the structure. Therefore, we have used an alternative configuration for the 3D PC demultiplexers as shown schematically in Figure

7.1 consists of a preconditioning region where the incident beam starts broadening before entering the 3D PC region. In this configuration the PC dispersion diagram is engineered to have negative effective diffractive index in addition to the superprism effect for all wavelength channels. Thus, different wavelength channels of the incident beam are angularly separated from each other inside the 3D PC by the superprism effect and are simultaneously focused back to their diffraction limited spot size at the output of the PC region because of the negative diffraction.

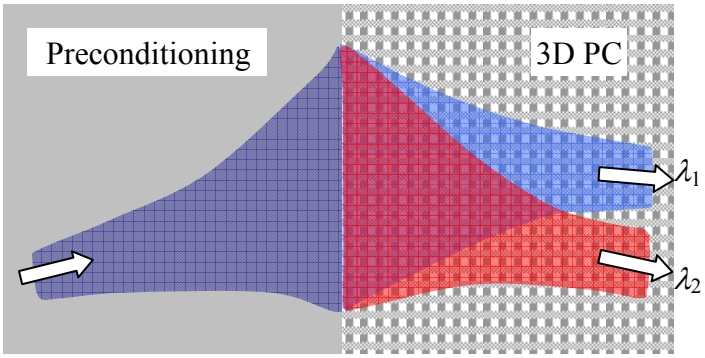

Figure 7.1. Schematic of a preconditioned superprism-based 3D PC demultiplexer.

In this chapter we present the analysis and design of preconditioned 3D PC demultiplexers as in Figure 7.1 where the simultaneous existence of the superprism effect and the diffraction compensation results in a very compact structure. We apply the effective diffractive index model developed in the previous chapter and use the same lines of formula already developed for the 2D case [94] and revise it properly for the quantitative analysis of the performances of the 3D PC demultiplexers and their optimization in regard of their size. Subsequently, a systematic design procedure for making the most compact preconditioned superprism-based 3D PC demultiplexer is presented. Later in this chapter, we will use tetragonal woodpile 3D PCs as a design

template for making practical demultiplexers. Finally, polarization states of modes of 3D PC structures are briefly discussed.

7.1. Analysis of Preconditioned Superprism-Based 3D PC Demultiplexers

At the beginning, it is worth mentioning that in our analysis we have assumed that the demultiplexer separates all the spectral channels in one dimension along its direction of angular separation. Therefore, all the theoretical formulations developed previously for 2D PCs [94] can be exactly repeated for 3D PCs with just taking into account that all the diffractive index orders are calculated from 3D PC band structures (i.e., iso-frequency surfaces) along the direction of angular separation. In other words, the systematic analysis and design of 3D PC demultiplexers are reduced into the analysis and design of 2D ones. In this case, the band structure of the reduced 2D PC demultiplexer (which is represented in the form of a constant frequency contour in the 2D wave-vector plane) is the intersection of the band structure of the 3D PC (which is represented in the form of an iso-frequency surface in the 3D wave-vector plane) and the plane of angular separation.

As mentioned already in the previous chapter, the diffraction of an optical beam in 3D PC is modeled by two diffractive indices. Here in the analysis and design of the reduced 2D PC demultiplexers, the second diffractive index in the direction perpendicular to the direction of angular separation is not entered and rather considered as a free design parameter. Nevertheless, the second diffractive index is preferred to be either equal to the first diffractive index (in both sign and value) or to be much larger than the first one so when the beam is diffraction compensated to its minimum waist by the PC region along the direction of angular separation, it is also very close to its minimum waist in the perpendicular direction.

The basic topology of the preconditioned superprism 3D PC demultiplexer with different important parameters is shown in Figure 7.2. There are two basic conditions that need to be satisfied in the demultiplexer, namely, spatial separation and diffraction compensation. Spatial separation refers to the different channels being separated in space at the output of the device. This is caused by the propagation of beams of different wavelength in different directions inside the structure. This separation can be quantified by defining cross-talk between channels as the sum of the powers of all undesired channels at the location of the desired channel. Diffraction compensation condition is the cancellation of second-order spectral phase from the input diffraction-limited incident beam to the output plane as designed. In this section, we follow the same lines of formulation developed in Reference [94] to express these two conditions in terms of actual physical design parameters for 3D PCs.

In Figure 7.2(a), we have shown the propagation of a Gaussian beam through the structure where $2w_0$ is the initial waist of the incident beam, α is the incident angle, and L and θ_g are respectively propagation length and propagation angle of the beam, corresponding to a single demultiplexing channel in the PC region. In addition, $2w_{PC} = 2w_0 \cos\theta_g / \cos\alpha$ is the beam waist in the direction of angular separation corresponding to that beam inside the 3D PC. Here, we consider the third order spectral phase to be the dominant term in the higher order effects; validity of this assumption can be easily checked for each design by comparing the contributions of different spectral phase orders. In case other spectral terms become dominant (for example, the fourth order spectral phase in the ideal structure) the same steps as below can be performed with the corresponding phase term. Figure 7.2(b) shows the evolution of the beam inside the

structure considering only the third-order spectral phase term. The output beam obtained in this way is the actual beam profile only at the output plane of the structure, where the effect of second-order spectral phase is designed to vanish.

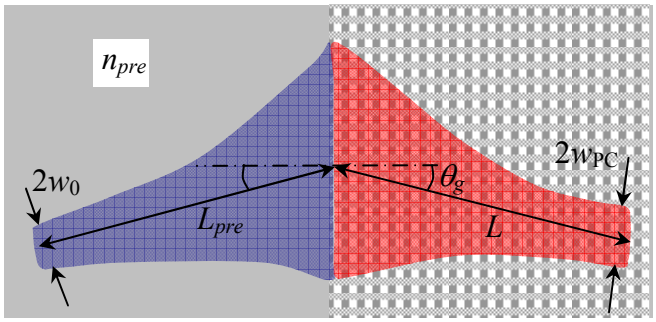

(a)

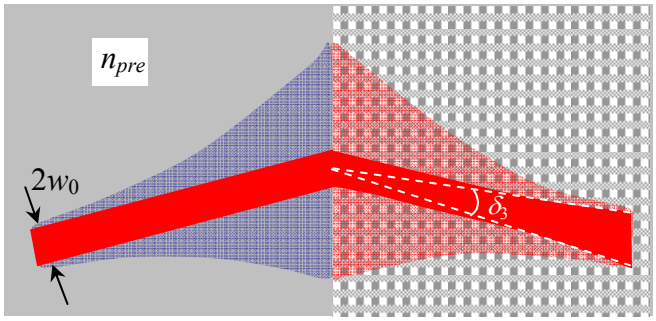

(b)

Figure 7.2. (a) Parameters for a preconditioned superprism 3D PC demultiplexer are depicted for an incident beam coming at an angle α, and for a single channel inside the PC region. (b) The darker pattern trace shows the evolution of an optical beam at a single wavelength throughout the structure without the effect of the second order diffraction. In this case, δ_3 is the divergence angle of the beam due to the third-order diffraction effect. The brighter pattern is the actual beam profile inside the structure. By compensating the second-order phase, the beam size at the output is the same as that in the assumed structure with zero second-order phase everywhere.

Calculation of the optimum propagation length L inside the PC depends on the amount of cross-talk required between adjacent wavelength channels at the output plane of the demultiplexer. The relative extent of two adjacent channels inside the PC is schematically shown in Figure 7.3(a), assuming that the two channels have equal divergence angles δ_3 and the angular separation between them is Δ. We can calculate

the required propagation length L, for achieving a cross-talk level of at most X as in Reference [42]

$$L = \zeta_3 z_3 , \tag{7.1}$$

where

$$\zeta_3 = \frac{K(X)}{\eta_3 - H(X)} . \tag{7.2}$$

In these relations, z_3 is the Rayleigh range corresponding to the third order spectral phase term, $\eta_3 = \Delta / \delta_3$ is the ratio of the angular separation between adjacent channels (Δ) to divergence angle of each channel due to the third-order diffraction effect inside the PC [as represented by δ_3 in Figure 7.2(b)], and K and H are constants given by Table 7.1 according to the required cross-talk. The procedure for calculating $K(X)$ and $H(X)$ is the same as that in Reference [42]. Equations (7.1) and (7.2) represent the spatial separation condition of output channels for preconditioned superprism 3D PC demultiplexers. Figure 7.3(b) shows the cross-talk versus propagation length for different ratios of angular separation η_3. Note that one major difference in the 3D case compared to the 2D case is the calculation of cross-talk where in the 3D case we have to consider the actual 2D Gaussian beam profiles at the output plane rather than the 1D Gaussian profiles in the 2D case.

Table 7.1. Cross-talk parameters

Cross-talk, X (dB)	$K(X)$	$H(X)$
-10	0.67	0.15
-20	0.88	0.38

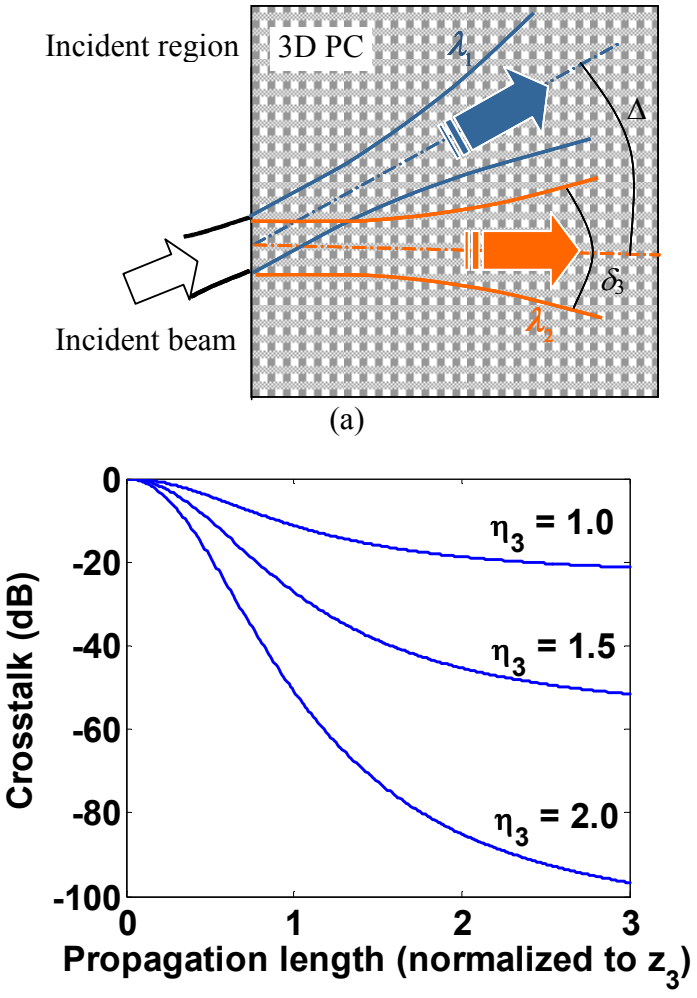

Figure 7.3. (a) Schematic evolution of beam profiles of two adjacent wavelength channels inside the PC structure. Δ is the angular spacing between group velocity directions of center frequencies of these two channels, and δ_3 is the divergence angle of one channel due to the third-order diffraction effect inside the PC region. (b) The cross-talk versus propagation length is shown for different values of η_3. Gaussian beam approximation is used in all cases.

The diffraction compensation condition that describes the cancellation of the overall quadratic phase can be simply put as

$$\frac{L_{pre}}{n_{pre}\cos^2\alpha} = \frac{L}{n_{e2}\cos^2\theta_g}, \tag{7.3}$$

in which n_{pre} and L_{pre} are the refractive index and the length of the preconditioning region, respectively. Also, n_{e2} and L are the effective index along the direction of angular separation and the propagation length of the 3D PC region, respectively. To assess the performance of the preconditioned superprism demultiplexers, here, we calculate the size of these structures for a given angular channel spacing, Δ. As it has been derived in Reference [94] for a beam propagating in a medium with third-order diffraction effects, we have $\delta_3 = 2\lambda/(\pi w_{PC} \mid n_{e3} \mid)$ and $z_3 = \frac{1}{2} k_0 w_{PC}^2 \mid n_{e3} \mid$, with $\mid n_{e3} \mid$ being the magnitude of the third-order effective index along the direction of angular separation of the 3D PC. By inserting these relations into Equation (7.2) we obtain

$$L = \zeta_3 z_3 = \frac{K}{\pi w_{PC} \mid n_{e3} \mid \Delta/2\lambda - H} (\frac{1}{2} k_0 w_{PC}^2 \mid n_{e3} \mid), \tag{7.4}$$

and therefore,

$$L = \frac{2K w_{PC}^3}{w_{PC}^2 \Delta - 2\sqrt{3} H \left| \partial^3 k_\eta / \partial k_\xi^3 \right|}. \tag{7.5}$$

The volume of the 3D PC (V) taken by each channel can be estimated as

$$V = \left(\frac{w_{PC}}{z_2} L \right)^2 L = \frac{32 K^3 w_{PC}^7 \left| \partial^2 k_\eta / \partial k_\xi^2 \right|}{\left(w_{PC}^2 \Delta - 2\sqrt{3} H \left| \partial^3 k_\eta / \partial k_\xi^3 \right| \right)^3}. \tag{7.6}$$

The volume in Equation (7.6) depends explicitly on the diffraction-limited beam waist of the channel inside the PC, $2w_{PC}$; thus, we can minimize the volume directly with respect to this parameter by using $\partial V / \partial w_{PC} = 0$ to obtain

$$(w_{PC})_{opt} = \left[\frac{14\sqrt{3} H}{\Delta} \left| \frac{\partial^3 k_\eta}{\partial k_\xi^3} \right| \right]^{1/2}, \tag{7.7}$$

which consequently results in the optimal propagation length (L_{opt}) as

$$L_{opt} = \frac{7K}{3\Delta}(w_{PC})_{opt}, \tag{7.8}$$

and the optimum (i.e., minimum) 3D PC volume (V_{opt}) as

$$V_{opt} = \frac{1372K^3}{27k_0^2 n_{e2}^2 \Delta^3}(w_{PC})_{opt}. \tag{7.9}$$

Following the same lines of formulation as in Reference [94], we can rewrite Equations (7.7)-(7.9) in terms of the physical parameters of the 3D PC structure.

7.2. Design of Preconditioned Superprism-Based 3D PC Demultiplexers

In this section we develop a design strategy for preconditioned superprism-based 3D PC demultiplexers. For any incident angle, we can find different parameters of the structure, i.e., angle of group velocity (θ_g), second-order effective index (n_{e2}), sensitivity factors [$\left(\partial\theta_g/\partial\omega\right)$ and $\left(\partial n_{e2}/\partial\alpha\right)$] as well as higher-order effective indices associated with each demultiplexing channel in our bandwidth of interest. Note that all these parameters are calculated from the band structure of the reduced 2D PC as already mentioned. These parameters describe the propagation behavior for each channel (i.e., direction of propagation, sensitivity to frequency, and the divergence caused by the third-order spectral phase term). To get the required cross-talk for all channels, the parameter w_i (i.e., the beam waist of the incident optical beam consisting of several wavelengths) should be found in such a way that the maximum propagation length required over all channels is minimized. This can be directly performed by reformulating Equation (7.5) as

$$L_j = \frac{2Kw_i^3 \cos^3\theta_{gj}}{w_i^2 \Delta_j \cos^2\theta_{gj} \cos\alpha - 2\sqrt{3}H\left|\partial^3 k_\eta / \partial k_\xi^3\right|_j \cos^3\alpha}, \tag{7.10}$$

in which subscript *j* stands for the parameters calculated for the *j*th channel. After finding w_i from this process, it is straightforward to set

$$L = \text{mean}\{L_j(w_i)\}, \tag{7.11}$$

and the length of the preconditioning region is found from Equation (7.3) as

$$L_{pre} = \frac{n_{pre}\cos^2\alpha}{n_{e2}\cos^2\theta_g} L, \tag{7.12}$$

which completes the design. Here, n_{pre} is the refractive index of the preconditioning region.

7.3. Results

Now we use the procedure of the previous section to design an optimal preconditioned 3D PC demultiplexer for a dense wavelength division multiplexing system operating around 1520nm. We use tetragonal woodpile PCs as a design template for making this kind of devices. The choice of woodpile structures is due to their more mature and controllable fabrication process rather than other 3D PC lattice geometries. They are fabricated by 3D patterning of a polymer material through a two-photon absorption technique and direct laser writing [47-49]. The relative permittivity of the polymer material is assumed to be $\varepsilon_r = 2.5$.

By direct search through the band structure of a woodpile PC structure with a tetragonal unit cell [as shown in Figure 6.2(a)] with $f_x = f_y = 0.3$, $f_z = 0.5$, and $a_z = 1.6a_x = 1.6a_y = 1.6a$, we look for a frequency range and an excitation point on the band structure to simultaneously achieve both superprism effect and negative diffraction along the direction of angular separation. Then, around the center frequency, the required

propagation length (L) and incident beam waist ($2w_i$) is found so that the desired cross-talk level for all channels is achieved. This process can be repeated for a range of incident angles to find the optimum structure for the given specifications. Note that the excitation point can be arbitrarily chosen by the incident angles α and ϕ, where α is the angle between the incident wavevector and the z-axis, and ϕ is the angle between the plane of incidence and the x-axis as shown in Figure 6.2(b). After searching through the band structure of the tetragonal woodpile PC introduced earlier, we have found that in the band TE_3 and in a small bandwidth around the normalized frequency of $a/\lambda = 0.66$ as shown in Figure 7.4, it is possible to excite the structure for achieving both superprism effect and negative diffraction. Here, we report on two different excitations of the structure, one at $\alpha = 30°$ and $\phi = 45°$, and the other at $\alpha = 20°$ and $\phi = 0°$, for designing a 4-channel and a 6-channel preconditioned demultiplexer, respectively.

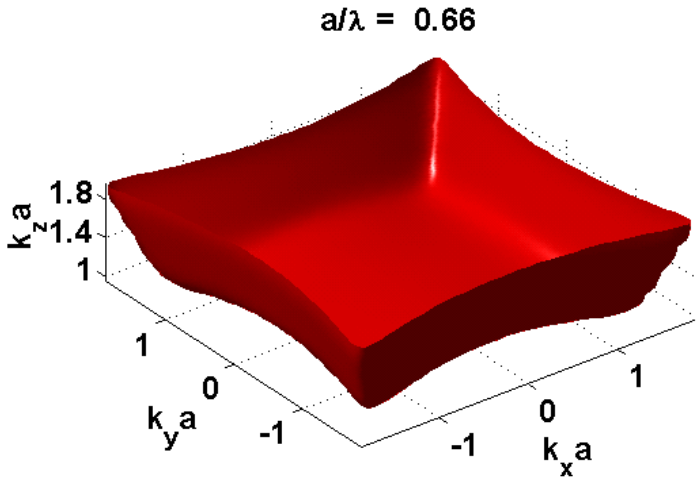

Figure 7.4. Iso-frequency surface of the tetragonal woodpile PC structure specified in the text at the normalized frequency of $a/\lambda = 0.66$.

7.3.1. Design of a 4-Channel 3D PC Demultiplexer

In this design we excite the PC structure with an incident beam coming from air at $\alpha = 30°$ and $\phi = 45°$. The incident beam is assumed to be a symmetric Gaussian beam. It propagates inside the PC structure in the direction normal to the iso-frequency surface at the excitation point. Figure 7.5 shows the group velocity angles α_g and ϕ_g versus normalized frequency. While beam keeps remaining in the $\phi = 45°$ plane, α_g is changing with frequency which is an evidence of the superprism effect. Therefore, as incident beam propagates through the PC structure different wavelength channels are dispersed in the $\phi_g = 45°$ plane. This observation confirms our assumption that we can reduce the 3D design problem into a 2D design problem by just looking into the band structure of the 3D PC in the $\phi = 45°$ plane.

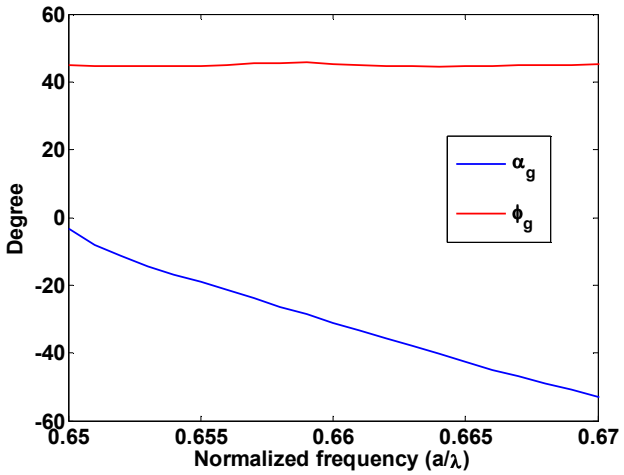

Figure 7.5. Group velocity angles α_g and ϕ_g versus normalized frequency for the tetragonal woodpile PC structure excited in band TE_3 with an incident beam coming from air at $\alpha = 30°$ and $\phi = 45°$. As seen in the figure ϕ_g remains constant and equal to 45°.

Figure 7.6 shows the constant frequency contours of the 3D PC structure in the $\phi = 45°$ plane as well as the loci of the points with the constant angle of incidence $\alpha = 30°$ in the wavevector space. We have calculated the group velocity angle (α_g)

inside the PC structure and the second-order effective index (n_{e2}) for the whole bandwidth of interest. Figure 7.7(a) shows the group velocity angle versus normalized frequency where the superprism effect is clearly seen. Another interesting point observed in this figure is the negative sign of the group velocity angle which is a result of negative refraction at the interface of the PC structure to air. Therefore, as the beam enters from air to the PC structure the desired signal encoded in the bandwidth of interest is separated from stray light (i.e., noise) and consequently the signal to noise ratio (SNR) at the output detector is improved. Figure 7.7(b) shows the second-order effective index versus normalized frequency. The negative sign of the effective index here helps to compensate the normal diffraction of the beam in the preconditioning region and focus it back to its initial waist, w_i. Moreover, the almost constant value of the effective index in the whole bandwidth gives us the opportunity to equally compensate the diffraction of all the signal channels. As a result, at the output detector all the channels reach their minimum waist simultaneously and therefore, crosstalk between adjacent channels is reduced.

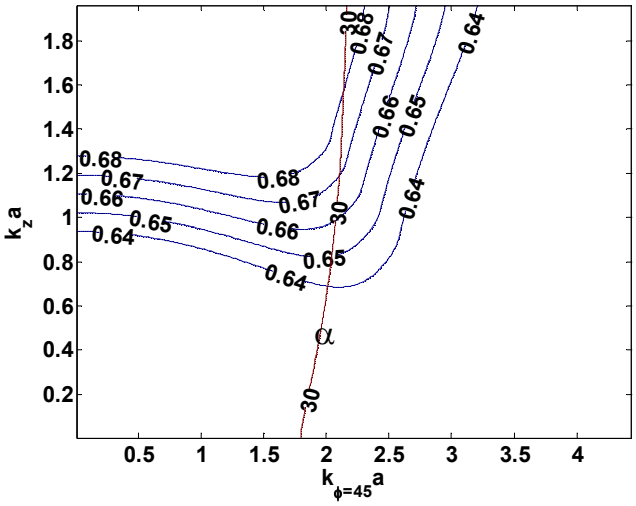

Figure 7.6. Constant frequency contours of the band TE_3 of the tetragonal woodpile PC structure in the $\phi = 45°$ plane. The curve marked with α corresponds to the angle of incidence $\alpha = 30°$.

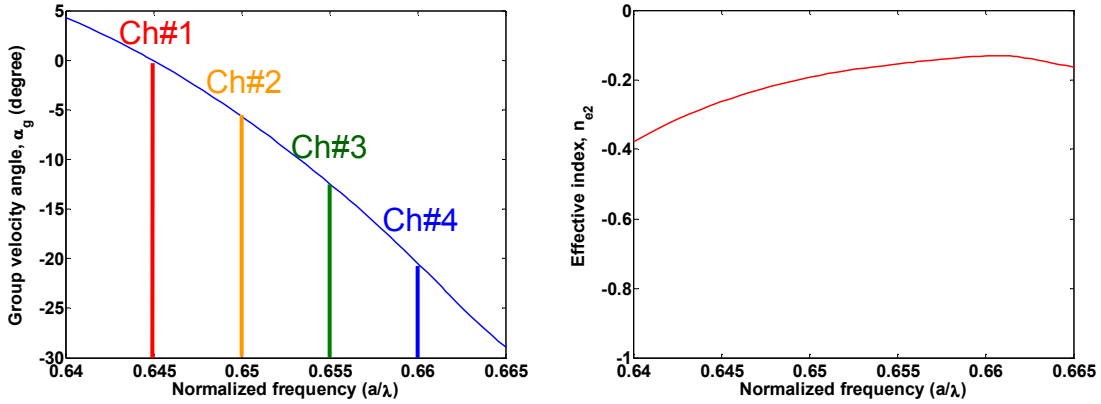

(a) (b)

Figure 7.7. (a) Group velocity angle versus normalized frequency for the 2D reduced tetragonal woodpile PC excited at $\alpha = 30°$ in the $\phi = 45°$ plane where its variation with frequency is an indication of the superprism effect. (b) Second-order effective index versus normalized frequency in the $\phi = 45°$ plane where its negative sign indicates the possibility of diffraction compensation.

For designing a 4-channel PC demultiplexer, four equally spaced channels in the bandwidth of interest as in Figure 7.7(a) have been chosen. Following the procedure outlined in the previous section we have calculated the length and the beam waist of each channel for achieving crosstalk level better than -10 dB and the results are listed in Table 7.2. For calculation of the actual wavelength values, we have assumed the lattice constant of the PC structure is equal to one micron (i.e., $a = 1\,\mu m$). We have fixed the length of the PC structure (L) in 120 μm which is the average of the lengths of the four channels. By using Equation (7.12) and the information given in Figure 7.7, we can calculate the length of the preconditioning region (L_{pre}) in Figure 7.2 for the center wavelength and it is found to be 650 μm. We have simulated the beam propagation for each channel through the whole demultiplexer region as in Figure 7.2 with a symmetric Gaussian profile and an initial waist of $2w_i = 20\,\mu m$. Figure 7.8 shows the -3 dB contour of output beam profiles of the four channels listed in Table 7.2 after passing through the PC structure. As expected the four channels are dispersed along the diagonal direction in the

$\phi = 45°$ plane. Although the second-order diffraction effect has been compensated and all channels almost reach their initial waist along the direction of angular separation, higher order diffraction effects deteriorate the beam shapes and result in asymmetric profiles in this direction. Presence of these higher order effects increases the interference between adjacent channels and hence makes the crosstalk level higher than -10 dB. Moreover, we did not try to harness the diffraction effects in the perpendicular direction normal to the $\phi = 45°$ plane and the beam is rather freely broadened in this direction. Therefore, the proposed demultiplexer despite of being functional in roughly separating four channels, is not very promising as the beam profiles do not look symmetric and well-shaped. This has motivated us to look for a subsequent design with better performance regarding the beam shapes.

Table 7.2. Design parameters for an optimal 4-channel demultiplexer in the tetragonal woodpile PC structure with $a = 1\,\mu m$ excited with an incident beam coming from air at $\alpha = 30°$ and $\phi = 45°$

Channel (nm)	$2w_i$ (μm)	L (μm)
$\lambda_1 = 1550$	14	189
$\lambda_2 = 1539$	13	140
$\lambda_3 = 1527$	12	111
$\lambda_4 = 1515$	7	49

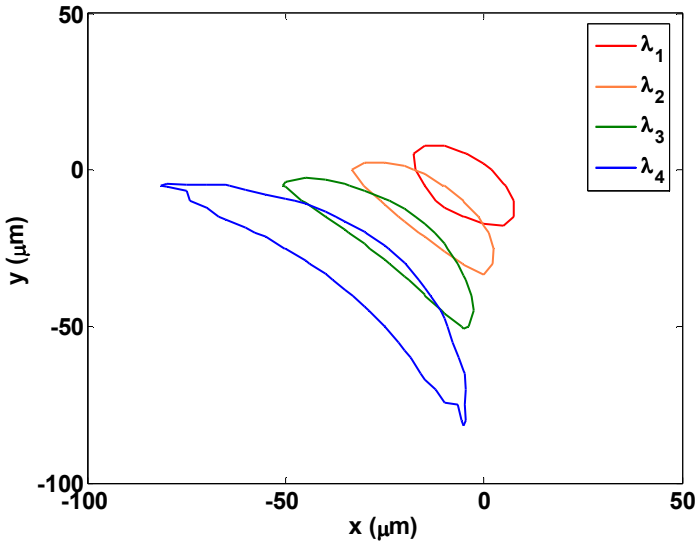

Figure 7.8. The -3 dB contour of the beam profiles of the four channels listed in Table 7.2 at the output plane of the preconditioned superprism-based demultiplexer shown in Figure 7.2 with $2w_i = 20\,\mu m$, $L_{pre} = 650\,\mu m$, and $L = 120\,\mu m$.

7.3.2. Design of a 6-Channel 3D PC Demultiplexer

For the second design we have excited the PC structure in band TE_3 with an incident beam coming from air at $\alpha = 20°$ in the *xz*-plane (i.e., $\phi = 0°$). All the other parameters are as before and the beam is assumed to be a symmetric Gaussian beam. The group velocity angles α_g and ϕ_g versus normalized frequency have been calculated and shown in Figure 7.9. As seen in the figure the beam keeps remaining in the *xz*-plane. Therefore, once again we can reduce the 3D PC demultiplexer design problem into a 2D design problem by just looking into the band structure of the 3D PC in the *xz*-plane as shown in Figure 7.10. We have calculated the group velocity angle (α_g) inside the PC structure and the second-order effective index (n_{e2}) for the whole bandwidth of interest and they have been shown in Figure 7.11.

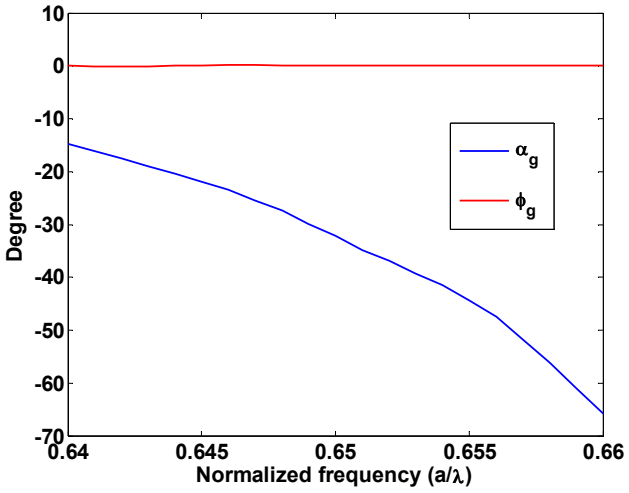

Figure 7.9. Group velocity angles α_g and ϕ_g versus normalized frequency for the tetragonal woodpile PC structure excited in band TE_3 with an incident beam coming from air at $\alpha = 20°$ in the *xz*-plane. As seen in the figure the beam keeps remaining in the *xz*-plane.

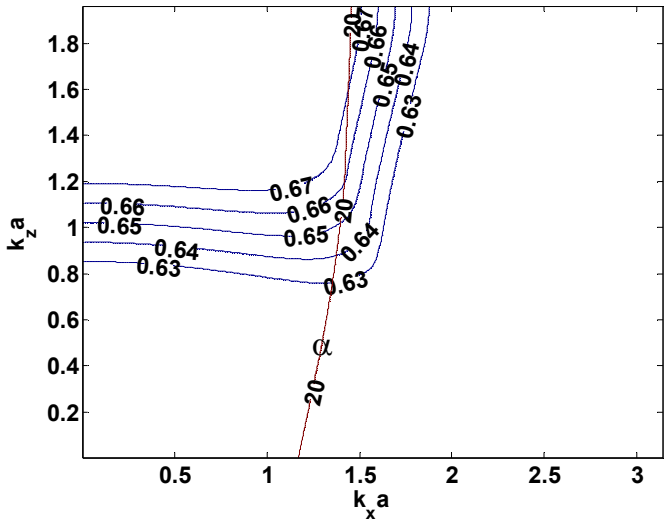

Figure 7.10. Constant frequency contours of band TE_3 of the tetragonal woodpile PC structure in the *xz*-plane. The curve marked with α corresponds to the angle of incidence $\alpha = 20°$.

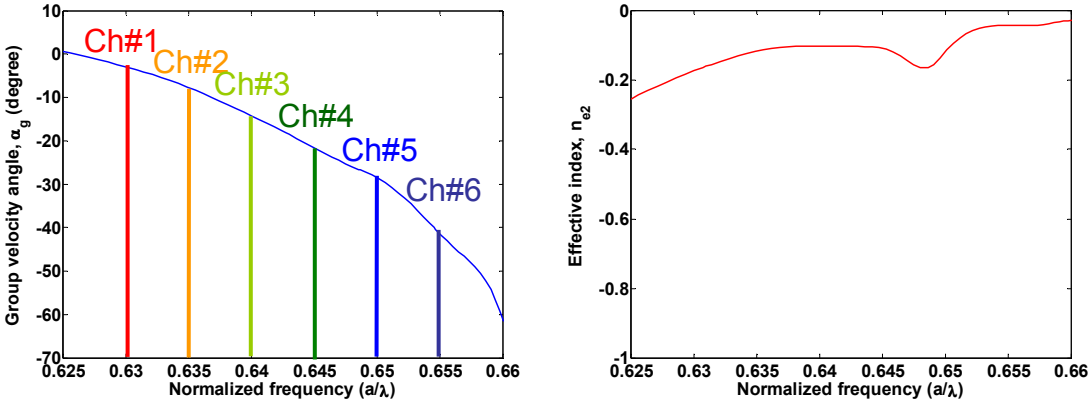

(a) (b)

Figure 7.11. (a) Group velocity angle versus normalized frequency for the 2D reduced tetragonal woodpile PC excited at $\alpha = 20°$ in the *xz*-plane where its variation with frequency is an indication of the superprism effect. (b) Second-order effective index versus normalized frequency in the *xz*-plane where its negative sign indicates the possibility of diffraction compensation.

For designing a 6-channel PC demultiplexer, six equally spaced channels in the bandwidth of interest as in Figure 7.11(a) have been chosen. Once again we have calculated the length and the beam waist of each channel for achieving crosstalk level better than -10 dB and the results are listed in Table 7.3. We have fixed the length of the PC structure (L) in 200 μm. By using Equation (7.12) and the information given in Figure 7.11, we can calculate the length of the preconditioning region (L_{pre}) in Figure 7.2 for the center wavelength and it is found to be 2250 μm. We have simulated the beam propagation for each channel through the whole demultiplexer region as in Figure 7.2 with a symmetric Gaussian profile and an initial waist of $2w_i = 40\,\mu m$. Figure 7.12 shows the -3 dB contour of output beam profiles of the six channels listed in Table 7.3 after passing through the PC structure. As expected the six channels are dispersed along the horizontal direction in the *xz*-plane. In this design the beam profiles look more symmetric compared to the first design and their diffractions along the *y*-direction (i.e., normal to the direction of angular separation) are pretty small. As seen in the figure yet

the presence of higher order diffraction effects increases the interference between adjacent channels along the *x*-direction and makes the crosstalk level higher than -10 dB.

Although the 6-channel demultiplexer proposed here shows better performance compared to the earlier 4-channel demultiplexer, it is twice thick as the first design. Considering challenges involved in the state of the art fabrication of 3D PC woodpile structures, it is not practically possible to fabricate PC samples thicker than 80 μm. Hence, the first design can be realized more practically.

Table 7.3. Design parameters for an optimal 6-channel demultiplexer in the tetragonal woodpile PC structure with $a = 1\,\mu m$ excited with an incident beam coming from air at $\alpha = 20°$ in the *xz*-plane

Channel (nm)	$2w_i$ (μm)	L (μm)
$\lambda_1 = 1587$	35	532
$\lambda_2 = 1575$	35	372
$\lambda_3 = 1563$	15	126
$\lambda_4 = 1550$	30	220
$\lambda_5 = 1539$	45	306
$\lambda_6 = 1527$	32	102

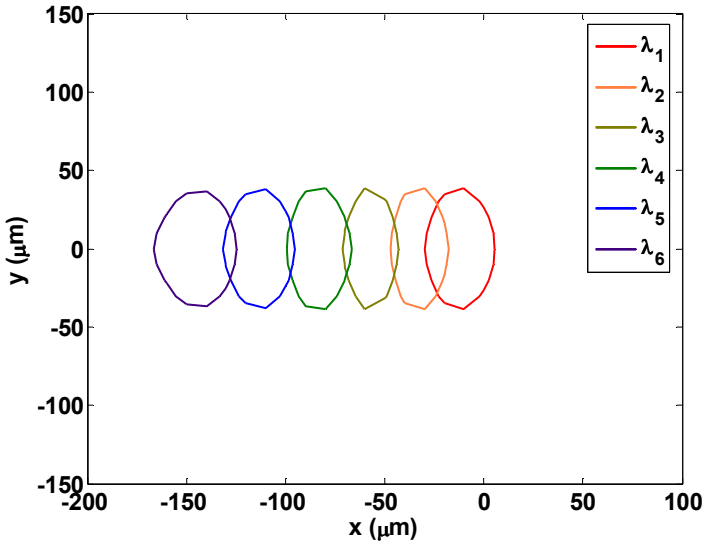

Figure 7.12. The -3 dB contour of the beam profiles of the six channels listed in Table 7.3 at the output plane of the preconditioned superprism-based demultiplexer shown in Figure 7.2 with $2w_i = 40\,\mu m$, $L_{pre} = 2250\,\mu m$, and $L = 200\,\mu m$.

Although we did not explicitly report on the spectrometers, the demultiplexers designed here can be renamed as a 3D PC microspectrometer as well since they map different wavelength channels to different locations. Therefore, our study to reduce the size of bulky spectrometers proposed earlier ended up with a successful and of course an initial realization of highly compact spectrometers.

7.4. Polarization State for Modes of 3D PC Structures

Another property that is desired for the better performance of the demultiplexer is the single mode excitation. Although not explicitly mentioned, both the 4-channel and the 6-channel demultiplexers are almost working under a single mode excitation. Because of the anomalous dispersion diagram of PCs, in a multimode excitation different modes can propagate in different directions, which results in an undesired division of the power through the structure and decreases the SNR on the detector. Hence, in most practical applications that we are targeting, to achieve higher SNR it is highly preferred to work in the single mode regime. In 2D PC structures most of the time we have two modes that can be selectively excited by choosing the proper incident polarization. One of the modes is TE polarized and the other one is TM polarized, and these two polarizations are orthogonal to each other. Unlike 2D PCs that we can exactly decouple TE and TM polarizations, in 3D PCs such a strict decoupling is not possible. We have observed that by searching through the band structure of the tetragonal woodpile PCs, there is a chance to find modes with TE-like or TM-like polarizations. This gives us an opportunity for possible single mode excitation of the woodpile PC structure by the right choice of the incident polarization very similar to the single mode excitation of the 2D PC devices.

For the tetragonal woodpile PC structure introduced in this chapter and excited at the normalized frequency of $\omega_n = 0.66$ with an incident beam coming from air at $\alpha = 30°$ and $\phi = 45°$, three modes, i.e., TE_3, TM_3, and TE_4, are excited. Figure 7.13 shows the polarization of the Bloch components of each PC mode. As seen in this figure the dominant Bloch components of the TE_3 and TM_3 modes are almost orthogonal and can be selectively excited. Moreover, the polarization of the third mode, i.e., TE_4, is rather different from those of the first two modes and potentially can be avoided from excitation.

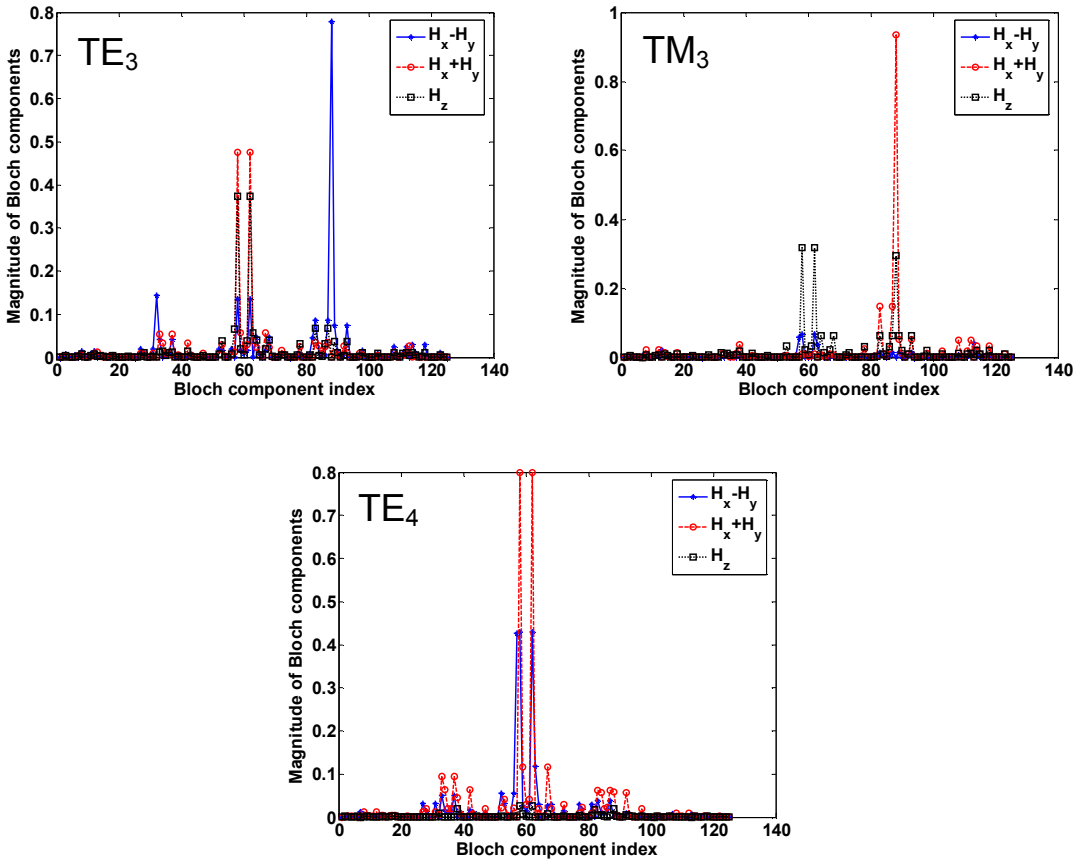

Figure 7.13. Polarization of all three excited PC modes versus the Bloch components for the tetragonal woodpile PC structure specified in the text. The PC structure is excited at the normalized frequency of $\omega_n = 0.66$ with an incident beam coming from air at $\alpha = 30°$ and $\phi = 45°$.

To investigate the possibility of the single mode excitation of this PC structure, we have calculated the transmitted power to each excited mode as a function of polarization angle δ which is the angle between magnetic field and plane of incidence in Figure 6.2(b). We have shown the coupling efficiency to each of these three PC modes versus δ in Figure 7.14. This figure illustrates that by choosing δ from 0° or 90° we can couple almost the whole transmitted power to the TM_3 or the TE_3 mode, respectively. As seen in the figure there is no chance for the TE_4 mode to be excited with substantial power at any incident polarization. Therefore, by proper choice of the incident polarization which is $\delta = 90°$, we can selectively excite the desired TE_3 mode in our designs proposed in the last section.

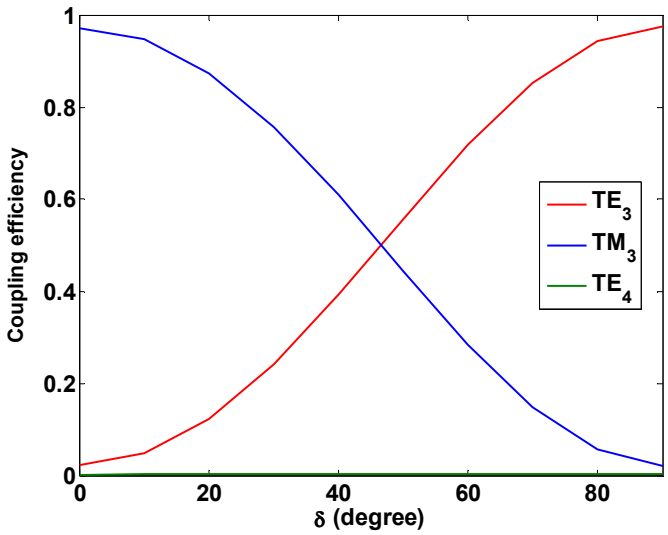

Figure 7.14. Coupling efficiency to the three excited PC modes versus the polarization angle δ. By the proper choice of polarization angle we can selectively excite on of the TE_3 or TM_3 modes. The TE_4 mode is not substantially excited at any incident polarization.

CHAPTER 8

CONCLUSION AND FUTURE WORK

The goal of this research has been the design and implementation of high resolution and large bandwidth free-space diffuse light spectrometers for biomedical and environmental sensing applications. To achieve this goal and make a spectrometer with state-of-the-art performance measures, we need to combine novel synthetic material properties and new device concepts using efficient design and optimization tools. Considering the material engineering, device innovation, and modeling and simulation tool development as the three primary areas of research in the invention of modern spectrometers, this thesis has been divided in three major parts. Although each part has been successfully completed, there are still some opportunities for future research in each part. In the following, a brief conclusion of each part in addition to its future research directions is presented. At the end, a brief summary of contributions and achievements of this research will be listed.

8.1. Design and Experimental Demonstration of a Diffuse Light Spectrometer using Conventional Spectroscopic Devices

In the first part we have analyzed the spatial-spectral response of the conventional spectrometers in two categories of the interferometric and the diffractive spectrometers for diffuse light spectroscopy where both types result in 1D spatial-spectral mapping at the output plane. We have shown that the normal gratings do not function properly under diffuse light illumination and we have introduced the CBVHs as a new class of diffractive and design-flexible diffuse spectrometers. Moreover, unlike SBVHs they do not affect the beam in the direction perpendicular to their diffraction direction.

To achieve high resolution as well as large bandwidth, we have proposed the tandem spectrometer combined of a FPE and a CBVH. In this configuration, the resolution is determined by the resolution of the FPE and the bandwidth is equal to the bandwidth of the CBVH. Moreover, the tandem spectrometer has a 2D spatial-spectral response at the output (or the CCD) plane. The high resolution spectral information is encoded along one direction by the FPE and the low resolution one is dispersed along the orthogonal direction by the CBVH. For the one to one spatial-spectral encoding, the resolution of the CBVH should be less than or equal to the FSR of the FPE, otherwise there is ambiguity in retrieving the spectral information.

We have experimentally demonstrated a tandem spectrometer by cascading a FPE with a CBVH. The tandem spectrometer results in a true 2D spatial-spectral mapping and, thus, does not severely suffer from the trade-off between resolution and operation bandwidth in contrast to conventional spectrometers. Using this spectrometer, a resolution of 0.2 nm over a bandwidth of almost 50 nm has been achieved. Moreover, the performance of this tandem spectrometer has been tested with standard light sources. We have actually shown that its performance is comparable to that of some sophisticated spectrometers such as Oriel InstaSpec spectrometers.

What remains to be further investigated, is to use the true 2D spatial-spectral mapping property of this tandem spectrometer to increase its bandwidth while keeping the resolution intact. For this investigation, we can use a spatially multiplexed CBVH (with the same FPE) to increase the bandwidth to a few 100 nm. The next step is to study the throughput issue and try to improve it by using unique properties of volume holograms, especially their multiplexing that allows more sophisticated 2D spatial-

spectral mapping to obtain better throughput. For commercializing this research, there is also a need to investigate other materials such as photopolymers or doped glasses for recording volume holograms. These materials are less expensive than Lithium Niobate and can be recorded more easily and quickly. They do not require thermal fixing as needed for Lithium Niobate for acceptable lifetime of the volume hologram.

8.2. Fast and Efficient Modeling of a Spatially Incoherent Source

First we have tried a Monte-Carlo model for modeling and simulation of spatially incoherent sources using an array of Poisson pulse trains. Compared to the brute-force method, we have shown that by using this method it is possible to reduce the simulation time by one order of magnitude while keeping the relative error below 10%. The advantage of the proposed method over the brute-force method becomes stronger for larger structures. However, the 10% error might be too much for some applications. For better accuracy, we have come up with a more accurate model using WCE method. In this approach we have proposed a stochastic model for spatially incoherent sources. Then, we have successfully applied the WCE method to reduce the stochastic wave equation into a set of deterministic PDEs for the expansion coefficients of the random fields. The significant advantage of this model is that all the statistical moments of the field values can be directly calculated using these expansion coefficients.

We have used the standard FDTD technique to numerically simulate these deterministic PDEs for a typical 2D PC structure. We have compared the WCE model with the exact brute-force model and demonstrated the WCE model accurately simulates the propagation of spatially incoherent source much faster than the brute-force model.

This is a consequence of the extremely fast convergence behavior of the WCE series in which a small number of expansion terms is sufficient for achieving accurate simulation.

This part of our research is almost complete and there is no major issue remained for future investigation. The next step is to use this simulation tool for analysis and design of 3D PC microspectrometers under diffuse light illumination. Although we did not show any 3D simulation in this research, all the analytical formulation and numerical implementation can be readily carried on to the 3D propagation problem. Moreover, the simulation time advantage of the WCE model will be even more remarkable for 3D structures (with 2D source planes) as the number of input source points needed for the brute-force simulation will be very large in this case.

8.3. Analysis and Design of a 3D PC Demultiplexer

First we have developed an accurate and efficient model based on effective diffractive indices for the analysis of beam propagation effects inside 3D PC structures. We have shown that two principal diffractive indices (corresponding to two principal diffraction directions) can be defined to describe the propagation of beams in an arbitrary direction inside these structures. The model has good accuracy for the analysis of all 3D PCs of interest for practical applications. Using this method, the beam propagation effects can be studied using simple geometrical optics formulas, which significantly reduces the amount of memory and computation cost needed for 3D structures compared to other approaches. Thus, the model enables efficient analysis, design, and optimization of 3D PC structures and opens up new possibilities for practical applications of 3D PCs by facilitating their modeling.

Then, we have used this diffractive model to analyze and design 3D tetragonal woodpile structures for demultiplexing applications. We have tried to bias these 3D PCs at a work point on their band structure so we can simultaneously combine the superprism effect, diffraction compensation, and negative refraction to minimize the size of these demultiplexers and at the same time, minimize the cross-talk between adjacent channels. Using this strategy we have reported the design of a 4-chanell and a 6-channel demultiplexer. Besides, it has been shown that we can selectively excite a single mode of these woodpile structures by proper choice of the incident polarization.

Although this part of our research has been performed to a good extent, the experimental demonstration of these demultiplexers is remained as the first priority to be investigated in near future. As a next step we can extend these demultiplexers to form microspectrometers and examine their capabilities for spectrum estimation. Therefore, one important task is to optimize the performance measures such as bandwidth and resolution of these demultiplexers. For this purpose, other PC lattice geometries as well as other host materials need to be investigated. Another interesting extension of this work is to investigate the use of 3D PC heterostructures in which each portion of the structure is engineered to optimize a subset of optical functionalities. The simplest version of such heterostructures is the integration of interferometry and spectroscopy in a single structure. The most general view of such engineered heterostructures is to consider them as a universal 3D device for the spatial-spectral mapping of the information in an optical beam. Considering the extensive opportunities exist in this research and the novelty of the research topic, we feel that at least another complete Ph.D. thesis can be devoted to these taskes.

To conclude a brief summary of contributions of this research follows:

- Design of a compact, low-cost, alignment insensitive diffuse light spectrometer with high resolution, large bandwidth, and 2D spatial-spectral response
- Experimental demonstration of the tandem FPE-CBVH spectrometer with resolution better than 0.2 nm for diffuse light spectroscopy
- Development of a Monte-Carlo model for simulation of a spatially incoherent source
- Development of a fast and efficient simulation model for a spatially incoherent source based on the WCE method (the first theoretical model proposed so far for simulation of spatially incoherent sources)
- Development of an approximate diffractive index model for efficient and intuitive analysis of the diffraction effects inside 3D PC structures
- Developing the idea and systematically designing 3D PC demultiplexers based on dispersion compensation (the first 3D PC demultiplexers proposed so far)

REFERENCES

[1] G. P. Anderson, K. D. King, D. S. Cuttino, J. P. Whelan, F. S. Ligler, J. F. MacKrell, C. S. Bovais, D. K. Indyke, R. J. and Foch, "Biological agent detection with the use of an airborne biosensor," Field Analytical Chemistry and Technology **3**, 307–314 (1999).

[2] M. A. Cooper, "Optical biosensors in drug discovery," Nature Reviews Drug Discovery **1,** 515-528 (2002).

[3] Y. Pan, V. Boutou, R. K. Chang, I. Ozden, K. Davitt, and A. V. Nurmikko, "Application of light-emitting diodes for aerosol fluorescence detection," Optics Letters **28**, 1707-1709 (2003).

[4] E. D. Lester, G. Bearman, A. Ponce, "A second-generation anthrax "smoke detector"," IEEE Engineering in Medicine and Biology Magazine **23**, 130-135 (2004).

[5] J. Xu, D. Suarez, and D. S. Gottfried, "Detection of avian influenza virus using an interferometric biosensor," Analytical and Bioanalytical Chemistry **389**, 1193-1199 (2007).

[6] A. J. Berger, Y. Wang, and M. S. Feld, "Rapid, noninvasive concentration measurements of aqueous biological analytes by near-infrared Raman spectroscopy," Applied Optics **35**, 209-212 (1996).

[7] R. A. Zangaro, L. Silveira, R. Manoharan, G. Zonios, I. Itzkan, R. R. Dasari, J. Van Dam, and M. S. Feld, "Rapid multiexcitation fluorescence spectroscopy system for in vivo tissue diagnosis," Applied Optics **35**, 5211-5219 (1996).

[8] A. J. Berger, T. Koo, I. Itzkan, G. Horowitz, and M. S. Feld, "Multicomponent blood analysis by near-infrared Raman spectroscopy," Applied Optics **38**, 2916-2926 (1999).

[9] S. C. Hill, R. G. Pinnick, S. Niles, N. F. Fell, Jr., Y. Pan, J. Bottiger, B. V. Bronk, S. Holler, and R. K. Chang, "Fluorescence from airborne microparticles: dependence on size, concentration of fluorophores, and illumination intensity," Applied Optics **40**, 3005-3013 (2001).

[10] V. Sivaprakasam, A. L. Huston, C. Scotto, and J. D. Eversole, "Multiple UV wavelength excitation and fluorescence of bioaerosols," Optics Express **12**, 4457-4466 (2004).

[11] P. D. Kaplan, M. S. Kao, A. G. Yodh, and D. J. Pine, "Geometric constraints for the design of diffusing-wave spectroscopy experiments," Applied Optics **32**, 3828-3836, (1993).

[12] D. J. Pine, D. A. Weitz, J. X. Zhu, D. J. Durian, A. G. Yodh, and M. Kao, "Diffusing-wave spectroscopy and interferometry," Macromolecular Symposia **79**, 31-44 (1994).

[13] A. G. Yodh and B. Chance, "Spectroscopy and imaging with diffusing light," Physics Today **48**, 34-40 (1995).

[14] H. Stark, M. H. Kao, K. A. Jester, T. C. Lubensky, and A. G. Yodh, "Light diffusion and diffusing-wave spectroscopy in nematic liquid crystals," Journal of the Optical Society of America A **14**, 156-178 (1997).

[15] G. Zonios, L. T. Perelman, V. M. Backman, R. Manoharan, M. Fitzmaurice, J. Van Dam, and M. S. Feld, "Diffuse reflectance spectroscopy of human adenomatous colon polyps in vivo," Applied Optics **38**, 6628-6637 (1999).

[16] C. Hsieh, O. Momtahan, A. Karbaschi, and A. Adibi, "A compact Fourier transform volume holographic spectrometer for diffuse source spectroscopy," Optics Letters **30**, 836-838 (2005).

[17] E. C. Cull, M. E. Gehm, D. J. Brady, C. R. Hsieh, O. Momtahan, and A. Adibi, "Dispersion multiplexing with broadband filtering for miniature spectrometers," Applied Optics **46**, 365-374 (2007).

[18] O. Momtahan, C. Hsieh, A. Karbaschi, A. Adibi, M. E. Sullivan, and D. J. Brady, "Spectral diversity filters using spherical beam volume holograms: theory and implementation," Applied Optics **43**, 6557- 6567 (2004).

[19] O. Momtahan, C. Hsieh, A. Adibi, and D. J. Brady, "Analysis of slitless holographic spectrometers implemented by spherical beam volume holograms," Applied Optics **45**, 2955-2964 (2006).

[20] G. G. Shepherd, C. W. Lake, J. R. Miller, and L. L. Cogger, "A spatial spectral scanning technique for the Fabry-Perot spectrometer," Applied Optics **4**, 267-272 (1965).

[21] M. Conde, "Driving wavelength spectra from fringe images from a fixed-gap single-etalon Fabry-Perot spectrometer," Applied Optics **41**, 2672-2678 (2002).

[22] S. Fan, P. R. Villeneuve, R. D. Meade and J. D. Joannopoulos, "Design of three dimensional photonic crystals at submicron lengthscales," Applied Physics Letters **65**, 1466-1468 (1994).

[23] S. Y. Lin, J. G. Fleming, D. L. Hetherington, B. K. Smith, R. Biswas, K. M. Ho, M. M. Sigalas, W. Zubrzycki, S. R. Kurtz, and J. Bur, "A three-dimensional photonic crystal operating at infrared wavelengths," Nature **394**, 251-253 (1998).

[24] M. Qi, E. Lidorikis, P. T. Rakich, S. G. Johnson, J. D. Joannopoulos, E. P. Ippen, and H. I. Smith, "A three-dimensional optical photonic crystal with designed point defects," Nature **429**, 538-542 (2004).

[25] Z. Xu, Z. Wang, M. E. Sullivan, and D. J. Brady, "Multimodal multiplex spectroscopy using photonic crystals," Optics Express **11**, 2126-2133 (2003).

[26] E. Yablonovitch, "Inhibited spontaneous emission in solid-state physics and electronics," Phys. Rev. Lett., vol. 58, pp. 2059-2062 (1987).

[27] S. John, "Strong localization of photons in certain disordered dielectric superlattices," Phys. Rev. Lett., vol. 58, pp. 2486-2489 (1987).

[28] J. Joannopoulos, R. Meade, and J. Winn, *Photonic Crystals: Molding the Flow of Light*, Princeton University Press, Princeton, NJ, 1995.

[29] J. D. Joannopoulos, P. R. Villeneuve, and S. Fan, "Photonic crystals: putting a new twist on light," Nature **386**, 143-147 (1997).

[30] S. Fan, A. Mekis, S. G. Johnson, J. D. Joannopoulos, "Manipulating light with photonic crystals," AIP Conference Proceedings **560**, 57-76 (2001).

[31] J. Witzens, M. Loncar, and A. Scherer, "Self-collimation in planar photonic crystals," IEEE Journal of Selected Topics in Quantum Electronics **8**, 1246-1257 (2002).

[32] L. Wu, M. Mazilu, and T. F. Krauss, "Beam steering in planar-photonic crystals: From superprism to supercollimator," Journal of Lightwave Technology **21**, 561-566 (2003).

[33] D. N. Chigrin, S. Enoch, C. M. Sotomayor Torres, and G. Tayeb, "Self-guiding in two-dimensional photonic crystals," Optics Express **11**, 1203-1211 (2003).

[34] S. Shi, A. Sharkawy, C. Chen, D. M. Pustai, and D. W. Prather, "Dispersion-based beam splitter in photonic crystals," Optics Letters **29**, 617-619 (2004).

[35] L. Wu, M. Mazilu, J. -F. Gallet, and T. F. Krauss, "Dual lattice photonic-crystal beam splitters," Applied Physics Letters **86**, 211106-1-3 (2005).

[36] S. Lin, V. M. Hietala, L. Wang, and E. D. Jones, "Highly dispersive photonic band-gap prism," Optics Letters **21**, 1771-1773 (1996).

[37] H. Kosaka, T. Kawashima, A. Tomita, M. Notomi, T. Tamamura, T. Sato, and S. Kawakami, "Superprism phenomena in photonic crystals," Physical Review B **58**, R10096-R10099 (1998).

[38] H. Kosaka, T. Kawashima, A. Tomita, M. Notomi, T. Tamamura, T. Sato, and S. Kawakami, "Superprism phenomena in photonic crystals: Toward microscale lightwave circuits," Journal of Lightwave Technology **17**, 2032-2038 (1999).

[39] B. Momeni and A. Adibi, "Optimization of photonic crystal demultiplexers based on the superprism effect," Applied Physics B **77**, 555-560 (2003).

[40] T. Matsumoto and T. Baba, "Photonic crystal k-vector superprism," Journal of Lightwave Technology **22**, 917-922 (2004).

[41] J. Witzens, T. Baehr-Jones, and A. Scherer, "Hybrid superprism with low insertion losses and suppressed cross-talk," Physical Review E **71**, 026604-1-9 (2005).

[42] B. Momeni and A. Adibi, "Systematic design of superprism-based photonic crystal demultiplexers," IEEE Journal of Selected Areas in Communications **23**, 1355-1364 (2005).

[43] T. Matsumoto, S. Fujita, and T. Baba, "Wavelength demultiplexer consisting of Photonic crystal superprism and superlens," Optics Express **13**, 10768-10776 (2005).

[44] B. Momeni, J. Huang, M. Soltani, M. Askari, S. Mohammadi, A. Adibi, and M. Rakhshandehroo, "Compact wavelength demultiplexing using focusing negative index photonic crystal superprisms," Optics Express **14**, 2413-2422 (2006).

[45] B. Momeni, E. Shah Hosseini, M. Askari, S. Mohammadi, M. Soltani, A. A. Eftekhar, M. Badieirostami, J. Huang, and A. Adibi, "Integrated photonic crystal spectrometers for sensing applications," submitted for publication.

[46] S. G. Romanov, P. Ferrand, M. Egen, R. Zentel, J. Ahopelto, N. Gaponik, A. Eychmüller, A. L. Rogach, and C. M. Sotomayor Torres, "Exploring integration prospects of opal-based photonic crystals," Synthetic Metals **139**, 701–704 (2003).

[47] M. Deubel, G. von Freymann, M. Wegener, S. Pereira, K. Busch, C. M. Soukoulis, "Direct laser writing of three-dimensional photonic-crystal templates for telecommunications," Nature Materials **3**, 444-447 (2004).

[48] R. Guo, Z. Li, Z. Jiang, D. Yuan, W. Huang, and A. Xia, "Log-pile photonic crystal fabricated by two-photon photopolymerization," Journal of Optics A: Pure and Applied Optics **7**, 396-399 (2005).

[49] M. Deubel, M. Wegener, S. Linden, G. von Freymann, and S. John, "3D-2D-3D photonic crystal heterostructures fabricated by direct laser writing," Optics Letters **31**, 805-807 (2006).

[50] Y. C. Zhong, S. A. Zhu, H. M. Su, and H. Z. Wang, J. M. Chen, Z. H. Zeng and Y. L. Chen, "Photonic crystal with diamondlike structure fabricated by holographic lithography," Applied Physics Letters **87**, 061103-1-3 (2005).

[51] J. H. Moon, J. Ford, and S. Yang, "Fabricating three-dimensional polymeric photonic structures by multi-beam interference lithography," Polymers for Advanced Technologies **17**, 83-93 (2006).

[52] J. H. Moon, S. Yang; S. –M. Yang, "Photonic band-gap structures of core-shell simple cubic crystals from holographic lithography," Applied Physics Letters **88**, 121101-1-3 (2006).

[53] J. Mizuguchi, Y. Tanaka, S. Tamura, and M. Notomi, "Focusing of light in a three-dimensional cubic photonic crystal," Physical Review B **67**, 75109-1-7 (2003).

[54] T. Prasad, V. Colvin, and D. Mittleman, "Superprism phenomenon in three-dimensional macroporous polymer photonic crystals," Physical Review B **67**, 165103-1-7 (2003).

[55] X. Ao and S. He, "Three-dimensional photonic crystal of negative refraction achieved by interference lithography," Optics Letters **29**, 2542-2544 (2004).

[56] Z. Lu, S. Shi, C. A. Schuetz, J. A. Murakowski, and D. W. Prather "Three-dimensional photonic crystal flat lens by full 3D negative refraction," Optics Express **13**, 5592-5599 (2005).

[57] J. Shin and S. Fan, "Conditions for self-collimation in three-dimensional photonic crystals," Optics Letters **30**, 2397-2399 (2005).

[58] Z. Lu, J. A. Murakowski, C. A. Schuetz, S. Shi, G. J. Schneider, and D W. Prather, "Three-dimensional subwavelength imaging by a photonic-crystal flat lens using negative refraction at microwave frequencies," Physical Review Letters **95**, 153901-1-4 (2005).

[59] Z. Lu, S. Shi, J. A. Murakowski, G. J. Schneider, C. A. Schuetz, and D. W. Prather, "Experimental demonstration of self-collimation inside a three-dimensional photonic crystal," Physical Review Letters **96**, 173902-1-4 (2006).

[60] J. Chen, W. Jiang, X. Chen, L. Wang, S. Zhang, and R. T. Chen, "Holographic three-dimensional polymeric photonic crystals operating in the 1550 nm window," Applied Physics Letters **90**, 093102-1-3 (2007).

[61] J. F. James and R. S. Sternberg, *The Design of Optical Spectrometers*, Chapman & Hall, London, UK, 1969.

[62] J. T. Verdeyen, *Laser Electronics*, Third Edition, Prentice Hall, Englewood Cliffs, NJ, 1995.

[63] O. Momtahan, C. Hsieh, and A. Adibi, "Multifunctional and compact spectrometers based on cylindrical beam volume holograms," Optics Letters **32**, 3269-3271 (2007).

[64] P. C. Clemmow, *The Plane Wave Spectrum Representation of Electromagnetic Fields*, Oxford University Press-IEEE Press, New York, NY, 1996.

[65] M. Badieirostami, O. Momtahan, C. Hsieh, A. Adibi, and D. J. Brady, "Very-high-resolution tandem Fabry-Perot etalon cylindrical beam volume hologram spectrometer for diffuse source spectroscopy," Optics Letters **33**, 31-33 (2008).

[66] S. T. McCain, M. E. Gehm, Y. Wang, N. P. Pitsianis, and D. J. Brady, "Coded aperture Raman spectroscopy for quantitative measurements of Ethanol in a tissue phantom," Applied Spectroscopy **60**, 663-671 (2006).

[67] B. Bates, D. J. McCartney, C. D. McKeith, A. McQuoid, and O. E. Sproule, "Interferometer-grating spectrograph for high resolution astronomical spectroscopy in the middle UV," Applied Optics **17**, 2119-2124 (1978).

[68] D. T. Speer, S. Von Laven, A. H. Karp, and M. Stockton, "Etalon-spectrograph system for improved resolution over a wide spectral range," Applied Optics **19**, 2757-2761 (1980).

[69] T. Iwata and J. Koshoubu, "Proposal for high resolution, wide-bandwidth, high-optical-throughput spectroscopic system using a Fabry-Perot interferometer," Applied Spectroscopy **52**, 1008-1013 (1998).

[70] S. D. Feller, H. Chen, D. J. Brady, M. E. Gehm, C. Hsieh, O. Momtahan, and A. Adibi, "Multiple order coded aperture spectrometer," Optics Express **15**, 5625-5630 (2007).

[71] A. Taflove and S. C. Hagness, *Computational Electrodynamics*, Artech House, Norwood, MA, 2000.

[72] M. Badieirostami, O. Momtahan, B. Momeni, and A. Adibi, "Efficient modeling of a spatially incoherent source for characterization of photonic crystal structures under diffuse light illumination," submitted for publication.

[73] L. Mandel and E. Wolf, *Optical Coherence and Quantum Optics*, Cambridge University Press, Cambridge, MA, 1995.

[74] A. Papoulis and S. Unnikrishna Pillai, *Probability*, *Random Variables and Stochastic Processes*, McGraw-Hill, New Delhi, India, 2002.

[75] J. W. Goodman, *Statistical Optics*, Wiley Classics Library Edition, New York, NY, 2000.

[76] R. G. Ghanem and P. D. Spanos, *Stochastic Finite Elements: A Spectral Approach*, Springer-Verlag, Berlin, Germany, 1991.

[77] H. G. Matthies and C. Bucher, "Finite elements for stochastic media problems," Computer Methods in Applied Mechanics and Engineering **168**, 3-17 (1999).

[78] R. Mikulevicius and B. L. Rozovskii, "Stochastic Navier-Stokes equations. Propagation of chaos and statistical moments," *Optimal Control and Partial Differential Equations*, J. L. Menaldi, E. Rofmann, and A. Sulem (Eds.) in honor of Professor Alain Bensoussan's 60th Birthday, 258-267, IOS Press, Amsterdam, Netherland, 2001.

[79] M. Jardak, C. H. Su, and G. E. Karniadakis, "Spectral polynomial chaos solutions of the stochastic advection equation," Journal of Scientific Computing **17**, 319-338 (2002).

[80] S. Sakamoto and R. Ghanem, "Polynomial chaos decomposition for the simulation of non-Gaussian non-stationary stochastic processes," Journal of Engineering Mechanics **128**, 190-201 (2002).

[81] D. Xiu and G. E. Karniadakis, "The Wiener-Askey polynomial chaos for stochastic differential equations," SIAM Journal on Scientific Computing **24**, 619-644 (2002).

[82] D. Xiu and G. E. Karniadakis, "Modeling uncertainty in flow simulations via generalized polynomial chaos," Journal of Computational Physics **187**, 137-167 (2003).

[83] D. Lucor and G. E. Karniadakis, "Adaptive generalized polynomial chaos for nonlinear random oscillators," SIAM Journal on Scientific Computing **26**, 720-735 (2004).

[84] D. Zhang, Z. Lu, "An efficient, high-order perturbation approach for flow in random porous media via Karhunen-Loeve and polynomial expansion," Journal of Computational Physics **194**, 773-794 (2004).

[85] T. Y. Hou, W. Luo, B. Rozovskii, and H. Zhou, "Wiener chaos expansions and numerical solutions of randomly forced equations of fluid mechanics," Journal of Computational Physics **216**, 687-706 (2006).

[86] M. Badieirostami, A. Adibi, H. Zhou, and S. Chow, "Model for efficient simulation of spatially incoherent light using the Wiener chaos expansion method," Optics Letters **32**, 3188-3190 (2007).

[87] M. Badieirostami, A. Adibi, H. Zhou, and S. Chow, "Wiener chaos expansion and simulation of electromagnetic wave propagation excited by a spatially incoherent source," submitted for publication.

[88] J. Shin and S. Fan, "Conditions for self-collimation in three-dimensional photonic crystals," Optics Letters **30**, 2397-2399 (2005).

[89] J. Mizuguchi, Y. Tanaka, S. Tamura, and M. Notomi, "Focusing of light in a three-dimensional cubic photonic crystal," Physical Review B **67**, 75109-1-7 (2003).

[90] B. Momeni and A. Adibi, "An approximate effective index model for efficient analysis and control of beam propagation effects in photonic crystals," Journal of Lightwave Technology **23**, 1522-1532 (2005).

[91] B. Momeni, M. Badieirostami, and A. Adibi, "Modeling the propagation of optical beams in three-dimensional photonic crystals," Journal of Optical Society of America B **25**, 785-793 (2008).

[92] M. Badieirostami, B. Momeni, and A. Adibi, "Polarization state for modes of low-contrast three-dimensional photonic crystal structures," in preparation.

[93] J. J. Stoker, *Differential Geometry*, Chapter 4, John Wiley & Sons Inc., New York, NY, 1969.

[94] B. Momeni and A. Adibi, "Preconditioned superprism-based photonic crystal demultiplexers: Analysis and design," Applied Optics **45**, 8466-8476 (2006).

VITA

MAJID BADIEIROSTAMI

Majid Badieirostami was born in Tehran, Iran. He received a B.S. degree in Electrical Engineering from Sharif University of Technology, Tehran, Iran in 2002. He moved to the School of Electrical and Computer Engineering at Georgia Institute of Technology in 2003 where he received a M.S. and a Ph.D. degree in 2005 and 2008, respectively. He is the recipient of the School of Electrical and Computer Engineering Graduate Research Assistant Excellence Award from Georgia Institute of Technology in 2008, the Best Paper Award from the International Association for Mathematics and Computers in Simulation (IMACS), Athens, GA, in 2007 and the Newport Research Excellence Award from the Photonics West Optoelectronics Symposium, San Jose, CA, in 2006. He also received the School of Electrical and Computer Engineering Outstanding Graduate Teaching Assistant Award from Georgia Institute of Technology in 2004. His technical interests are optical spectroscopy, biophotonics, nanophotonics, and electromagnetics.